

LEVEL II

12/85

ELECTROMAGNETICS LABORATORY
TECHNICAL REPORT NO. 81-4

April 1981

STUDY OF ANTENNA RADOME PROBLEMS

S. W. Lee
M. S. Sheshadri
R. Mittra



DTIC
SELECTED
S D
JUL 30 1981
D

Approved for public release
Distribution unlimited

ELECTROMAGNETICS LABORATORY
DEPARTMENT OF ELECTRICAL ENGINEERING
ENGINEERING EXPERIMENT STATION
UNIVERSITY OF ILLINOIS AT URBANA-CHAMPAIGN
URBANA, ILLINOIS 61801

N00019-80-C-0284
DEPARTMENT OF THE NAVY
NAVAL AIR SYSTEMS COMMAND
WASHINGTON, D.C. 20361

81 7 30 011

ERIC FILE COPY

"The views and conclusions contained in this document are those of the authors and should not be interpreted as necessarily representing the official policies, either expressed or implied, of the Naval Air Systems Command or the U.S. Government."

UNCLASSIFIED

SECURITY CLASSIFICATION OF THIS PAGE (When Data Entered)

REPORT DOCUMENTATION PAGE		READ INSTRUCTIONS BEFORE COMPLETING FORM
1. REPORT NUMBER	2. GOVT ACCESSION NO.	3. RECIPIENT'S CATALOG NUMBER
AD-A102 205		
4. TITLE (and SUBTITLE) STUDY OF ANTENNA RADOME PROBLEMS	5. TYPE OF REPORT /66666/00000000/ Final Technical 6 April 1980-5 April 1981	
6. AUTHORITY S. W. Lee, M. S. Sheshadri, and R. Mittra	7. PERFORMING ORG. REPORT NUMBER VEM 81-4; UILU-ENG-81-2545	
8. PERFORMING ORGANIZATION NAME AND ADDRESS Department of Electrical Engineering University of Illinois Urbana, IL 61801	9. PROGRAM ELEMENT, PROJECT, TASK AREA & WORK UNIT NUMBERS	
10. CONTROLLING OFFICE NAME AND ADDRESS Department of the Navy Naval Air Systems Command Washington, DC 20361	11. REPORT DATE April 1981	
12. MONITORING AGENCY NAME & ADDRESS// different from Controlling Office)	13. NUMBER OF PAGES 127	
	14. SECURITY CLASS. (of this report) UNCLASSIFIED	
	15a. DECLASSIFICATION/DOWNGRADING SCHEDULE	
16. DISTRIBUTION STATEMENT (of this Report) Distribution Unlimited	17. DISTRIBUTION STATEMENT (of the abstract entered in Block 20, if different from Report) Review for public release Distribution Unlimited	
18. SUPPLEMENTARY NOTES The views and conclusions contained in this document are those of the authors and should not be interpreted as necessarily representing the official policies, either expressed or implied, of the Naval Air Systems Command or the U.S. Government.		
19. KEY WORDS (Continue on reverse side if necessary and identify by block number) Array; boresight error; caustics; curvature matrix; concave lens; convex lens; convexo-concave lens; dielectric radome; dielectric interface; divergence factor; geometrical optics; multiple refraction; radiation pattern; spherical dielectric shell.		
20. ABSTRACT (Continue on reverse side if necessary and identify by block number) In a previous report [5], details of the analysis of a curved dielectric radome using geometrical optics were considered for a point source. In this report, we first consider the transmission of a spherical or plane wave through a curved dielectric interface. The transmitted field is proportional to the product of the conventional Fresnel's transmission coefficient and a divergence factor DF, which describes the cross-sectional variation (convergence or divergence) of a ray pencil as the latter propagates in		

the transmitted region. The factor DF depends on the incident wavefront, the curvatures of the interface, and the relative indices of the two media. We give explicit matrix formulas for calculating DF, illustrate its physical significance via examples, and point out an erroneous solution in the recent literature.

Next, we study the transmission of a spherical electromagnetic wave through a dielectric shell. The two surfaces of the shell are spherical (either concave or convex), and their centers are arbitrarily located in relation to the source point. The field solution determined by the geometrical optics theory is given in a simple closed form. Special attention is given to the lens effect of the dielectric shell which converts the incoming spherical pencil into a focusing pencil.

Finally, we present extensive numerical results on arrays of point sources covered by practical radomes.

141 DEM-71-4, UIU-ENG-81-2545

Electromagnetics Laboratory Report No. 81-4

6 STUDY OF ANTENNA RADOME PROBLEMS

Final Technical Report.
6 April 1980-5 April 1981

S. W. Lee
M. S. Sheshadri
R. Mittra

11 Apr 1981

12 128

Department of the Navy
Naval Air Systems Command
Washington, D.C. 20361

Contract No. N00019-80-C-0284

Electromagnetics Laboratory
Department of Electrical Engineering
University of Illinois at Urbana-Champaign
Urbana, Illinois 61801

Accession For	
NTIS GRA&I	<input type="checkbox"/>
DTIC TAB	<input type="checkbox"/>
Unannounced	<input type="checkbox"/>
Justification	
By	
Distribution/	
Availability Codes	
Avail and/or	
Dist	Special
A	

DTIC
ELECTE
S JUL 30 1981
D

ABSTRACT

In a previous report [5], details of the analysis of a curved dielectric radome using geometrical optics were considered for a point source. In this report, we first consider the transmission of a spherical or plane wave through a curved dielectric interface. The transmitted field is proportional to the product of the conventional Fresnel's transmission coefficient and a divergence factor DF, which describes the cross-sectional variation (convergence or divergence) of a ray pencil as the latter propagates in the transmitted region. The factor DF depends on the incident wavefront, the curvatures of the interface, and the relative indices of the two media. We give explicit matrix formulas for calculating DF, illustrate its physical significance via examples, and point out an erroneous solution in the recent literature.

Next, we study the transmission of a spherical electromagnetic wave through a dielectric shell. The two surfaces of the shell are spherical (either concave or convex), and their centers are arbitrarily located in relation to the source point. The field solution determined by the geometrical optics theory is given in a simple closed form. Special attention is given to the lens effect of the dielectric shell which converts the incoming spherical pencil into a focusing pencil.

Finally, we present extensive numerical results on arrays of point sources covered by practical radomes.

TABLE OF CONTENTS

	Page
I. INTRODUCTION.	1
II. DESCRIPTION OF PROBLEM.	6
III. FIELD SOLUTION BY GEOMETRICAL OPTICS.	8
A. Method of Solution.	8
IV. REFRACTION AT A CURVED DIELECTRIC INTERFACE	15
A. Introduction.	15
B. Final Solution for the Refracted Fields	16
C. Calculation of Curvatures of Refracted Wavefronts	20
D. Special Case: Spherical Interface.	25
E. Numerical Results and Discussion.	31
F. Conclusion.	46
V. WAVE TRANSMISSION THROUGH A SPHERICAL DIELECTRIC SHELL.	47
A. Introduction.	47
B. Solution for Concentric Spherical Shell	49
C. Generalization of Final Solution.	52
D. Axial Incidence on Symmetrical Shells	54
E. Numerical Results	64
F. Conclusions	75
VI. ARRAY COVERED BY RADOME	77
APPENDIX A: DERIVATION OF EQUATION (5.6)	113
REFERENCES.	115
DISTRIBUTION LIST	117

LIST OF FIGURES

Figure	Page
1. Antenna A and radome I.	2
2. Two choices of incident directions: Al and Pl.	2
3. An aperture antenna A inside a radome is approximated by an array B.	5
4. Transmission through a dielectric shell due to incidence from a point source at P_0	5
5. Coordinate systems for refraction at surface I_1	9
6. Coordinate systems for refraction at surface I_2	9
7. Refraction at a curved dielectric interface I	17
8. Refraction at a spherical dielectric interface.	26
9. Refraction at a concave spherical dielectric interface of a normally incident plane wave.	28
10. Three dielectric interfaces	32
11. E-plane far-field pattern through a concave spherical interface	34
12. Same as Figure 11, except for H-plane pattern	35
13. Axial far-field variation with source position for concave spherical interface	37
14. E-plane far-field pattern through a concave paraboloid. . . .	38
15. Same as Figure 14, except for H-plane pattern	39
16. E-plane far-field pattern through a concave hyperboloid . .	40
17. Same as Figure 16, except for H-plane pattern	41
18. E-plane far-field pattern through convex interfaces	42
19. Same as Figure 12, except for H-plane pattern	43
20. Ray picture and trace of foci of the transmitted rays which lie in the x-z plane, for the convex spherical interface with source at (6)	45

Figure	Page
21. Transmission of a spherical wave emitted from source 0 through a spherical dielectric shell.	48
22. General configurations where the field solution (2.3) can be used	53
23. Axial incidence on a symmetrical shell.	55
24. Condition for a convergent beam inside the dielectric shell	56
25. Transmitted field E_x transmitted through a spherical shell normalized by E_b which is that through a dielectric slab. .	59
26. Singly and doubly refracted rays through a dielectric slab. .	61
27. Error introduced by neglecting all or all except one multiply refracted ray in a dielectric slab	63
28. E-plane radiation pattern through a spherical radome. . . .	65
29. Double-concave spherical dielectric lens: geometry and ray picture	66
30. H-plane far-field pattern through lens I and lens II. . . .	68
31. Trace of foci of the transmitted rays which lie in x-z plane for lenses I and II	69
32. Double-convex spherical dielectric lens: geometry and ray picture	71
33. Convexo-concave spherical dielectric lens: geometry and ray picture	72
34. H-plane far field pattern through lens III.	73
35. Trace of foci of the transmitted rays which lie in the x-z plane, for lens III	74
36. Paraboloidal radome A generated by Eqs. (6.4) and (6.5) . .	78
37. H-plane element patterns through radome A for sources ①, ③ and ⑥	80
38. H-plane sum pattern through radome A beam at 0°	81
39. Same as Figure 38, except for scan angle = -4.95°	82

Figure	Page
40. Same as Figure 38, except for scan angle = -9.89°	83
41. Same as Figure 38, except for scan angle = -19.77°	84
42. Same as Figure 38, except for scan angle = -27.64°	85
43. Boresight error for radome A.	88
44. Variation of maximum field strength with scan angle for radome A.	89
45. Geometry of radome B.	90
46. H-plane sum pattern through radome B.	91
47. Same as Figure 46, except for scan angle = -4.95°	92
48. Same as Figure 46, except for scan angle = -9.89°	93
49. Same as Figure 46, except for scan angle = -14.83°	94
50. Boresight error for radome B.	95
51. Geometry of radomes C and D	97
52. H-plane pattern through radome C.	98
53. Same as Figure 52, except for scan angle = -4.95°	99
54. Same as Figure 52, except for scan angle = -9.89°	100
55. Same as Figure 52, except for scan angle = -14.83°	101
56. Same as Figure 52, except for scan angle = -19.77°	102
57. Same as Figure 52, except for scan angle = -27.64°	103
58. Boresight error for radome C.	104
59. H-plane pattern through radome D.	105
60. Same as Figure 59, except for scan angle = -4.95°	106
61. Same as Figure 59, except for scan angle = -9.89°	107
62. Same as Figure 59, except for scan angle = -14.83°	108
63. Same as Figure 59, except for scan angle = -19.77°	109

Figure	Page
64. Same as Figure 59, except for scan angle = -27.65°	110
65. Boresight error for radome D.	111
66. Comparison of tangent ogive and an equivalent paraboloid. .	112

I. INTRODUCTION

Many practical antennas are covered by radomes, whose effects on the antenna radiation are of considerable importance, especially in today's high-performance radar/communication systems. In the past quarter of a century, several standard analyses have been devised for analyzing radome effects. None of them is exact, and improvements are always needed. The present report described an effort in this direction.

A typical radome problem may be stated as follows. Let an aperture antenna A, for instance a horn, a slot, or a conformal array, radiate a known field $\vec{E}^1(\vec{r})$ in free space (see Figure 1). A protective shield or radome Σ is placed around antenna A. The problem is to determine the radiation field \vec{E} for the composite structure, i.e., the antenna A radiating in the presence of the radome. This problem has received a great deal of attention from many researchers during the last two decades, and a so-called "best available" method for attacking this problem appears to have emerged. A brief description of this method is given below.

(a) In the vicinity of Σ , the incident field \vec{E}^1 is not a ray field (locally plane wave). To circumvent this difficulty, let \vec{E}^1 be resolved into a spectrum of plane waves, namely,

$$\vec{E}^1(\vec{r}) = \int_{-\infty}^{\infty} dk_x \int_{-\infty}^{\infty} dk_y \vec{W}(\vec{k}) e^{i\vec{k} \cdot \vec{r}} \quad (1.1)$$

$$\vec{W}(\vec{k}) = \left(\frac{1}{2\pi}\right)^2 \int_{-\infty}^{\infty} dx \int_{-\infty}^{\infty} dy \vec{E}^1(\vec{r}) e^{-i\vec{k} \cdot \vec{r}} \quad (1.2)$$

Here, $\vec{k} = (k_x, k_y, k_z)$ is the direction of propagation of the plane-wave spectral component. The spectral wave number in the z-direction,

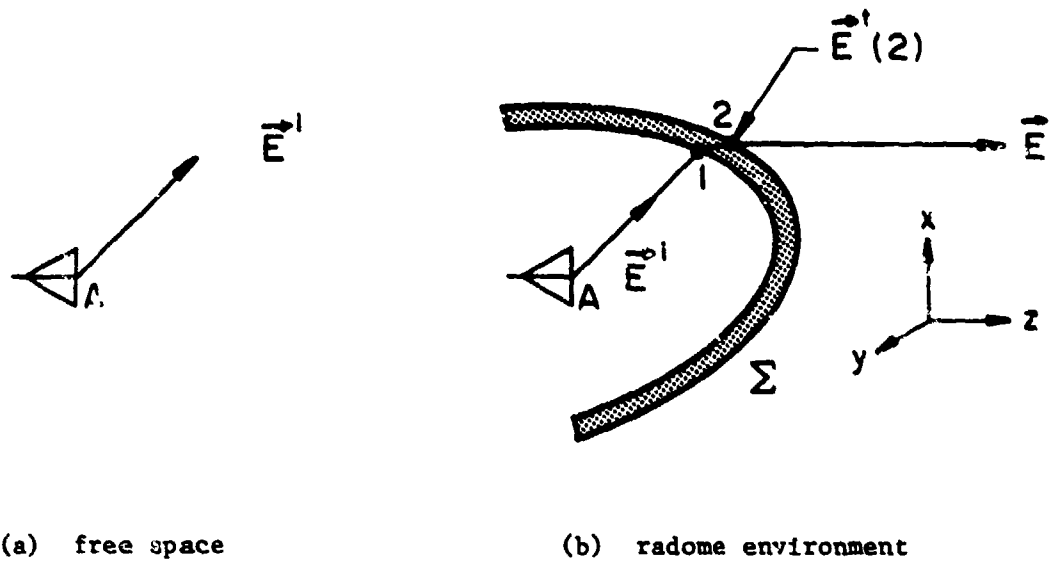


Figure 1. Antenna A and radome Σ .

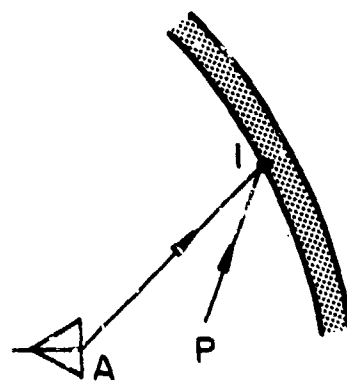


Figure 2. Two choices of incident directions: A_1 and P_1 .

$$k_z = \sqrt{\omega^2 \mu \epsilon - (k_x^2 + k_y^2)} \quad , \quad (1.3)$$

may be real (homogenous plane wave) or imaginary (inhomogenous plane wave). The weighting factor $\hat{W}(\vec{k})$ is the amplitude of the plane-wave spectral component propagating in the direction \vec{k} .

(b) For each plane-wave component, a transmission coefficient matrix $\bar{T}_0(\vec{k})$ for a flat dielectric slab can be obtained from any standard text on EM theory. The subscript zero of \bar{T}_0 indicates that it is derived from the assumption of a plane-wave incident field. The transmitted field $\hat{E}^t(2)$ at point 2 on the outer surface of Σ is calculated from the formula

$$\hat{E}^t(2) = \int_{-\infty}^{\infty} dk_x \int_{-\infty}^{\infty} dk_y \bar{T}_0(\vec{k}) \hat{W}(\vec{k}) e^{i\vec{k} \cdot \vec{r}} . \quad (1.4)$$

(c) Once $\hat{E}^t(2)$ is known for all points on the outer surface of Σ , equivalent surface current sources $(\hat{J}(2), \hat{K}(2))$ can be determined. The convolution of the source with the Green's function gives the desired radiation field which is expressible as

$$\hat{E}(\vec{r}) = \iint_{\text{outer } \Sigma} (\bar{G}_1 \hat{J} + \bar{G}_2 \hat{K}) da . \quad (1.5)$$

The approach described above is of course theoretically sound. However, its faithful execution is impractical because of the extremely laborious numerical integrations in (1.4) and (1.5). In the well-quoted analyses by Paris [1] and Wu and Rudduck [2], the numerical integration in (1.4) is avoided by approximating the transmitted field at point 2 by

$$E^t(2) \approx \bar{T}_0(\vec{k}_0) \hat{W}(\vec{k}_0) e^{i\vec{k}_0 \cdot \vec{r}} \quad (1.6a)$$

where the incident direction is determined by

\hat{k}_0 = actual ray direction A_1 , or the direction P_1 of the Poynting vector of \hat{E}^1 (Figure 2). (1.6b)

Note that the approximation in (1.6) is to describe \hat{E}^1 by a plane wave. Since the radome is in the near zone of the antenna, this plane wave approximation for \hat{E}^1 described in [1], [2] does not seem to be a good one.

In the present report, we approach the radome problem from a different viewpoint. Instead of decomposing the incident field \hat{E}^1 into a plane wave spectrum, we approximate the finite-sized antenna A in Figure 3a by an array B in Figure 3b. Each element in array B radiates a spherical wave. Those spherical wave constituents, transmitting through the radome Σ , are superimposed to give rise to the desired radiation field \hat{E} in the far zone. Thus, the key step in the present approach is to determine the transmission of a spherical wave through a curved dielectric shell.

We shall apply geometrical optics to solve the transmission through the curved radome. Specifically, we first study in detail the different aspects of refraction at a single curved dielectric interface; second, we analyze the behavior of a spherical dielectric shell; and third, we apply our theory to various practical radomes.

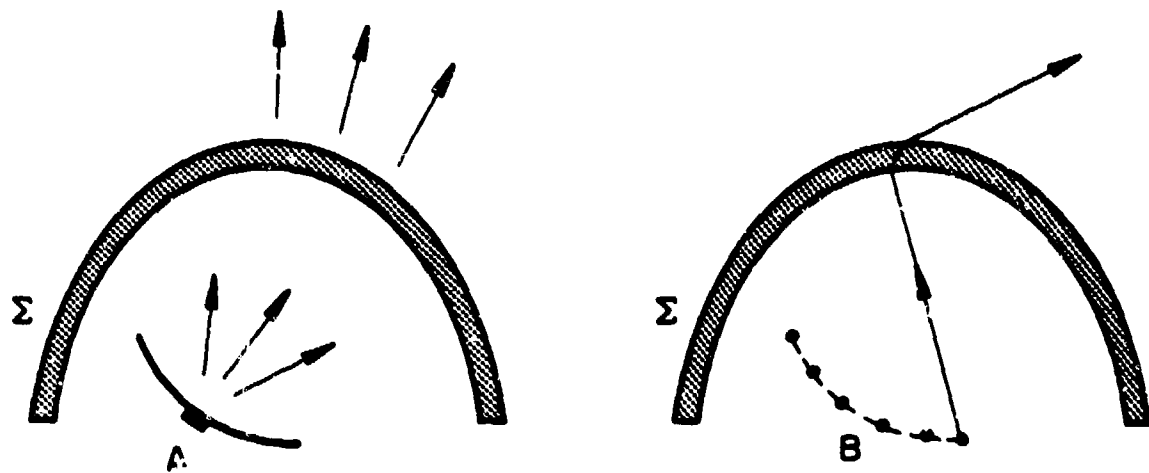


Figure 3. An aperture antenna A inside a radome is approximated by an array B. Each point source in array B radiates a spherical wave.

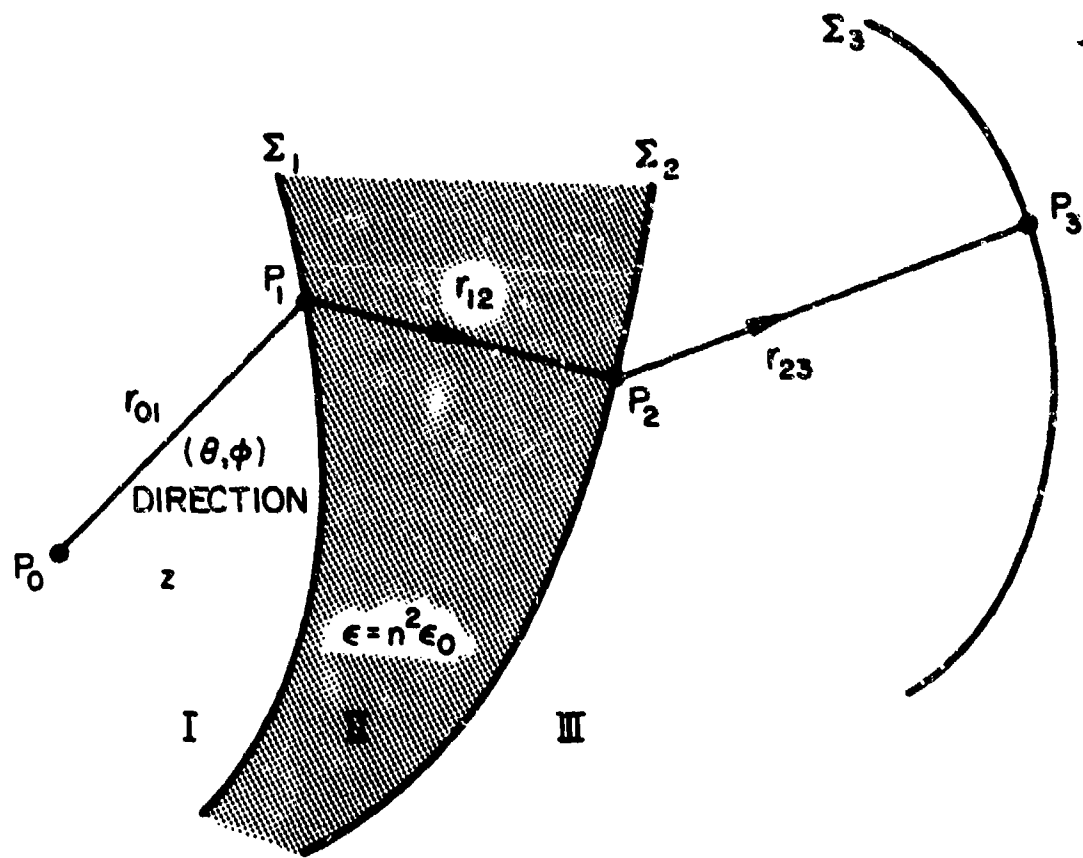


Figure 4. Transmission through a dielectric shell due to incidence from a point source at P_0 .

II. DESCRIPTION OF PROBLEM

The geometry of the radome problem under consideration is sketched in Figure 4. A point source at P_0 produces a spherical wave which goes through a curved dielectric shell with nonuniform thickness. Ray techniques are used to determine the field at point P_3 on a given surface outside the shell. First, let us describe the various elements involved in the problem.

Coordinate Systems and Time Convention. The main coordinate system is the rectangular system $(\hat{x}, \hat{y}, \hat{z})$, whose origin is chosen at the source point P_0 and the z -coordinate is in the direction of the beam maximum of the antenna. Other coordinate systems at points P_1 , P_2 and P_3 along the ray are defined later. The field is time-harmonic with the time factor $\exp(+j\omega t)$ which is suppressed throughout.

Source. We assume that the source has a well-defined "phase center" at point P_0 , the origin of the coordinate system $(\hat{x}, \hat{y}, \hat{z})$, and radiates a spherical wave denoted by (\hat{E}^1, \hat{H}^1) . If the antenna is an array of point sources, it is necessary to consider each element in the array separately and superimpose their final fields at the observation points.

Dielectric radome. The radome is a dielectric shell with nonuniform thickness of relative dielectric constant $\epsilon_r = \epsilon/\epsilon_0$ or refraction index $n = \sqrt{\epsilon_r}$, and is bounded by the inner and outer surfaces Σ_1 and Σ_2 , respectively. The inner surface Σ_1 (near the source) is described by the equation:

$$z = f_1(x, y) \quad , \quad \text{for } a_1 < x < b_1 \text{ and } c_1 < y < d_1 . \quad (2.1)$$

The outer surface Σ_2 is given by the equation:

$$z = f_2(x, y) \quad , \quad \text{for } a_2 < x < b_2 \text{ and } c_2 < y < d_2 \quad . \quad (2.2)$$

It is not necessary to know the analytical form of the functions $f_1(x, y)$ and $f_2(x, y)$. In computation, only a set of discrete data points (x_n, y_n, f_n) with $n = 1, 2, \dots, N$ is needed for the description of f (f_1 or f_2). These points are fitted by a cubic spline which gives automatically first and second partial derivatives of f , i.e., $\partial f / \partial x$, $\partial f / \partial y$, $\partial^2 f / \partial x^2$, $\partial^2 f / \partial x \partial y$, and $\partial^2 f / \partial y^2$. There are two requirements for the cubic-spline fit:

(i) the data points can be distributed over a random grid, but they must be dense enough to describe the fine details of Σ (Σ_1 or Σ_2); (ii) the domain of the data points ($a < x < b$ and $c < y < d$) must be somewhat greater than the area of Σ in which the incident ray is expected to intersect the radome.

Observation points. Observation point P_3 is located on a prespecified surface Σ_3 , which can be either one of the following two types:

(i) Spherical Σ_3 with center at P_0 and an infinitely large radius.

In this case, P_3 is in the far field, and the field at P_3 calculated by the ray technique is the final result.

(ii) Planar Σ_3 which is just outside the radome and normal to the z -axis. In this case, we have to integrate the field on Σ_3 to obtain the far field.

In later calculations, we use mostly the spherical Σ_3 in (i).

III. FIELD SOLUTION BY GEOMETRICAL OPTICS

For a given incident field (\vec{E}^i, \vec{H}^i) generated by the source at point P_0 (Fig. 4), the asymptotic solution of the field at point P_1 is determined using geometrical optics [3], [4]. The method of solution is described below.

A. Method of Solution

Consider a ray in direction (θ, ϕ) extending from the source point P_0 to the point P_1 on Σ_1 . The source region (Region I) is homogeneous and isotropic; hence, the ray is a straight line along the unit vector \vec{r}_{01} . First, the distance r_{01} is found and the coordinates of point P_1 are determined. Then the unit vector \vec{N}_1 normal to the surface Σ_1 at point P_1 is found (Figure 5). The plane of vectors \vec{r}_{01} and \vec{N}_1 establishes the incident plane. The angle between these two vectors is the incident angle α_1^i . Using Snell's law, the refraction angle α_1^t is obtained, which establishes the direction of the transmitted wave, \vec{r}_{12} , in Region II (dielectric). The ray in Region II is a straight line along the unit vector \vec{r}_{12} . Three coordinate systems $(\vec{x}_1^i, \vec{y}_1^i, \vec{r}_{01})$, $(\vec{u}_1, \vec{v}_1, \vec{N}_1)$, and $(\vec{x}_1^t, \vec{y}_1^t, \vec{r}_{12})$, with common origin at point P_1 , are then established. They belong to the incident ray, the surface Σ_1 , and the transmitted ray, respectively.

The incident field $(\vec{E}_1^i, \vec{H}_1^i)$ is split into a normally polarized field $(\vec{E}_1^{in}, \vec{H}_1^{ip})$, (E-vector normal to the incident plane at P_1) and a parallel polarized field $(\vec{E}_1^{ip}, \vec{H}_1^{in})$. The transmitted field at point P_1 is obtained as follows:

$$\vec{E}_1^{tn} = r_1^n \vec{E}_1^{in} \quad , \quad \vec{H}_1^{tp} = Y \vec{r}_{12} \times \vec{E}_1^{tn}$$

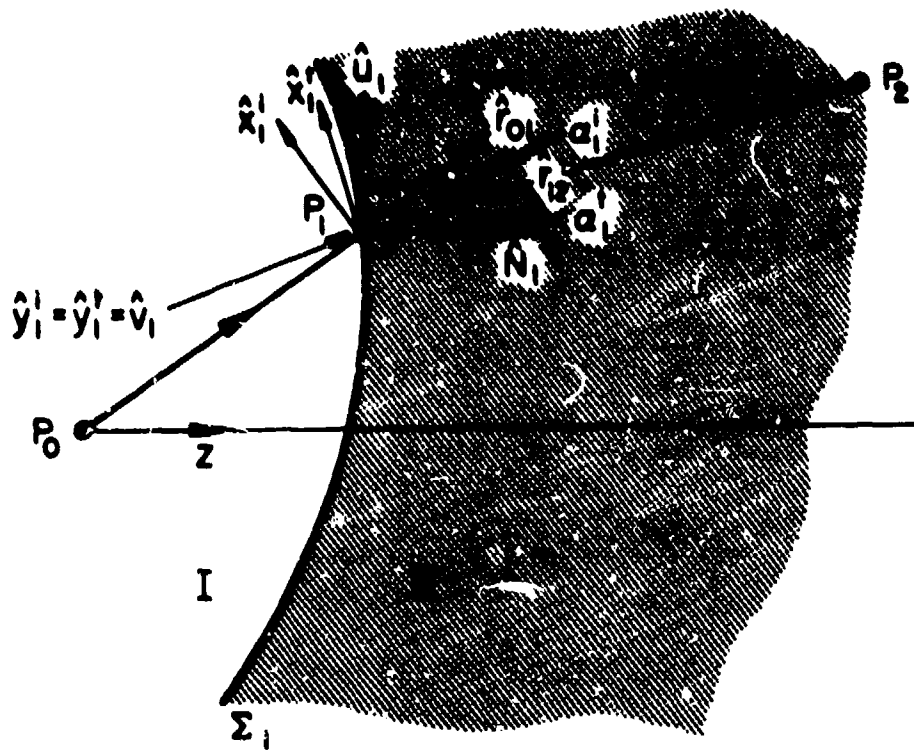


Figure 5. Coordinate systems for refraction at surface Σ_1 .

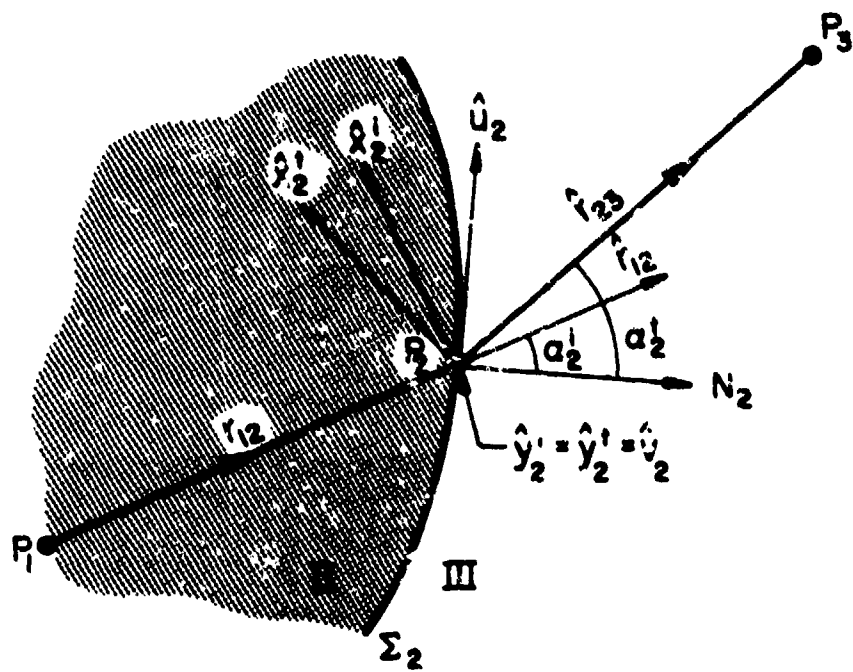


Figure 6. Coordinate systems for refraction at surface Σ_2 .

$$\hat{H}_1^{tn} = t_1^n \hat{H}_1^{in} , \quad \hat{E}_1^{tp} = z \hat{H}_1^{in} \times \hat{r}_{12} \quad (3.1)$$

in which t_1^n and t_1^p are transmission coefficients for the normal and parallel polarized fields, respectively,

$$\begin{aligned} t_1^n &= \frac{2}{1 + v_{nl}} , \quad v_{nl} = \frac{Y \cos \alpha_1^t}{Y_0 \cos \alpha_1^i} = n \frac{\cos \alpha_1^t}{\cos \alpha_1^i} \\ t_1^p &= \frac{2}{1 + v_{pl}} , \quad v_{pl} = \frac{Z \cos \alpha_1^t}{Z_0 \cos \alpha_1^i} = n \frac{\cos \alpha_1^t}{\cos \alpha_1^i} \end{aligned} \quad (3.2)$$

$$Y_0 = \frac{1}{Z_0} = \sqrt{\frac{\epsilon_0}{\mu_0}} = \frac{1}{120\pi} , \quad Y = \frac{1}{Z} = \sqrt{\frac{\epsilon}{\mu_0}} = nY_0 , \quad n = \sqrt{\frac{\epsilon}{\epsilon_0}} = \sqrt{\epsilon_r} .$$

Note that the subscript 1, in \hat{H}_1^{tn} for example, signifies the field evaluated at point 1.

The transmitted field at P_1 is incident on E_2 at point P_2 . Coordinates of this point can be found from the knowledge of the coordinates of point P_1 and the transmitted ray direction \hat{r}_{12} . The field values, in going from P_1 to P_2 , undergo some change which is dependent on the divergence of the ray. Thus, we have

$$\hat{E}_2^i = (DF_{12}) e^{-jkr_{12}} \hat{E}_1^t \quad (3.3)$$

in which $k = nk_0$ is the wave number in the dielectric and DF_{12} is the divergence factor for the pencil of rays travelling from P_1 to P_2 in the dielectric. It is given in [3], as

$$DF_{12} = (1 + q_1^{II} r_{12})^{-1/2} (1 + q_2^{II} r_{12})^{-1/2} \quad (3.4)$$

in which q_1^{II} and q_2^{II} are the principal curvatures (inverse of the radii of curvature) for the ray pencil in Region II. They are found from the curvature matrix of the transmitted ray at point P_1 . The matrix itself is found from a formula involving the curvature matrix of the incident ray and that of the surface Σ_1 at point P_1 . The curvature matrix of the transmitted ray pencil at point P_1 is also used to find the curvature matrix of the ray at point P_2 incident upon the surface Σ_2 .

Having the field incident upon Σ_2 at point P_2 , the ray direction \vec{r}_{12} , and its curvature matrix, we can proceed, in a manner similar to the transmission through Σ_1 , to find the field transmitted through Σ_2 at P_2 (Figure 6). Thus, a unit vector \vec{N}_2 , normal to Σ_2 is obtained, and together with \vec{r}_{12} defines the incidence plane at point P_2 . The incidence angle α_2^i ($\cos \alpha_2^i = \vec{N}_2 \cdot \vec{r}_{12}$) is then calculated. Again, Snell's law is invoked to find the refraction angle α_2^t at P_2 . This angle specifies the ray direction \vec{r}_{23} in Region III (outside the radome). Three coordinate systems $(\vec{x}_2^i, \vec{y}_2^i, \vec{r}_{12})$, $(\vec{u}_2^i, \vec{v}_2^i, \vec{N}_2)$ and $(\vec{x}_2^t, \vec{y}_2^t, \vec{r}_{23})$ with common origin at point P_2 are then introduced.

The field $(\vec{E}_2^i, \vec{H}_2^i)$ incident upon Σ_2 at P_2 is resolved into parallel and normally polarized fields, from which the transmitted fields are found as follows:

$$\begin{aligned} \vec{E}_2^{tn} &= \epsilon_2^n \vec{E}_2^i & \vec{H}_2^{tp} &= Y_0 \vec{r}_{23} \times \vec{E}_2^{tn} \\ \vec{H}_2^{tn} &= \epsilon_2^p \vec{H}_2^i & \vec{E}_2^{tp} &= Z_0 \vec{H}_2^{tn} \times \vec{r}_{23} \end{aligned} \quad (3.5)$$

in which

$$t_2^n = \frac{2}{1 + v_{n2}} , \quad v_{n2} = \frac{1}{n} \frac{\cos \alpha_2^t}{\cos \alpha_2^i}$$

$$t_2^p = \frac{2}{1 + v_{p2}} , \quad v_{p2} = n \frac{\cos \alpha_2^t}{\cos \alpha_2^i} . \quad (3.6)$$

The field at observation point P_3 is then found from the transmitted field at P_2 , such that,

$$\tilde{E}_3 = (DF_{23}) e^{-jk_0 r_{23}} \tilde{E}_2^t , \quad (3.7a)$$

in which

$$DF_{23} = (1 + q_1^{III} r_{23})^{-1/2} (1 + q_2^{III} r_{23})^{-1/2} , \quad (3.7b)$$

and q_1^{III} and q_2^{III} are the principal curvatures of the ray pencil in Region III. They are obtained from the curvature matrix of the transmitted ray at point P_2 . This matrix is obtained from a formula already mentioned in connection with transmission through E_1 . For a typical factor in Eqs. (3.4) and (3.7b), the following square root convention is used:

$$f = 1/\sqrt{1 + qr} = \begin{cases} +|f|, & \text{if } f \text{ is real} \\ +j|f|, & \text{if } f \text{ is imaginary} \end{cases} \quad (3.8)$$

It should be mentioned here that we have ignored multiple reflections in the dielectric radome throughout our analysis. Details of the analysis may be found in [5].

We now summarize the final results obtained so far. The point source at P_0 (Figure 4) radiates a spherical wave described by

$$\begin{aligned}
 \hat{\mathbf{E}}^1(r, \theta, \phi) &= \frac{-jk_0 r}{(r/\lambda_0)} (P(\theta, \phi)\hat{\mathbf{e}}_r + Q(\theta, \phi)\hat{\mathbf{e}}_\theta), \\
 &= \frac{-jk_0 r}{(r/\lambda_0)} [(P \cos\theta \cos\phi - Q \sin\phi)\hat{\mathbf{x}} + (P \sin\theta \cos\phi + Q \cos\phi)\hat{\mathbf{y}} - P \sin\theta\hat{\mathbf{z}}]
 \end{aligned} \tag{3.9a}$$

$$\hat{\mathbf{H}}^1 = Y_0 \hat{\mathbf{r}} \times \hat{\mathbf{E}}^1 \tag{3.9b}$$

where (r, θ, ϕ) are spherical coordinates with origin at P_0 . The pattern functions $P(\theta, \phi)$ and $Q(\theta, \phi)$ in (3.9) are given. At point P_1 (Figure 5), we decompose the field into two components in the directions of $(\hat{\mathbf{x}}_1^1, \hat{\mathbf{y}}_1^1)$, i.e.,

$$\hat{\mathbf{E}}_1^1 = \hat{\mathbf{E}}^1(r_1, \theta_1, \phi_1) = (\hat{\mathbf{E}}^1 \cdot \hat{\mathbf{x}}_1^1) \hat{\mathbf{x}}_1^1 + (\hat{\mathbf{E}}^1 \cdot \hat{\mathbf{y}}_1^1) \hat{\mathbf{y}}_1^1, \quad \hat{\mathbf{H}}_1^1 = Y_0 \hat{\mathbf{r}}_{01} \times \hat{\mathbf{E}}_1^1. \tag{3.10}$$

At the observation point P_3 , we express the field as follows

$$\hat{\mathbf{E}}_3^t = (\hat{\mathbf{E}}_3^t \cdot \hat{\mathbf{x}}_2^t) \hat{\mathbf{x}}_2^t + (\hat{\mathbf{E}}_3^t \cdot \hat{\mathbf{y}}_2^t) \hat{\mathbf{y}}_2^t, \quad \hat{\mathbf{H}}_3^t = Y_0 \hat{\mathbf{r}}_{23} \times \hat{\mathbf{E}}_3^t. \tag{3.11}$$

The two components of $\hat{\mathbf{E}}_3^t$ in (3.11) are found from the matrix equation

$$\begin{bmatrix} \hat{\mathbf{E}}_3^t \cdot \hat{\mathbf{x}}_2^t \\ \hat{\mathbf{E}}_3^t \cdot \hat{\mathbf{y}}_2^t \end{bmatrix} = (DF_{12})(DF_{23})^{-1} e^{-jk_0(nr_{12} + r_{23})} \begin{bmatrix} t_1^p t_2^p (\hat{\mathbf{x}}_2^t \cdot \hat{\mathbf{x}}_1^1) & n t_1^n t_2^p (\hat{\mathbf{x}}_2^t \cdot \hat{\mathbf{y}}_1^1) \\ n^{-1} t_1^p t_2^n (\hat{\mathbf{y}}_2^t \cdot \hat{\mathbf{x}}_1^1) & t_1^n t_2^n (\hat{\mathbf{y}}_2^t \cdot \hat{\mathbf{y}}_1^1) \end{bmatrix} \begin{bmatrix} \hat{\mathbf{E}}_1^1 \cdot \hat{\mathbf{x}}_1^1 \\ \hat{\mathbf{E}}_1^1 \cdot \hat{\mathbf{y}}_1^1 \end{bmatrix} \tag{3.12a}$$

or more compactly,

$$\hat{\mathbf{E}}_3^t = (DF) e^{-jk_0(nr_{12} + r_{23})} \hat{\mathbf{E}}_1^1. \tag{3.12b}$$

In (3.12), n is the refraction index of the dielectric, k_0 is the free-space wave number and $t_1^N, t_1^P, t_2^N, t_2^P$ are the normal and parallel transmission coefficients at points P_1 and P_2 , respectively, as given in (3.2) and (3.6). The two divergence factors are given in (3.4) and (3.7b). Their calculations constitute the major effort of the present solution.

IV. REFRACTION AT A CURVED DIELECTRIC INTERFACE

A. Introduction

The refraction at a dielectric interface is of fundamental importance in electromagnetic theory. If the interface is arbitrarily curved, the only available solution is the one derived by the geometrical optics theory (GO). Such a solution consists of two main ingredients: the well-known Fresnel formulas for the transmission and reflection coefficients (due to A. J. Fresnel in 1823) and a so-called "divergence factor DF." Surprisingly, the solution of DF was derived as early as 1915 by A. Gullstrand [6], but its application was not widely recognized in the electromagnetic/optical community until very recently. In 1972, Deschamps [3], [4] rederived Gullstrand's result by using "curvature matrices" for describing curved surfaces/wavefronts, thus resulting in greater clarity and simpler computations.

In this chapter, we supplement Deschamps' results by giving explicit formulas for calculating various curvature matrices and by illustrating the physical significance of DF via analytical and numerical examples. Another motivation for the present work is to compare our solution with the one described by Snyder and Love [7]-[9] for the same problem. It is shown that these two solutions are not in agreement. We believe that the Snyder-Love solution is incorrect.

B. Final Solution for the Refracted Fields

We begin with a statement of the problem. Two infinite dielectric media with refraction indices n_1 and n_2 are separated by a curved interface Σ (Figure 7), which is described by

$$\Sigma: z = f(x, y) . \quad (4.1)$$

The origin of the (x, y, z) coordinates is at the source point 0 in medium 1.

1. The source emits a spherical wave, whose electric field at an observation point $\vec{r} = (r, \theta, \phi)$ is given by [for $\exp(j\omega t)$ time convention]

$$\vec{E}^i(\vec{r}) = \frac{e^{-jk_1 r}}{r} [\hat{\theta}P(\theta, \phi) + \hat{\phi}Q(\theta, \phi)] \quad (4.2)$$

where $k_1 = 2\pi/\lambda_1 = n_1\omega/c$, and (r, θ, ϕ) are the spherical coordinates with origin at 0. The problem at hand is to find the transmitted field \vec{E}^t at a typical point 2 in medium 2, and the reflected field \vec{E}^r at a typical point 3 in medium 1.

We attack the problem by the geometrical optics theory (GO) [3], [4]. Referring to Figure 7, let us concentrate on a typical incident ray in the direction of \hat{z}_1 emanating from the source at 0. The "outward" normal to surface Σ at the refraction point 1 is \hat{N} . The plane defined by the ray 01 and \hat{N} is the plane of incidence. With respect to this plane, we resolve the incident field \vec{E}^i into two components: perpendicular component E_1^i and parallel component $E_{||}^i$. We introduce a scalar u^i such that

$$u^i = \begin{cases} E_1^i & , \text{ for perpendicular polarization} \\ E_{||}^i & , \text{ for parallel polarization} \end{cases} . \quad (4.3)$$

Similar decompositions and notations apply to \vec{E}^t and \vec{E}^r . Then, the final solution derived from GO has the following form

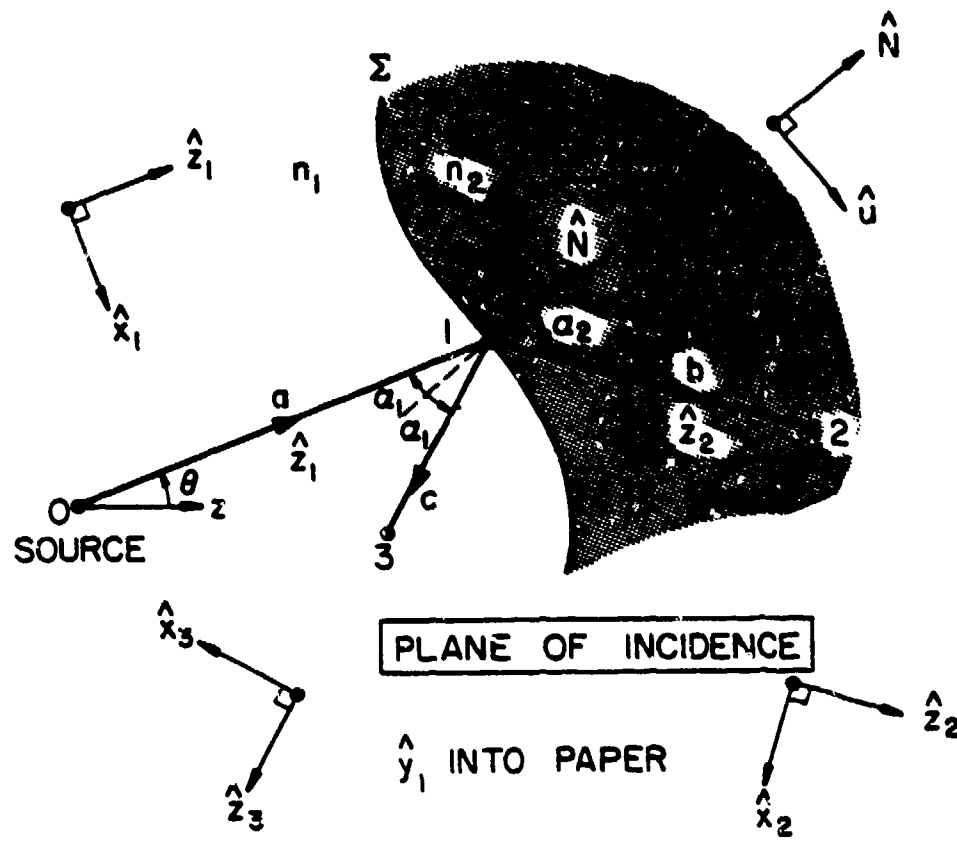


Figure 7. Refraction at a curved dielectric interface Σ .

$$u^t(2) = (DF)_2 T e^{-jk_2 b} u^i(1) \quad (4.4a)$$

$$u^r(3) = (DF)_3 R e^{-jk_1 c} u^i(1) . \quad (4.4b)$$

The various factors in (4.4) are explained below: T and R are the well-known Fresnel's transmission and reflection coefficients (for a planar interface), given by

$$T = \frac{2}{1+Y} , \quad R = \frac{1-Y}{1+Y} \quad (4.5)$$

where

$$Y = \begin{cases} n(\cos \alpha_2 / \cos \alpha_1) , & \text{for perpendicular polarization} \\ n^{-1}(\cos \alpha_2 / \cos \alpha_1) , & \text{for parallel polarization} \end{cases}$$

$$n = (n_2/n_1) = \text{relative refraction index.}$$

The incident angle α_1 and transmitted angle α_2 are related by the Snell's law

$$\sin \alpha_2 = \frac{1}{n} \sin \alpha_1 . \quad (4.6)$$

For $n < 1$, a critical incident angle α_c exists, where

$$\sin \alpha_c = n , \quad \text{if } n < 1 . \quad (4.7)$$

If $\alpha_1 > \alpha_c$, α_2 defined in (4.6) becomes complex and the simple ray picture shown in Figure 7 is lost. It is not immediately clear how the present GO solution must be modified. Therefore, in this paper, we exclude the case $\alpha_1 > \alpha_c$ when $n < 1$. The factor $(DF)_2$ in (4.4a) is the so-called "divergence factor" [3] of the transmitted ray pencil at point 2 in reference to point 1.

It is given by

$$(DF)_2 = \frac{1}{\sqrt{1 + (b/R_{21})}} \frac{1}{\sqrt{1 + (b/R_{22})}} . \quad (4.8)$$

Here (R_{21}, R_{22}) are the two principal radii of curvature of the transmitted wavefront passing through point 1. The sign convention of R_{21} (or R_{22}) is as follows: R_{21} is positive if the transmitted rays in the corresponding normal section are divergent, and R_{21} is negative if the transmitted rays are convergent. The square roots in (4.8) take either positive real or negative imaginary value. Thus, $(DF)_2$ is positive real (no focus between points 1 and 2 on the transmitted ray), positive imaginary (one focus between 1 and 2), or negative real (two foci between 1 and 2). The factor $(DF)_3$ in (4.4b) is the divergence factor of the reflected ray pencil at point 3 in reference to point 1. It is given by

$$(DF)_3 = \frac{1}{\sqrt{1 + (c/R_{31})}} \frac{1}{\sqrt{1 + (c/R_{32})}} . \quad (4.9)$$

The determination of the four principal radii of curvature $(R_{21}, R_{22}, R_{31}, R_{32})$ is the key to the present problem. In Section IV.C, we give an explicit, step-by-step description of their determination.

In summary, for the refraction problem in Figure 7, the final solutions for the fields of the transmitted and reflected rays are given in (4.4). This solution is based on GO. It is valid for high frequencies, and for all cases, except when total reflection occurs ($n < 1$ and $\alpha_1 > \alpha_c$).

C. Calculation of Curvatures of Refracted Wavefronts

For an arbitrary interface Σ and an arbitrary incident ray 01 (Figure 7), the calculation of the four radii of curvatures $(R_{21}, R_{22}, R_{31}, R_{32})$ is not a simple task. In this section, we present a systematic and explicit procedure for doing this calculation.

Coordinate systems at point 1. Consider a ray leaving the source at 0 in the direction (θ, ϕ) , which intersects the surface Σ described in (4.1) at point 1. The distance a is determined from the non-linear equation

$$a \cos \theta = f(x = a \sin \theta \cos \phi, y = a \sin \theta \sin \phi) . \quad (4.10)$$

The unit vector in the direction of the incident ray is

$$\hat{z}_1 = \hat{x} \sin \theta \cos \phi + \hat{y} \sin \theta \sin \phi + \hat{z} \cos \theta . \quad (4.11)$$

The unit normal \hat{N} of surface Σ at point 1 is

$$\hat{N} = \frac{1}{\Delta} (-f_x \hat{x} - f_y \hat{y} + \hat{z}) \quad (4.12)$$

where $\Delta = +(1 + f_x^2 + f_y^2)^{1/2}$, and f_x , for example, is the partial derivative of $f(x, y)$ with respect to x . By defining Δ positive, we have chosen \hat{N} in the forward direction with respect to the incident ray. Vectors \hat{z}_1 and \hat{N} define the plane of incidence. At point 1, we introduce four orthonormal base vectors:

$(\hat{x}_1, \hat{y}_1, \hat{z}_1)$ for the incident ray 01

$(\hat{x}_2, \hat{y}_2, \hat{z}_2)$ for the transmitted ray 12

$(\hat{x}_3, \hat{y}_3, \hat{z}_3)$ for the reflected ray 13

$(\hat{u}, \hat{v}, \hat{N})$ for the surface Σ .

We choose

$$\hat{y}_1 = \hat{y}_2 = \hat{y}_3 = \hat{v} = \hat{N} \times \hat{s}_1 \quad (4.13)$$

= a unit vector normal to the plane of incidence .

Then it follows

$$\hat{u} = \hat{v} \times \hat{N} , \hat{x}_n = \hat{y}_n \times \hat{s}_n \text{ for } n = 1, 2, 3 . \quad (4.14)$$

The incident, transmitted, and reflected rays are respectively in the directions

$$\hat{z}_1 = \hat{u} \sin \alpha_1 + \hat{N} \cos \alpha_1 \quad (4.15a)$$

$$\hat{z}_2 = \hat{u} \sin \alpha_2 + \hat{N} \cos \alpha_2 \quad (4.15b)$$

$$\hat{z}_3 = \hat{u} \sin \alpha_1 - \hat{N} \cos \alpha_1 \quad (4.15c)$$

where

$$\sin \alpha_2 = n^{-1} \sin \alpha_1 , \quad 0 \leq \alpha_1, \alpha_2 \leq \pi/2 . \quad (4.15d)$$

Note that, because of the particular choice in (4.13), both α_1 and α_2 are always positive, and have values in $(0, \pi/2)$.

Curvature matrix of surface Σ . At point 1 on surface Σ , the following two vectors lie in the tangent plane of the surface:

$$\hat{r}_{1x} = \hat{x} + f_x \hat{z} \quad (4.16a)$$

$$\hat{r}_{1y} = \hat{y} + f_y \hat{z} \quad (4.16b)$$

where (x, y, z) are evaluated at point 1. With respect to the base vectors $(\vec{r}_{1x}, \vec{r}_{1y})$, the curvature matrix of Σ is given by [10]

$$\tilde{Q}_\Sigma = \frac{1}{\Delta^2} \begin{bmatrix} e_1 G_1 - f_1 F_1 & f_1 E_1 - e_1 F_1 \\ f_1 G_1 - g_1 F_1 & g_1 E_1 - f_1 F_1 \end{bmatrix} \quad (4.17)$$

where $\Delta = +(\mathbf{1} + f_x^2 + f_y^2)^{1/2}$

$$E_1 = \mathbf{1} + f_x^2, \quad F_1 = f_x f_y, \quad G_1 = \mathbf{1} + f_y^2$$

$$e_1 = -\Delta^{-1} f_{xx}, \quad f_1 = -\Delta^{-1} f_{xy}, \quad g_1 = -\Delta^{-1} f_{yy}.$$

All (x, y, z) 's are evaluated at point 1. Now we transfer the curvature matrix with respect to $(\vec{r}_{1x}, \vec{r}_{1y})$ to that with respect to (u, v) , namely,

$$Q_\Sigma = \Lambda^{-1} \tilde{Q}_\Sigma \Lambda \quad (4.18)$$

where

$$\Lambda = \begin{bmatrix} \vec{r}_{1x} \cdot u & \vec{r}_{1x} \cdot v \\ \vec{r}_{1y} \cdot u & \vec{r}_{1y} \cdot v \end{bmatrix}.$$

It may be shown [10] that a principal radius calculated from (4.17) or (4.18) has a positive (negative) sign if the normal section of the surface bends away from (toward) the normal N . For example, if Σ is a sphere with radius ρ and the normal N points away from the sphere center, we have

$$Q_\Sigma = \tilde{Q}_\Sigma = \begin{bmatrix} \rho^{-1} & 0 \\ 0 & \rho^{-1} \end{bmatrix}. \quad (4.19)$$

We note that the present sign convention for the surface curvature is the same as that used in [4], but opposite to that in [3], [10].

Curvature matrices of wavefronts. The incident wavefront passing through point 1 is spherical with a radius a . Thus, its curvature matrix Q_1 with respect to base vectors (\hat{x}_1, \hat{y}_1) , or any other orthonormal base vectors, is

$$Q_1 = \begin{bmatrix} a^{-1} & 0 \\ 0 & a^{-1} \end{bmatrix} \quad . \quad (4.20)$$

The curvature matrices of the transmitted and reflected wavefronts passing through 1 are expressed with respect to base vectors (\hat{x}_2, \hat{y}_2) , and (\hat{x}_3, \hat{y}_3) , respectively. They are denoted by Q_2 and Q_3 . The solution of Q_2 is found from the following matrix equation [4]:

$$n \cdot \lambda_2 B_2 = B_1^T Q_1 B_1 + (n \cos \alpha_2 - \cos \alpha_1) Q_1 \quad (4.21)$$

where

$$B_1 = \begin{bmatrix} \hat{x}_1 \cdot \hat{u} & \hat{x}_1 \cdot \hat{v} \\ \hat{y}_1 \cdot \hat{u} & \hat{y}_1 \cdot \hat{v} \end{bmatrix} = \begin{bmatrix} \cos \alpha_1 & 0 \\ 0 & 1 \end{bmatrix}$$

$$B_2 = \begin{bmatrix} \hat{x}_2 \cdot \hat{u} & \hat{x}_2 \cdot \hat{v} \\ \hat{y}_2 \cdot \hat{u} & \hat{y}_2 \cdot \hat{v} \end{bmatrix} = \begin{bmatrix} \cos \alpha_2 & 0 \\ 0 & 1 \end{bmatrix} \quad .$$

The solution of Q_3 is found from the following matrix equation

$$B_3^T Q_3 B_3 = B_1^T Q_1 B_1 - 2(\cos \alpha_1) Q_1 \quad (4.22)$$

where

$$B_3 = \begin{bmatrix} \hat{x}_3 \cdot \hat{u} & \hat{x}_3 \cdot \hat{v} \\ \hat{y}_3 \cdot \hat{u} & \hat{y}_3 \cdot \hat{v} \end{bmatrix} = \begin{bmatrix} -\cos \alpha_1 & 0 \\ 0 & 1 \end{bmatrix} .$$

Principal radii of curvature of refracted wavefronts. Once matrices Q_2 and Q_3 are determined from (4.21) and (4.22), they may be diagonalized in a standard manner to find their eigenvectors (principal directions of the wavefront) and their eigenvalues (principal curvatures) [10]. In particular, the principal radii of the transmitted wavefront (R_{21}, R_{22}) are the roots of the following quadratic equation

$$\frac{1}{R^2} - \frac{1}{R} (\text{trace } Q_2) + \det. Q_2 = 0 \quad (4.23)$$

If Q_2 in (4.23) is replaced by Q_3 , the two roots are the radii (R_{31}, R_{32}) of the reflected wavefront.

D. Special Case: Spherical Interface

To illustrate the results obtained in the previous two sections, let us concentrate on a special case in which the interface Σ is spherical with radius $|\rho|$, as shown in Figure 8. Following our sign convention, the radius of curvature of Σ is

$$\rho = \begin{cases} +|\rho| & , \text{ if } \Sigma \text{ is concave when viewed from the source (Figure 8a)} \\ -|\rho| & , \text{ if } \Sigma \text{ is convex (Figure 8b)} \end{cases} \quad (4.24)$$

Without loss of generality, we assume that the incident ray from the source at point 0 is in the direction $(\theta, \phi = 0)$. The plane of incidence is then the $x - z$ plane. Making use of the formulas in Section IV.C, we find that the principal radii of the transmitted and reflected wavefronts passing through point 1 are

$$R_{21} = (n \cos^2 \alpha_2) \left[\frac{1}{a} \cos^2 \alpha_1 + \frac{1}{\rho} (n \cos \alpha_2 - \cos \alpha_1) \right]^{-1} \quad (4.25a)$$

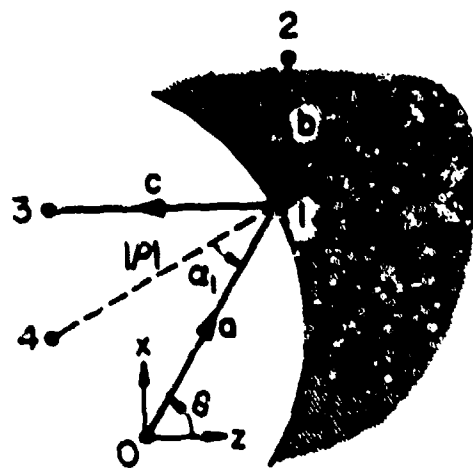
$$R_{22} = \left[\frac{1}{na} + \frac{1}{n\rho} (n \cos \alpha_2 - \cos \alpha_1) \right]^{-1} \quad (4.25b)$$

$$R_{31} = \left[\frac{1}{a} - \frac{2}{\rho \cos \alpha_1} \right]^{-1} \quad (4.26a)$$

$$R_{32} = \left[\frac{1}{a} - \frac{2 \cos \alpha_1}{\rho} \right]^{-1} \quad (4.26b)$$

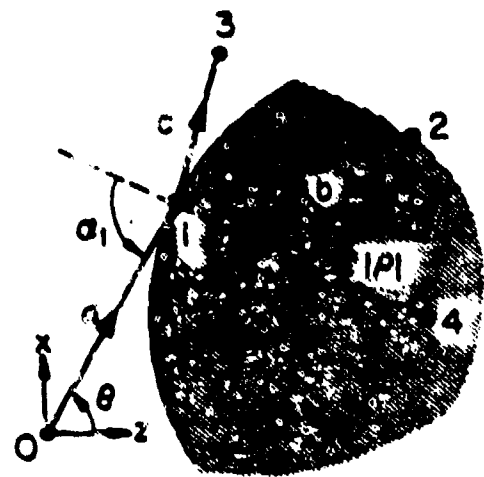
It can be shown that R_{21} and R_{31} are the radii of curvature of the normal sections in the $x - z$ plane (plane of incidence), whereas R_{22} and R_{32} are those in the orthogonal directions. Since in general $R_{21} \neq R_{22}$ and $R_{31} \neq R_{32}$, the refracted and reflected pencils are astigmatic.

POINT 0: SOURCE



(a) CONCAVE: $\rho = +1\rho_1$

POINT 4: CENTER OF Σ



(b) CONVEX: $\rho = -1\rho_1$

Figure 8. Refraction at a spherical dielectric interface.

(A) Normal incidence. For $a_1 = 0$, (4.25) and (4.26) become

$$R_{21} = R_{22} = n \left[\frac{1}{a} + \frac{n-1}{\rho} \right]^{-1} \quad (4.27)$$

$$R_{31} = R_{32} = \left[\frac{1}{a} - \frac{2}{\rho} \right]^{-1}. \quad (4.28)$$

Thus, for normal incidence, both refracted pencils have spherical wavefronts (no longer astigmatic). The relation in (4.27) may be rearranged to read

$$\frac{n}{R_{21}} = \frac{1}{a} + \frac{n-1}{\rho} \quad (4.29)$$

which is the well-known lens equation in optics. (See for example Eq. (40-14), p. 678 of [11].) Note the corresponding notations used in [11] and here: $n \rightarrow 1$, $n' \rightarrow n$, $s \rightarrow a$, $s' \rightarrow (-R_{21})$, and $R \rightarrow (-\rho)$.) The divergent incident pencil from a point source is converted into a convergent transmitted pencil in medium 2 when $R_{21} < 0$. This occurs when

$$a > \left(\frac{\rho}{1-n} \right) > 0. \quad (4.30)$$

If $\rho > 0$ (concave dielectric interface shown in Figure 8a), this is possible if $n = (n_2/n_1) < 1$. If $\rho < 0$ (convex dielectric interface shown in Figure 8b), this is possible if $n > 1$.

(B) Comparison with Synder and Love's result. In a recent article [7], Synder and Love consider the problem sketched in Figure 7 for an incident plane wave (source distance $a \rightarrow \infty$ in Figure 7). Their final result is in disagreement with ours. To show this disagreement, let us concentrate on a simple case (Figure 9): a concave, spherical, dielectric interface is illuminated by an incident plane wave which is given by

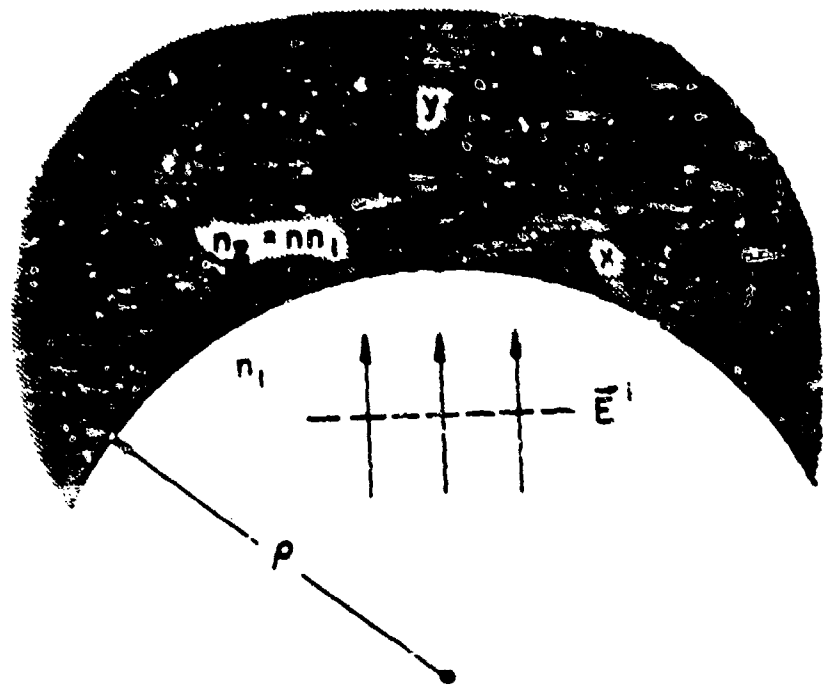


Figure 9. Refraction at a concave spherical dielectric interface of a normally incident plane wave.

$$\vec{E}^i(x, y, z) = z e^{-jk_1 y} . \quad (4.31)$$

The problem is to find the high-frequency solution of the refracted fields along the y -axis. Based on GO, our solution is given in (4.4), (4.5), (4.8), (4.9), (4.27), and (4.28) with $a = \infty$. Using the coordinate system in Figure 9, the transmitted and reflected fields are

$$\vec{E}^t(0, y, 0) = z \left[\frac{1}{1 + \left(\frac{n-1}{n} \right) \left(\frac{y}{\rho} \right)} \right] \frac{2}{1+n} e^{-jk_2 y} , \quad y > 0 \quad (4.32a)$$

$$\vec{E}^r(0, y, 0) = z \left[\frac{1}{1 - (2|y|/\rho)} \right] \frac{1-n}{1+n} e^{jk_1 y} , \quad y < 0 . \quad (4.32b)$$

The factors in [] in (4.32) are divergence factors. The intensity or power density of the incident field on the central ray (along $x = z = 0$) is given by

$$I^i = k_e(y \cdot (\vec{E}^i \times \vec{H}^{i*})) = (n_1/120\pi) \quad \text{watts/m}^2 \quad (4.33)$$

which is independent of y . This is due to the fact that the incident field is a plane wave and all incident rays are parallel. The intensity of the refracted field on the central ray does vary with y , namely,

$$\frac{I^t(y)}{I^i} = n \left(\frac{2}{1+n} \right)^2 \left[\frac{1}{1 + \left(\frac{n-1}{n} \right) \left(\frac{y}{\rho} \right)} \right]^2 , \quad y > 0 \quad (4.34a)$$

$$\frac{I^r(y)}{I^i} = \left(\frac{1-n}{1+n} \right)^2 \left[\frac{1}{1 - (2|y|/\rho)} \right]^2 , \quad y < 0 . \quad (4.34b)$$

At the focal point of the reflected pencil $y = -\rho/2$ in medium 1, the intensity I^r in (4.34b) predicted by the present GO becomes infinite as expected. For the same problem sketched in Figure 9, Snyder and Love's solution is given

in Eqs. (29) through (34) of [7]. For the case of normal incidence ($\alpha_1 = 0$) and central ray ($x = z = 0$), Snyder and Love's solution reads

$$\hat{E}_{SL}^t(0, y, 0) = z \frac{2}{1+n} , \quad r \gg y > 0 \quad (4.35a)$$

$$\hat{E}_{SL}^r(0, y, 0) = z \frac{1-n}{1+n} e^{jk_1 y} , \quad y < 0 \quad (4.35b)$$

which should be compared with our solution in (4.32). We note that (i) divergence factors $(DF)_2$ and $(DF)_3$ are missing in (4.35), and (ii) the propagation phase factor $\exp(-jk_2 y)$ is missing in (4.35a). Thus, we believe that (4.35) is incorrect. Furthermore, for each incident ray (fixed α_1), Snyder and Love define a "power transmission coefficient T_{SL} " by (Eq. (35a) of [7])

$$T_{SL} = 1 - \left[\frac{I^r}{I^i} \right] . \quad (4.36)$$

As may be seen from (4.34b), the intensity I^r is, in general, a function of position (x, y, z) , because of the divergence/convergence of the reflected ray pencil. Then, T_{SL} when calculated correctly is also a function of position, and does not have the usual significance associated with the "power transmission coefficient."

R. Numerical Results and Discussion

For the refraction problem sketched in Figure 7, the final solution for the transmitted field u^t into medium 2 is given in (4.4a), when the incident field is given in (4.2). In this section, we present some numerical results for u^t for various interfaces and source locations.

We consider three types of interfaces: the spherical interface described by

$$(z/\lambda_1) = 1 - [1 - (x^2 + y^2)/\lambda_1^2]^{1/2} , \quad (4.37)$$

the paraboloidal interface described by

$$(z/\lambda_1) = (x^2 + y^2)/2\lambda_1^2 , \quad (4.38)$$

and the hyperboloidal interface described by

$$(z/\lambda_1) = \frac{1}{2}[1 + 2(x^2 + y^2)/\lambda_1^2]^{1/2} - \frac{1}{2} \quad (4.39)$$

where λ_1 is the wavelength in medium 1 in which the source is located. For easy comparison, we have chosen the above interfaces such that they all have the same curvature in the axial direction (Figure 10). There are six source locations, indicated by numerals inside a small circle. When the source is at location 1, for example, medium 1 is on the right and medium 2 on the left, and the interface is concave. The source is assumed to be y-polarized. We calculate the transmitted field in the E-plane (plane normal to \hat{x}) and H-plane (plane normal to \hat{y}). In these two planes, the incident field is assumed to be

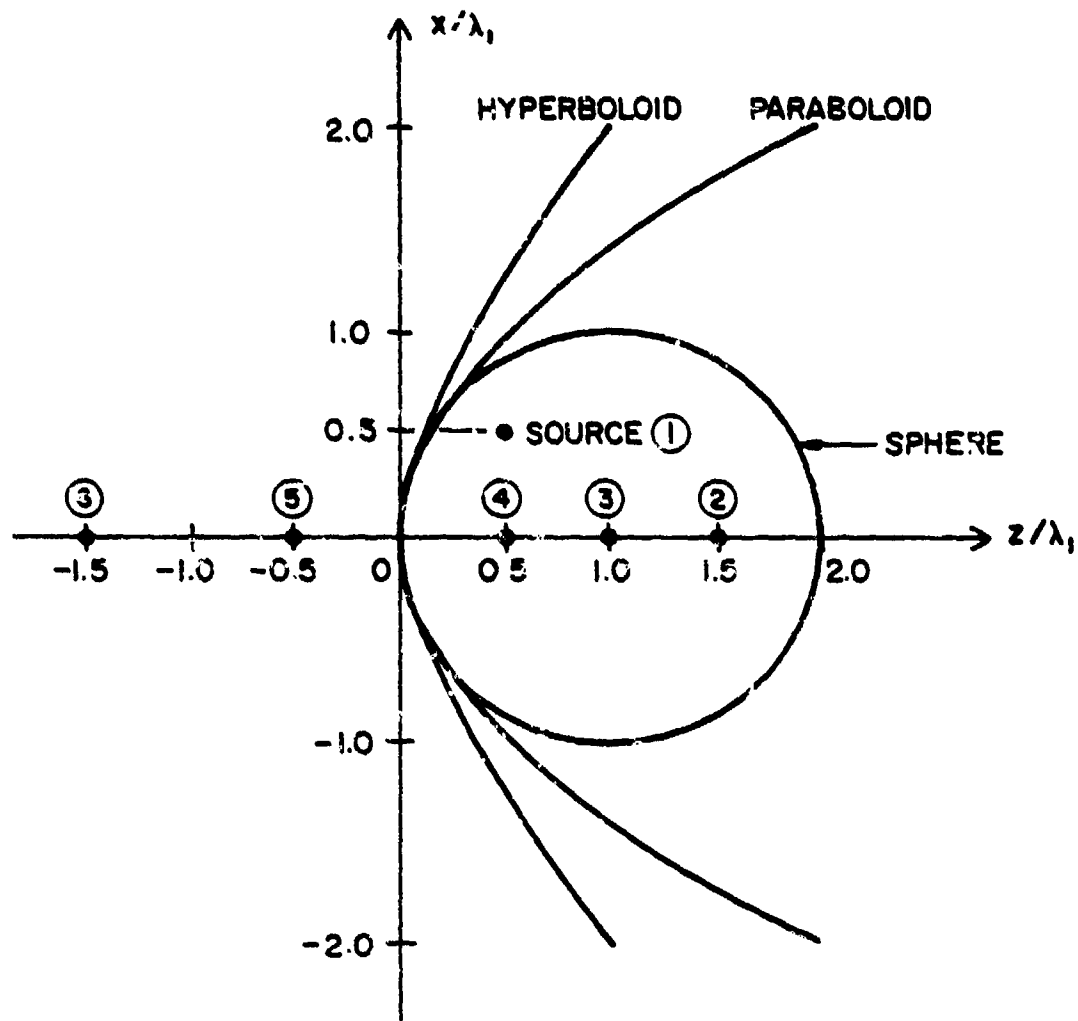


Figure 10. Three dielectric interfaces. At $z = 0$, all three interfaces have the same radius of curvature of $1 \lambda_1$.

$$\vec{E}^i(r) = \frac{-jk_1 r}{r} \begin{cases} \hat{\theta} 1, & \text{E-plane} \\ \hat{y} 1, & \text{H-plane} \end{cases} \quad (4.40)$$

Thus, in the E-plane, the \vec{E} -vector is parallel to the plane of incidence; whereas in the H-plane, the \vec{E} -vector is perpendicular. The observation point 2 is in medium 2 (Figure 7) with distance $b \rightarrow \infty$ (far zone).

We calculate the normalized far field defined by

$$EN = \left| \frac{\vec{E}^t(2)}{\vec{E}^i(2)} \right| = \left| \frac{\text{E-field when } n_1 \neq n_2}{\text{E-field when } n_1 = n_2} \right| \quad (4.41)$$

Substitute (4.4a) and (4.40) into (4.41). Under the condition $b \rightarrow \infty$, we have

$$EN = \frac{1}{a} \sqrt{R_{21} R_{22}} \quad , \quad b \rightarrow \infty \quad (4.42)$$

Here a is the distance between the source and the interface along the incident ray, and T is the Fresnel's transmission coefficient given in (4.5). The factor $\sqrt{R_{21} R_{22}}$ is the radius of the Gaussian curvature. In presenting the numerical results, we plot EN as a function of θ , where θ is the polar angle of observation point 2 measured from a line parallel to the z -axis and passing through the source point. The relative index $n = n_2/n_1$ is always set at 2 (transmission into a denser medium).

Concave spherical interface. Figures 11 and 12 show the E- and H-plane far-field pattern EN as a function of θ . Note that the field strengths increase as the source moves closer to the interface (smaller a). This is mainly due to the fact that EN is inversely proportional to a , according to (4.41). The Gaussian curvature $\sqrt{R_{21} R_{22}}$ decreases with a , but not enough to offset the factor $(1/a)$ in (4.41). For source 3, which is at the center

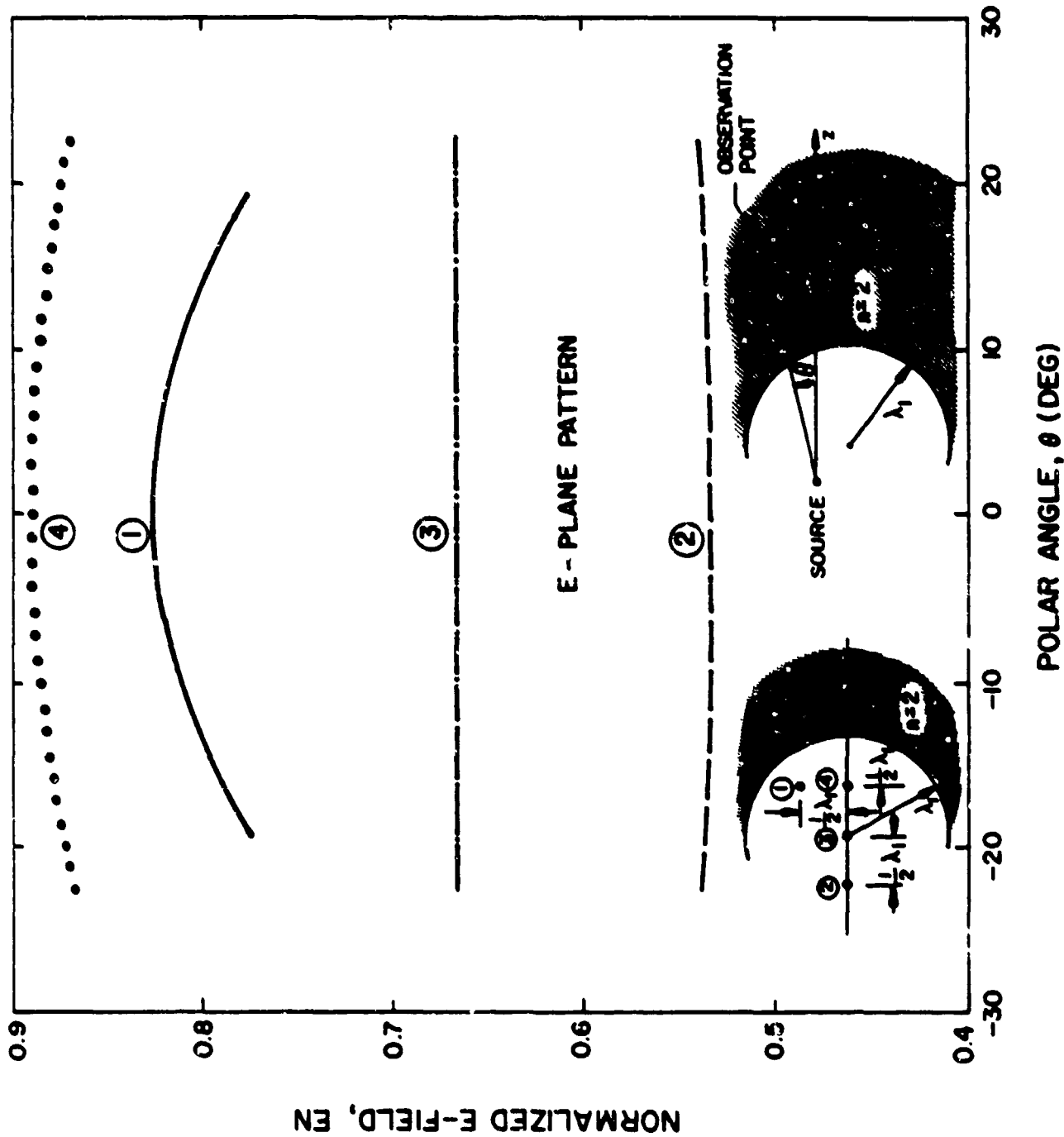


Figure 11. E-plane far field pattern through a concave spherical interface. The isotropic source is located at ①, ②, ③ or ④.

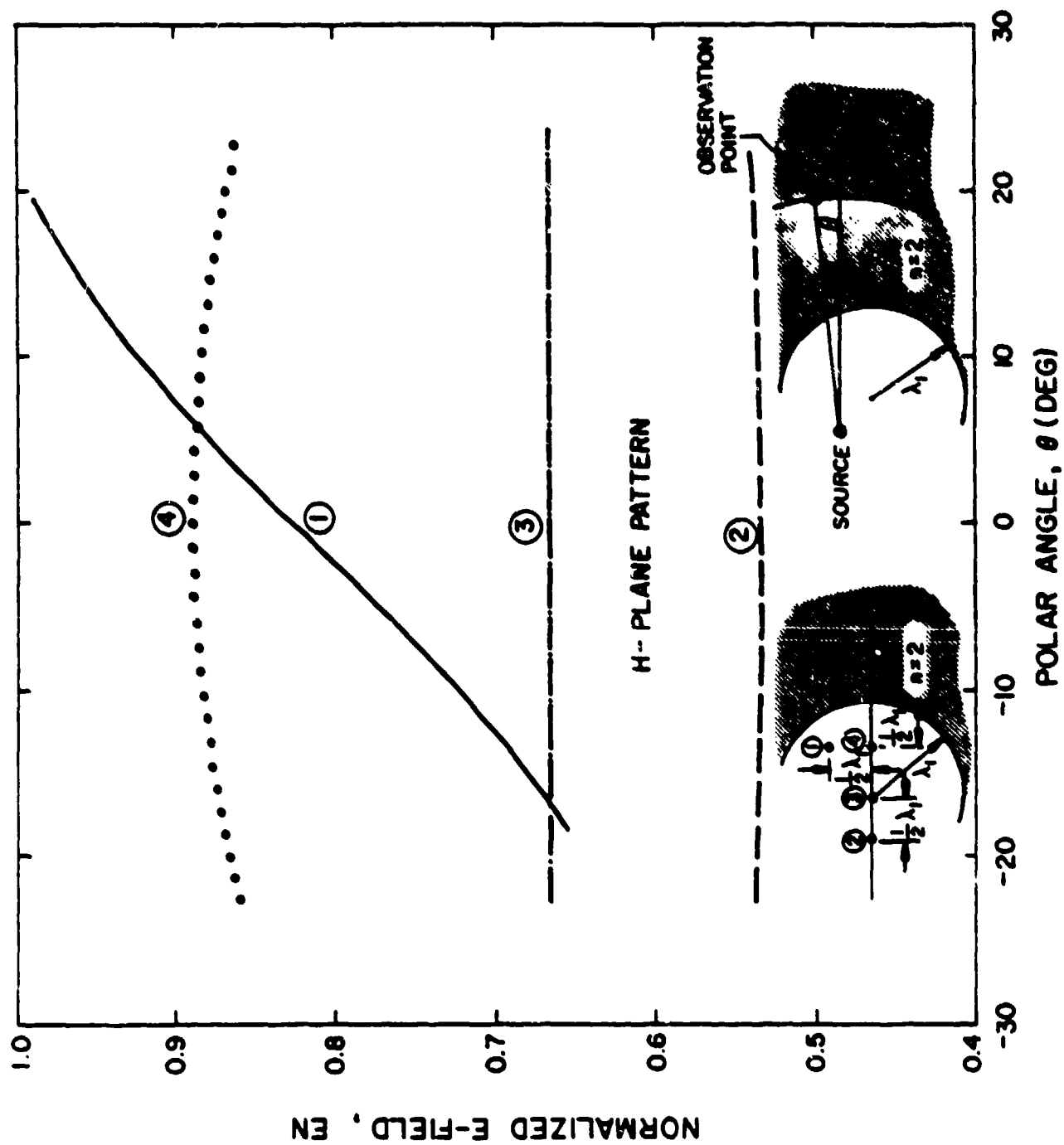


Figure 12. Same as Figure 11, except for H-plane pattern.

of the spherical interface, all of the incident rays are normal to the interface. It can be shown that $R_{21} = R_{22} = a$. Thus, EN calculated from (4.41) is equal to T , which is 0.667 for the present case of $n = 2$. Of particular interest is the H-plane pattern of source 1 shown in Figure 12. Note the marked asymmetry in the far-field pattern which is due to the asymmetry of the surface with respect to source 1. Figure 13 shows the variation of the axial far field when the source is moved along and parallel to the z-axis. It shows clearly the increase of the field as the source moves closer to the interface.

Concave paraboloidal interface (Figures 14 and 15). The far-field patterns for the concave paraboloid are quite similar to those for the spherical case. However, the pattern variations are more pronounced.

Concave hyperboloidal interface (Figures 16 and 17). Note that the far-field pattern due to source 4 has a dip instead of a peak in the axial direction. This is in contrast to the situations in Figures 11, 12, 14, and 15. There is another fact worth mentioning. Because of the choice of the same axial curvature for the above three interfaces, the axial field is the same for all interfaces when the source is at 2, 3, or 4. However, for source 1, which is displaced from the symmetry axis, the normalized axial field $\text{EN}(\theta = 0)$ increases from 0.826 for the spherical surface to 0.954 for the hyperboloid.

Convex interfaces. The E- and H-plane far-field patterns for a convex sphere, paraboloid and hyperboloid are shown in Figures 18 and 19 for source locations 5 and 6. The source locations 5 and 6 were chosen based on (4.30). Source 5 produces a divergent axial pencil in medium 2,

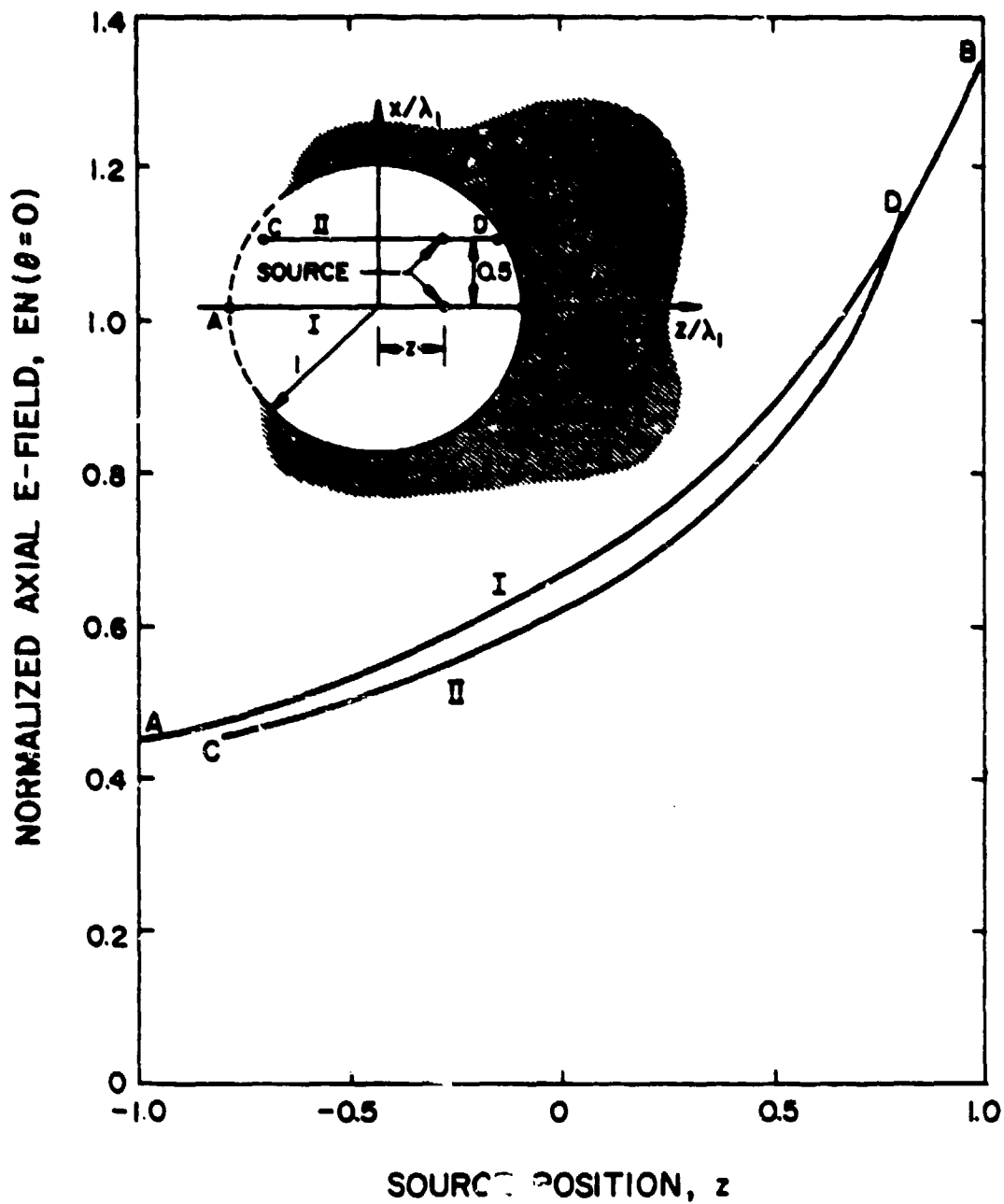


Figure 13. Axial far-field variation with source position for a concave spherical interface.

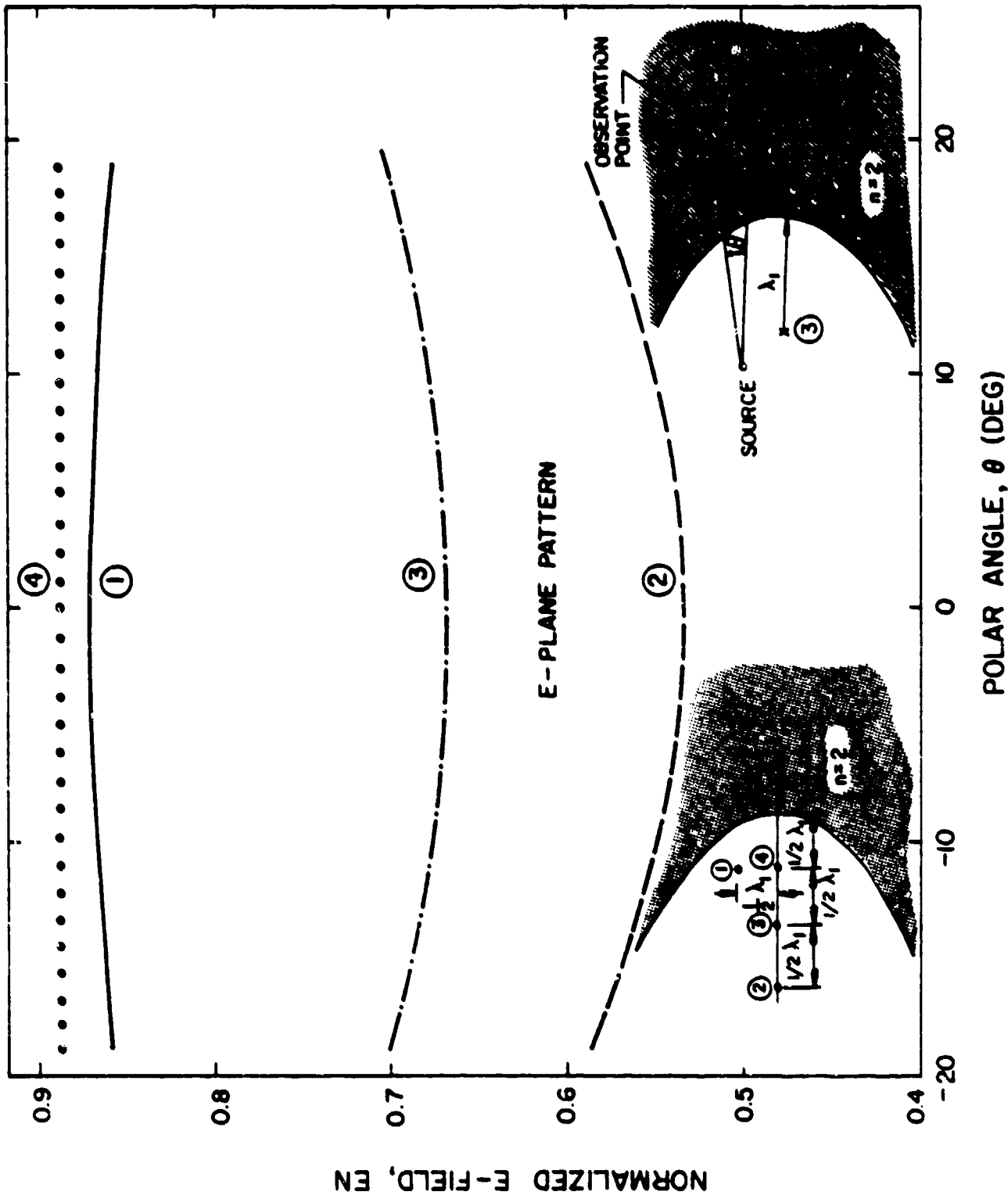


Figure 14. E-plane far-field pattern through a concave paraboloid.

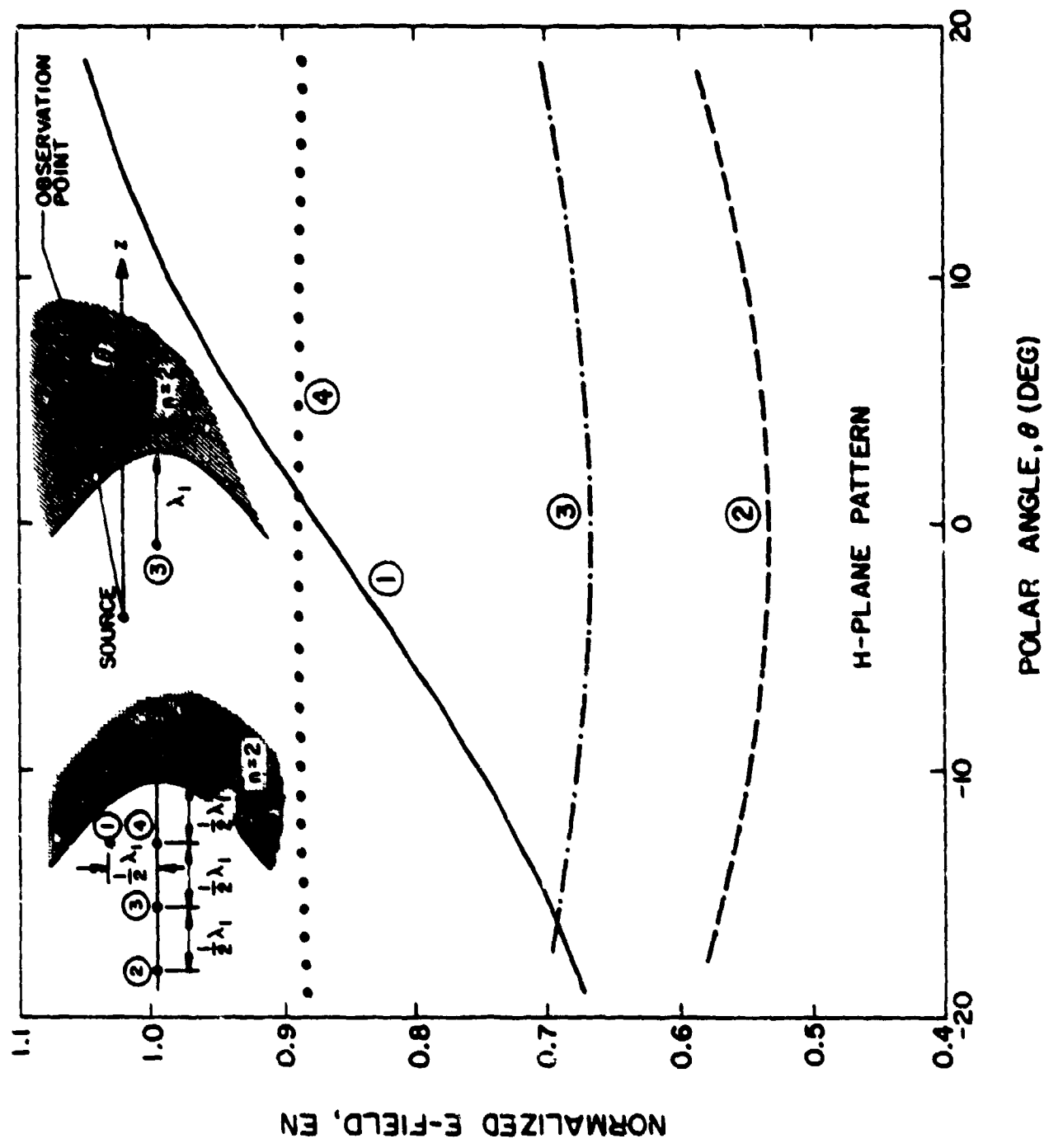


Figure 15. Same as Figure 14, except for H-plane pattern.

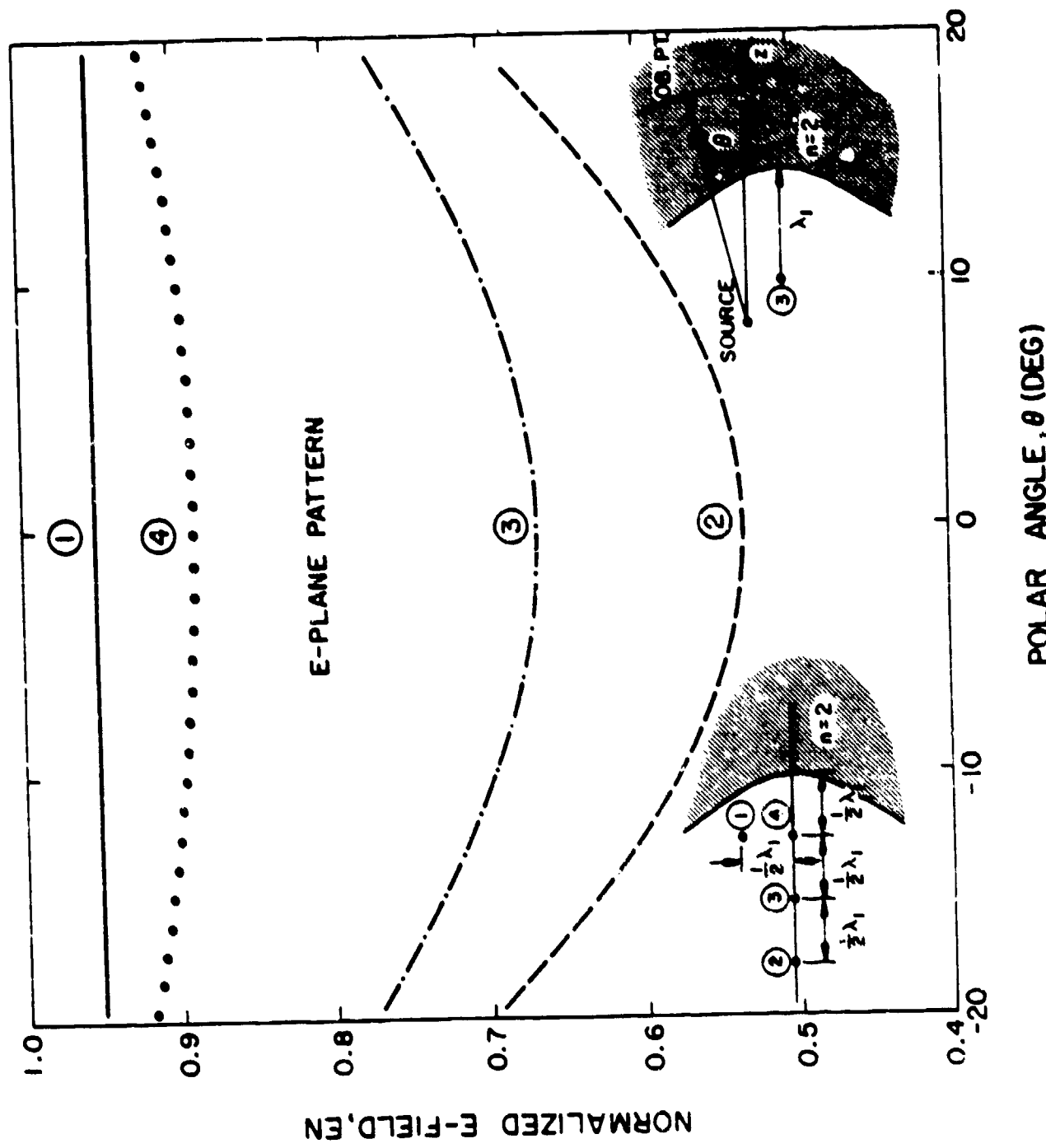


Figure 16. E-plane far-field pattern through a concave hyperboloid.

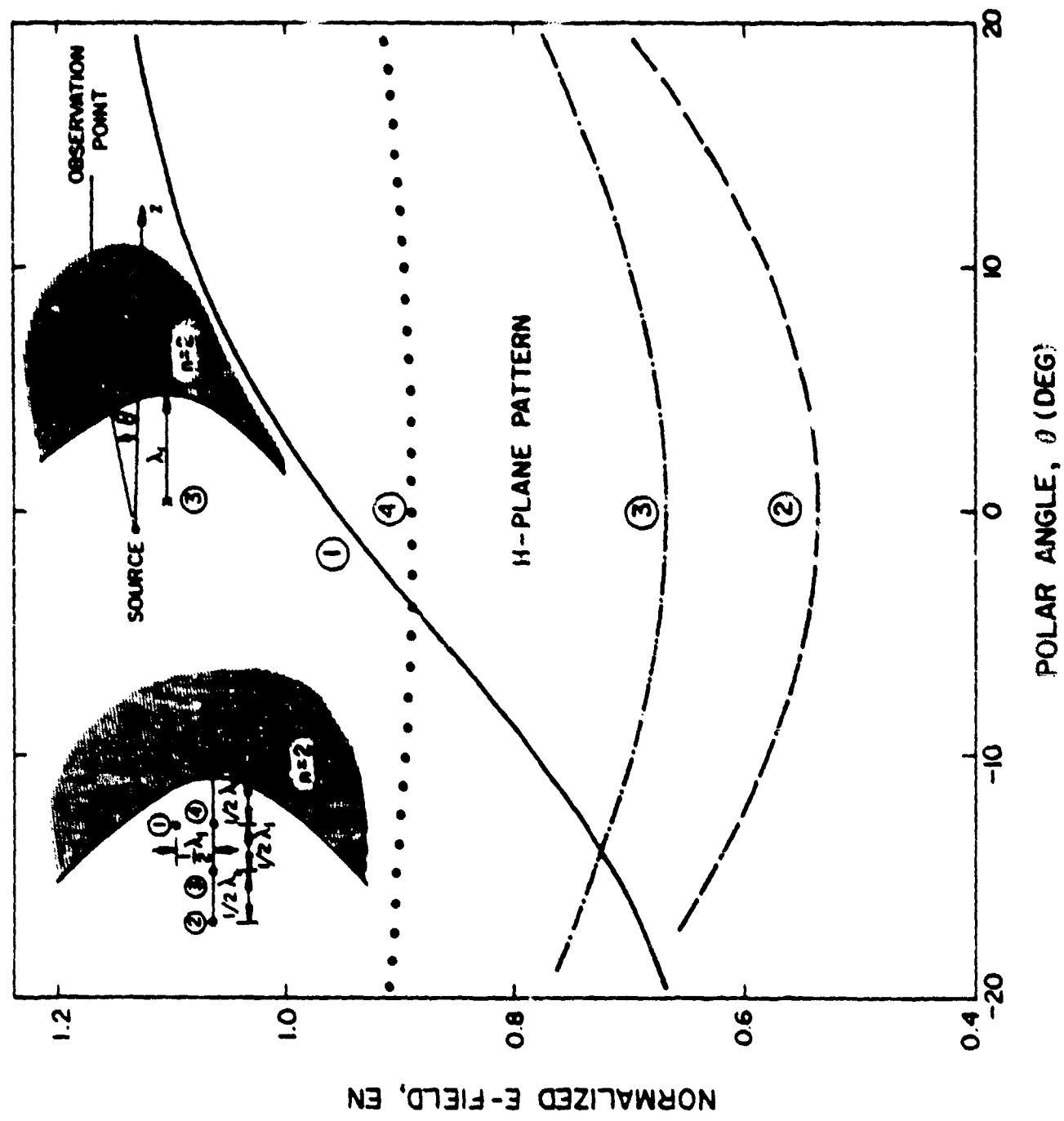


Figure 17. Same as Figure 16, except for H-plane pattern.

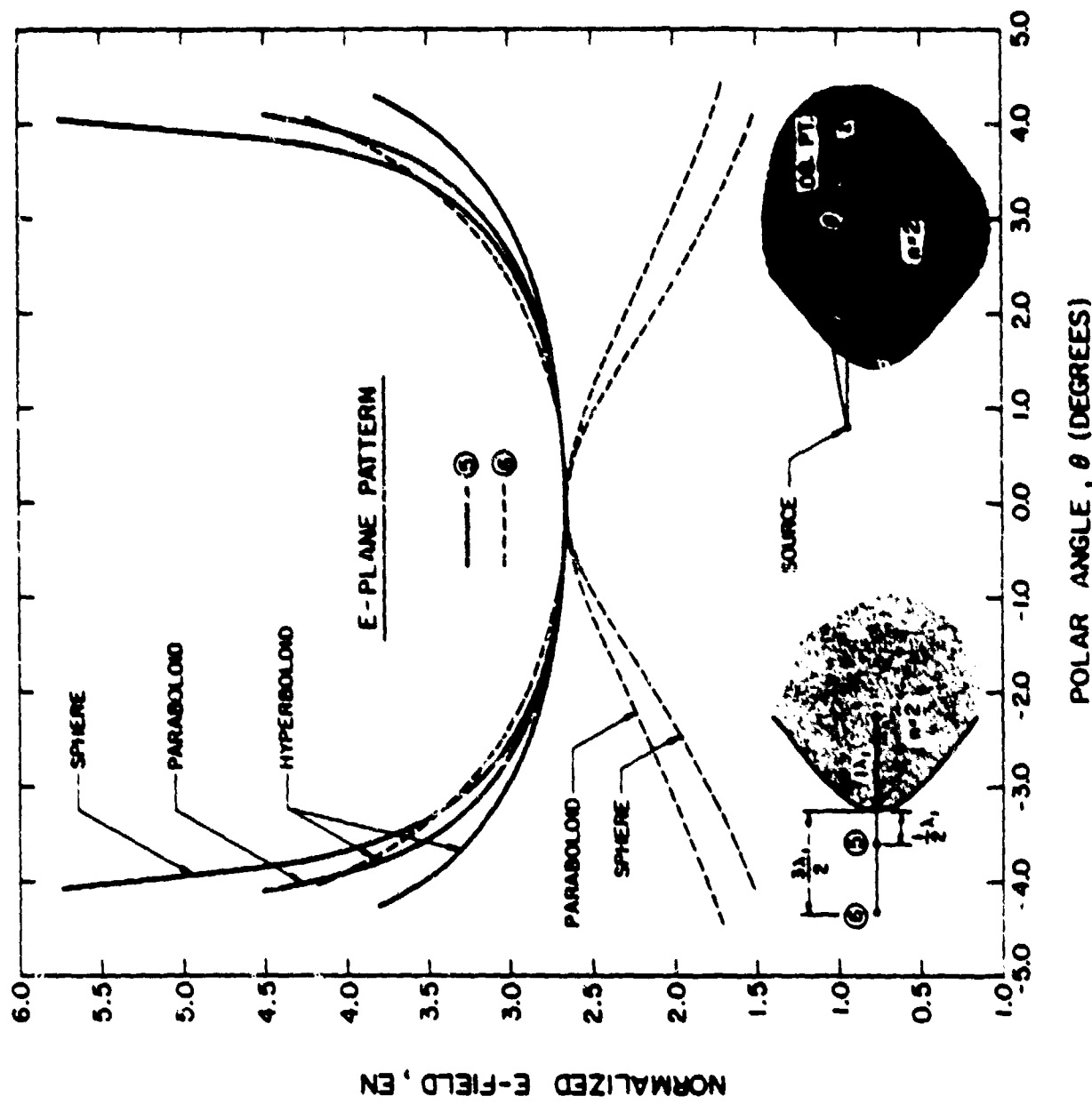


Figure 18. E-plane far-field patterns through convex interfaces.

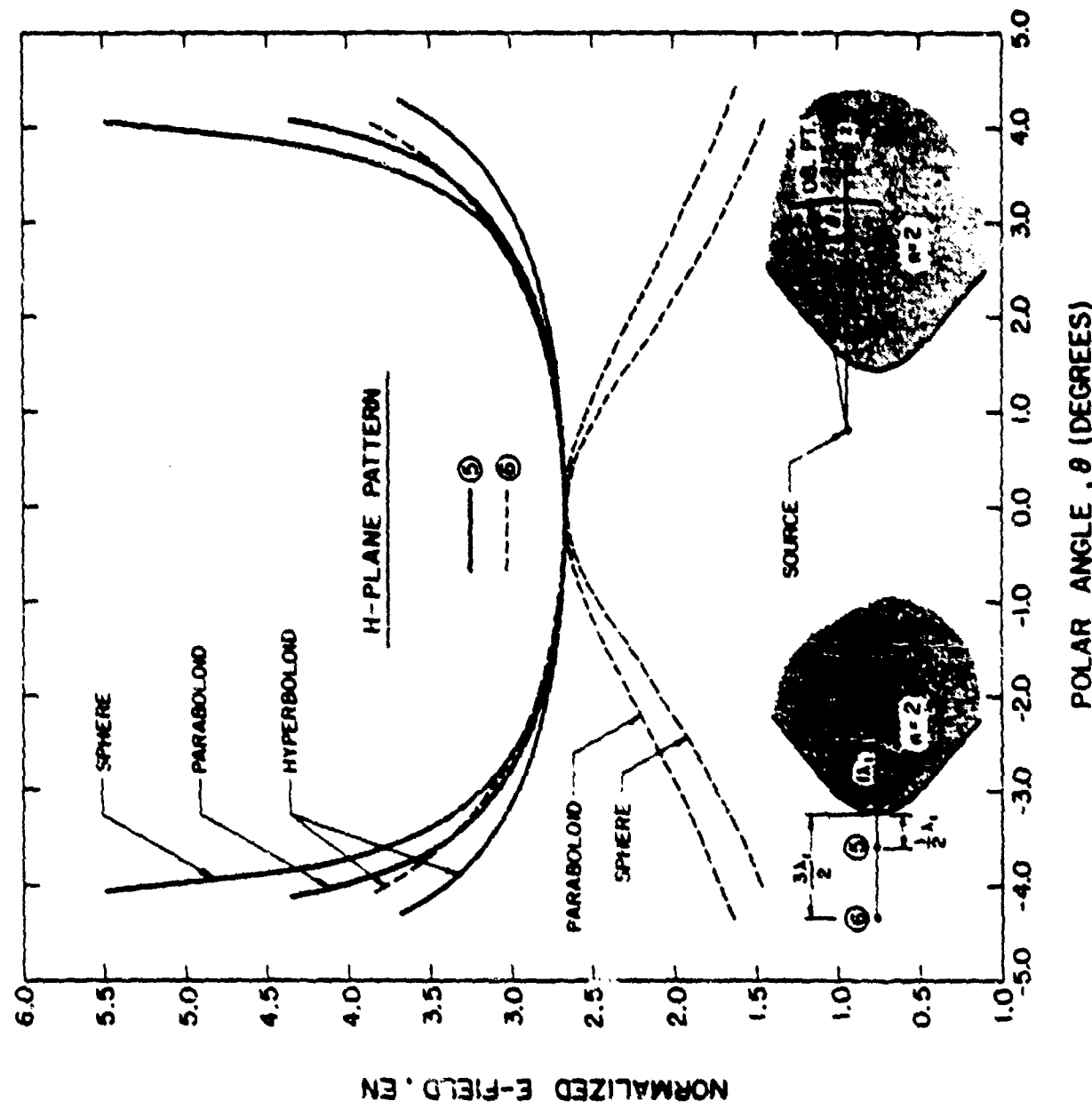


Figure 19. Same as Figure 12, except for H-plane pattern.

whereas source 6 produces a convergent axial pencil; the behavior in the non-axial direction is governed by the type of the interface. Thus, as may be seen from Figures 18 and 19, the far field in the axial direction through the spherical interface has a peak for source 6 and a dip for source 5. This is also the case for the paraboloid. However, this behavior is not observed in the hyperboloidal pattern.

For all the convex interfaces, the variation of EN as a function of θ in (4.41) is predominantly determined by the radius of the Gaussian curvature, $\sqrt{R_{21}R_{22}}$, and to a lesser extent by T or a .

Ray Picture. The H-plane pattern due to source 6 for a convex sphere is given in Figure 19. The corresponding ray picture is shown in Figure 20. We launch 6 rays at 4° apart in the upper half x-z plane ($x > 0$). The transmitted rays are first convergent, and after crossing the caustic surface, become divergent. The incident rays in the upper half x-z plane within a 20° angle give rise to transmitted rays in the lower x-z plane ($x < 0$) within a 13.5° angle. There are two caustic surfaces associated with the transmitted rays. The intersections of the caustic surfaces and the x-z plane are indicated by crosses and dots. Similar ray pictures can be drawn for the other cases also.

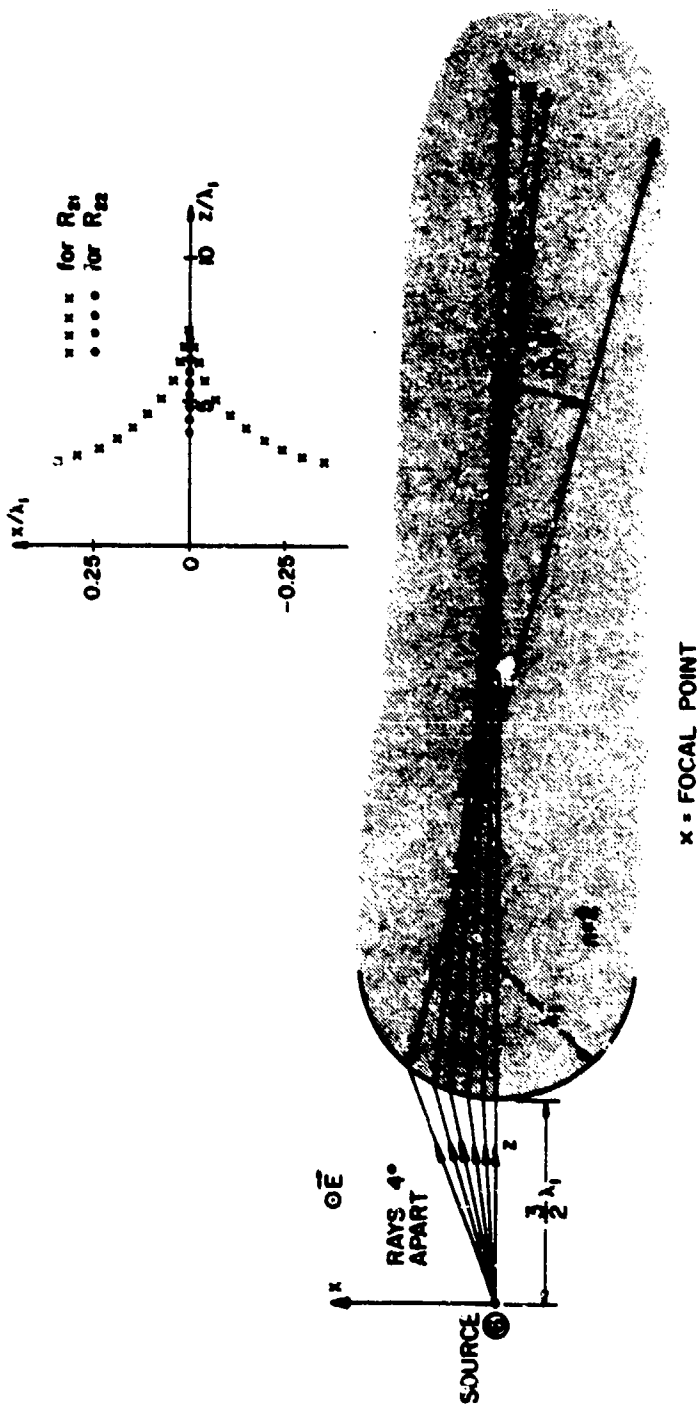


Figure 20. Ray picture and trace of foci of the transmitted rays which lie in the x-z plane, for the convex spherical interface with source at ⑥. The distance from the interface to a cross along a given ray represents R_{21} .

F. Conclusion

For the refraction problem sketched in Figure 7, the final geometrical-optics solutions for the transmitted field and the reflected field are given in (4.4). They are applicable under rather general conditions, namely, the dielectric interface described in (4.1) is arbitrary, and the incident field in (4.2) from a point source is arbitrary. A major step in calculating these solutions is the evaluation of the divergence factors in (4.8) and (4.9), which involves the matrix operation described by (4.21) and (4.22). Strictly speaking, the present solution is valid in the high-frequency limit $\omega \rightarrow \infty$; however, practical experience has shown that solutions of the present type are reasonably accurate as long as the radii of curvature of the dielectric interface are in the order of a wavelength or more.

V. WAVE TRANSMISSION THROUGH A SPHERICAL DIELECTRIC SHELL

A. Introduction

One of the fundamental problems in electromagnetic theory is the transmission of a spherical wave through a dielectric shell. This problem has numerous applications in antenna radomes, electromagnetic shielding, and scattering. It appears that solutions to this problem are available only for the special case where the shell is an infinite dielectric half space. That case was first studied by Sommerfeld in 1909, whereas later research was summarized in a book by Brekhovskikh (Chapter IV of [12]). In this chapter, we consider a more general case, namely, the shell has two spherical boundary surfaces. Unlike the Sommerfeld's problem, our case does include the effects of the shell's curvature and thickness. Therefore, its solution should be of more practical interest.

To solve our problem rigorously, the spherical wave expansion may be used. However, due to the fact that the source location and the two dielectric surface centers do not coincide, the translational addition theorem for vector spherical wave function [13] must be used. (Our problem is roughly comparable to scattering by three dielectric spheres.) This theorem leads to a complex series, which makes it very difficult to generate numerical results. In this paper, we use the geometrical optics theory (GO) [4], [14] to calculate the transmitted field in the problem sketched in Figure 21. Such a solution, though only approximately valid for high frequencies, is given in a simple closed form. Thus, it allows us to study the "cause and effect" of the various parameters in a convenient manner and gain physical insight.

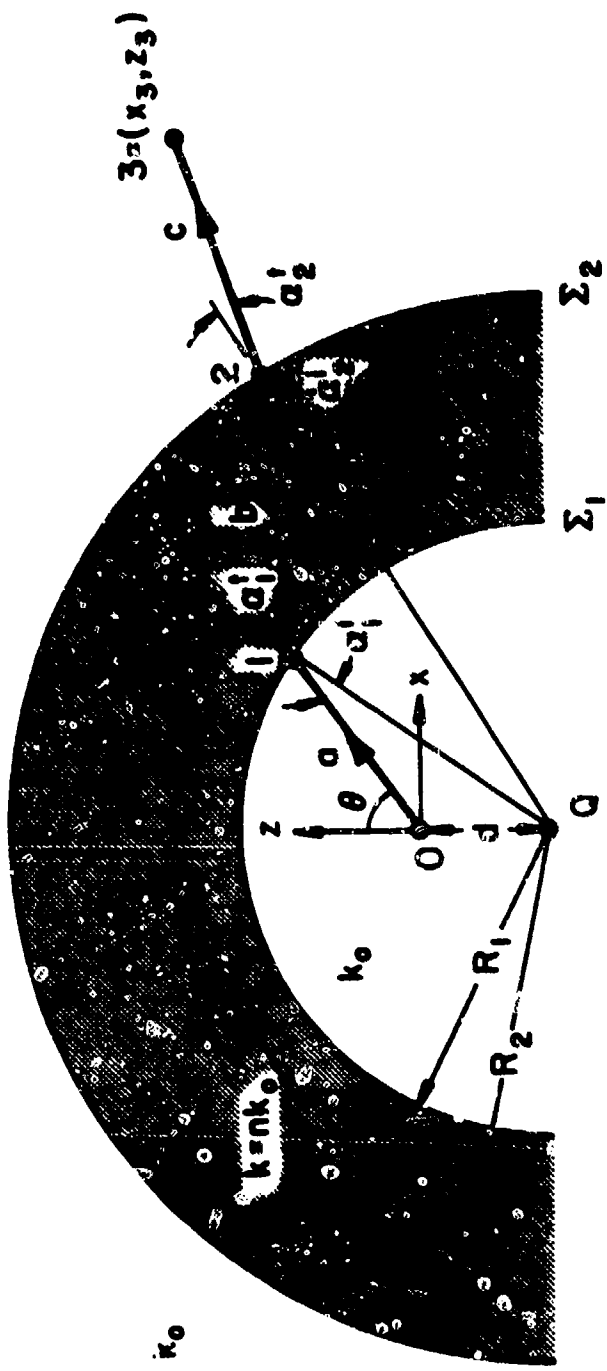


Figure 21. Transmission of a spherical wave emitted from source O through a spherical dielectric shell.

B. Solution for Concentric Spherical Shell

Let us consider the wave transmission problem in Figure 21. The boundary surfaces of the dielectric shell are two concentric spheres with radii R_1 and R_2 (both positive), and with a common center at Q . The point source at 0 emits a spherical wave described by (for exp j ω time convention)

$$\vec{E}^i(\vec{r}) = \frac{-jk_0 r}{r} [P(\theta, \phi)\hat{\theta} + Q(\theta, \phi)\hat{\phi}] . \quad (5.1)$$

Here, (r, θ, ϕ) are spherical coordinates of \vec{r} with origin at 0 . Functions P and Q describe the radiation pattern of the source. The wave number $k_0 = 2\pi/\lambda_0 = \omega(\mu_0 \epsilon_0)^{1/2}$ is that of free space. By using GO [4], [14], the transmitted field at an observation point 3 is to be determined. Without loss of generality, we assume that point 3 is in the (x, z) -plane with rectangular coordinates $(x_3, 0, z_3)$.

A. Ray Tracing. In accordance with Snell's law, we trace a ray from source point 0 to observation point 3 , via refraction points 1 and 2 (Figure 21). Clearly, all four points, 0 to 3 , lie in the same (x, z) -plane. For a given launching angle θ of the ray and the distance c , the other geometrical parameters can be determined from the following relations:

$$\sin \alpha_1^i = (d/R_1) \sin \theta , \quad a = R_1 [\sin(\theta - \alpha_1^i)] / \sin \theta \quad (5.2)$$

$$\sin \alpha_1^t = n^{-1} \sin \alpha_1^i , \quad \sin \alpha_2^i = (R_1/R_2) \sin \alpha_1^t$$

$$b = R_2 [\sin(\alpha_1^t - \alpha_2^i)] / \sin \alpha_1^t , \quad \sin \alpha_2^t = n \sin \alpha_2^i$$

$$x_3 = a \sin \theta + b \sin(\theta - \alpha_1^i + \alpha_1^t) + c \sin(\alpha_1^t + \alpha_2^t - \alpha_1^i - \alpha_2^i + \theta)$$

$$z_2 = a \cos \theta + b \cos (\theta - \alpha_1^i + \alpha_1^t) + c \cos (\alpha_1^t + \alpha_2^t - \alpha_1^i - \alpha_2^i + \theta).$$

Thus, for a given (θ, c) , we can determine the position of point 3 straightforwardly. On the other hand, when point 3 is given, explicit formulas do not exist for determining θ . One has to find θ by trial-and-error.

B. Field on the Ray. The present vector field problem can be decomposed into two scalar ones: one with the electric field vector perpendicular to the plane of incidence ($\vec{E} = \vec{E}_\perp$) and the other with the electric field vector parallel to the plane of incidence (\vec{E}_\parallel). The final solution for the transmitted field \vec{E}^t at point 3 derived by GO is given by

$$\vec{E}^t(3) = \begin{bmatrix} E_\perp^t(3) \\ E_\parallel^t(3) \end{bmatrix} = (DF) \begin{bmatrix} T_\perp E_\perp^i(1) \\ T_\parallel E_\parallel^i(1) \end{bmatrix} e^{-jk_0(n_b+c)}. \quad (5.3)$$

The various factors in (5.3) are explained below: T_\perp and T_\parallel are the products of the transmission coefficients at points 1 and 2, given by

$$T_\perp = 4 \left[1 + n \frac{\cos \alpha_1^t}{\cos \alpha_1^i} \right]^{-1} \left[1 + \frac{1}{n} \frac{\cos \alpha_2^t}{\cos \alpha_2^i} \right]^{-1} \quad (5.4a)$$

$$T_\parallel = 4 \left[1 + \frac{1}{n} \frac{\cos \alpha_1^t}{\cos \alpha_1^i} \right]^{-1} \left[1 + n \frac{\cos \alpha_2^t}{\cos \alpha_2^i} \right]^{-1}. \quad (5.4b)$$

The two components of the incident field are calculated from (5.1):

$$E_\perp^i(1) = \frac{-jk_0 a}{a} Q(\theta, \phi = 0) \quad (5.5a)$$

$$E_\parallel^i(1) = \frac{-jk_0 a}{a} P(\theta, \phi = 0). \quad (5.5b)$$

The derivation of the divergence factor DF in (5.3) requires some effort.

With the details given in Appendix A, the final result for DF reads

$$DF = (1 + \kappa_{11}b)^{-1/2} (1 + \kappa_{12}b)^{-1/2} (1 + \kappa_{21}c)^{-1/2} (1 + \kappa_{22}c)^{-1/2}, \quad (5.6)$$

At point 1 or 2, it can be shown that the principal directions of the transmitted wavefront are precisely the two directions parallel and perpendicular to the plane of incidence. Here $(\kappa_{11}, \kappa_{12})$ are the two principal curvatures of the transmitted wavefront at point 1, and $(\kappa_{21}, \kappa_{22})$ are those at point 2. They are calculated from the relations

$$\kappa_{11} = (n \cos^2 \alpha_1^t)^{-1} \left[\frac{1}{a} \cos^2 \alpha_1^i + \frac{1}{R_1} (n \cos \alpha_1^t - \cos \alpha_1^i) \right] \quad (5.7a)$$

$$\kappa_{12} = \frac{1}{na} + \frac{1}{R_1} (\cos \alpha_1^t - \frac{1}{n} \cos \alpha_1^i) \quad (5.7b)$$

$$\kappa_{21} = (\cos^2 \alpha_2^t)^{-1} [(b + \kappa_{11}^{-1})^{-1} n \cos^2 \alpha_2^i + \frac{1}{R_2} (\cos \alpha_2^t - n \cos \alpha_2^i)] \quad (5.7c)$$

$$\kappa_{22} = n(b + \kappa_{12}^{-1})^{-1} + \frac{1}{R_2} (\cos \alpha_2^t - n \cos \alpha_2^i) \quad (5.7d)$$

The sign convention of κ is as follows. If κ is positive (negative), the normal section of the wavefront is divergent (convergent). For example, if the transmitted wavefront at point 1 is the same as the incident spherical wavefront, we have $\kappa_{11} = \kappa_{12} = +R_1^{-1}$. For a typical factor in (5.6), the square root convention is

$$f = (1 + \kappa b)^{-1/2} = \begin{cases} +|f|, & \text{if } f \text{ is real} \\ +j|f|, & \text{if } f \text{ is imaginary} \end{cases} \quad (5.8)$$

When f is imaginary, it means that the ray has crossed a focus of the ray pencil. The $(+j)$ accounts for the well-known $(\pi/2)$ phase retardation.

Several general comments about the solution in (5.3) are in order:

(i) For the case where a total reflection occurs (a_1^t or a_2^t becomes complex), the field in the transmitted region is not an optical field, and the present ray solution (5.3) is no longer valid. (ii) Except for special cases, e.g., normal incidence $a_1^1 = 0$, the two curvatures (κ_{21}, κ_{22}) of the transmitted wavefront emerging from the dielectric shell are not equal. Thus, the transmitted pencil is generally astigmatic. (iii) It is possible that κ_{21} and/or κ_{22} are negative. Then the divergent pencil from the source is transformed into a convergent (focusing) pencil after propagating through the dielectric shell. (iv) The solution in (5.3) remains valid for more geometries than the one shown in Figure 21. This is discussed further in the next section.

C. Generalization of Final Solution

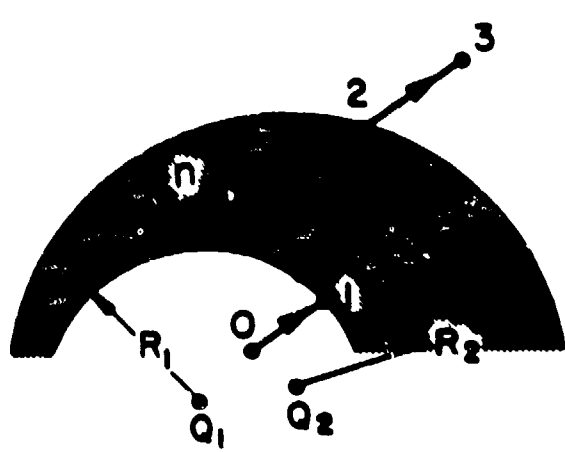
For transmission through the concentric spherical shell in Figure 21, the final solution consists of two parts:

Part A: Ray tracing formulas in (5.2)

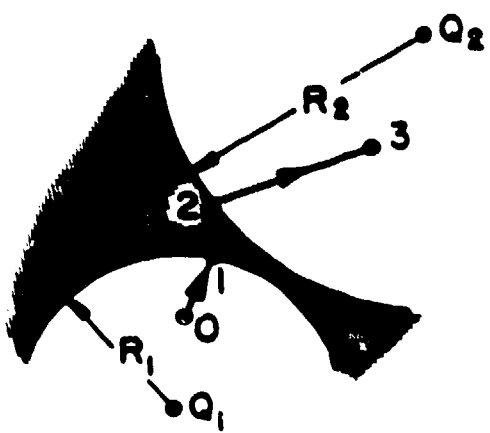
Part B: Field solution in (5.3) through (5.5)

It can be shown that Part B is valid under a more general condition (Figure 22), namely,

- (i) The centers of the spherical shells Q_1 and Q_2 need not coincide, as long as the four points (0,1,2,3) are coplanar.
- (ii) The surfaces of the shell can be either concave or convex. Looking from the source side, R_1 (or R_2) is positive if the surface is concave, and R_1 is negative if the surface is convex.

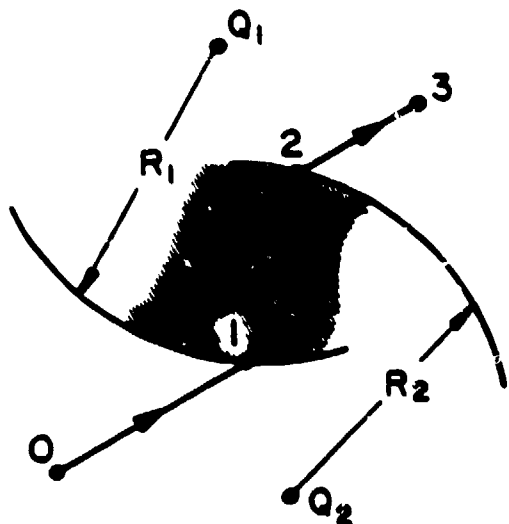


(a) $R_1 > 0, R_2 > 0$

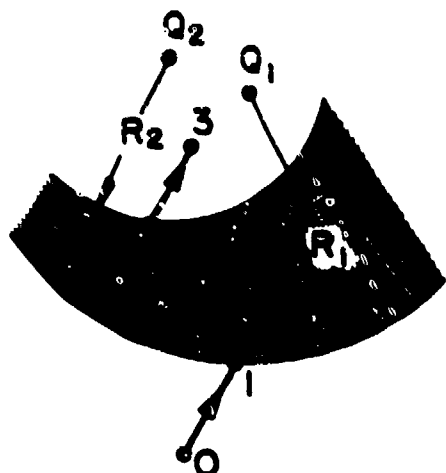


(b) $R_1 > 0, R_2 < 0$

x-z PLANE



(c) $R_1 < 0, R_2 > 0$



(d) $R_1 < 0, R_2 < 0$

Figure 22. General configurations where the field solution (2.3) can be used. Points (0.1.2.3) must be coplanar.

Condition (i) is necessary in order for the scalar transmission coefficients T_{\perp} and T_{\parallel} in (5.4) to be valid. When the four points $(0,1,2,3)$ are not coplanar, the perpendicular and parallel polarizations are no longer uncoupled. Then the scalar T_{\perp} or T_{\parallel} in (5.3) must be replaced by a (2×2) matrix. Also, (5.7) becomes more complicated.

For the general configurations in Figure 22, the ray tracing formulas in (5.2) are not valid. However, by following Snell's law, the ray tracing, even in the most general situation, is conceptually simple. Thus, instead of working out a set of general formulas, we leave it to the individual problems.

D. Axial Incidence on Symmetrical Shells

To study the features of the present ray solution, let us concentrate on a special case, where the four points $(0_1, 0_2, 0, 3)$ are on a straight line (Figure 23). Then the four curvatures in (5.7) reduce to

$$\kappa_{11} = \kappa_{12} = \frac{1}{na} + \frac{n-1}{n R_1} \quad (5.9a)$$

$$\kappa_{22} = \kappa_{21} = \frac{nR_1 + an(n-1)}{bR_1 + ab(n-1) + na R_1} + \frac{1-n}{R_2} = \frac{n}{b + \kappa_{11}^{-1}} + \frac{1-n}{R_2} \quad (5.9b)$$

An interesting question is when does κ_{11} or κ_{22} become negative (meaning a convergent pencil)? This is answered below:

(i) Negative κ_{11} . The transmitted pencil inside the dielectric shell is a convergent one when $\kappa_{11} < 0$ or

$$a > \left(\frac{1}{1-n} R_1 \right) > 0 \quad (5.10)$$

If $R_1 > 0$ (concave dielectric interface shown in Figure 24a), this is possible if $n < 1$. If $R_1 < 0$ (convex dielectric interface shown in Figure 24b),

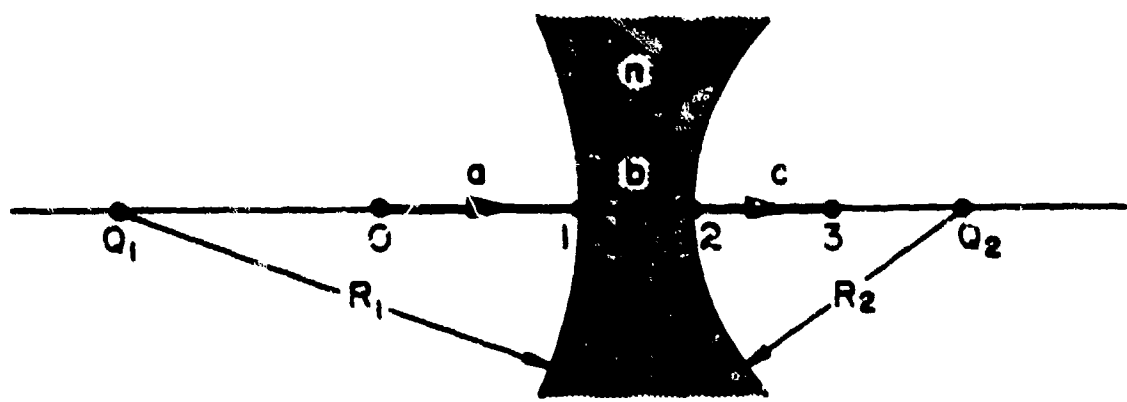
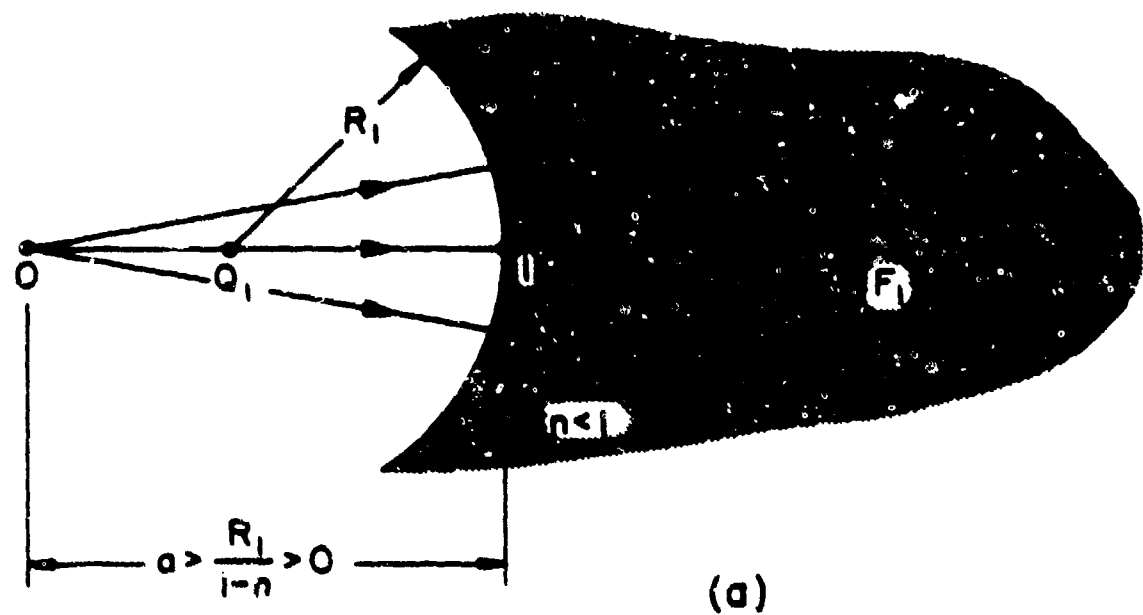
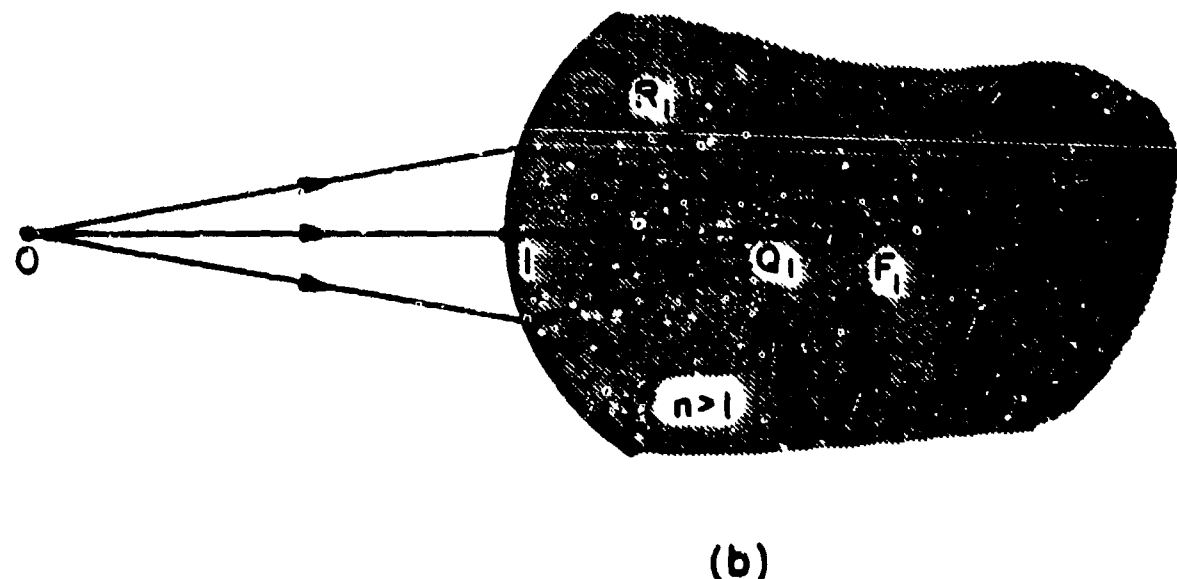


Figure 23. Axial incidence on a symmetrical shell. In this example, $R_1 > 0$ (concave) and $R_2 < 0$ (convex).



(a)



(b)

Figure 24. Condition for a convergent beam inside the dielectric shell.

this is possible only if $n > 1$. The distance between point 1 and focal point F_1 is $(\kappa_{11})^{-1}$.

(ii) Negative κ_{22} . The transmitted field in the free-space region outside the dielectric shell is convergent when $\kappa_{22} < 0$. Let us concentrate on a special case in which the thickness of the dielectric shell is small so that

$$b \ll \kappa_{11}^{-1} . \quad (5.11)$$

Then κ_{22} in (5.9b) becomes approximately

$$\kappa_{22} \approx \frac{1}{a} + (n - 1) \left(\frac{1}{R_1} - \frac{1}{R_2} \right) . \quad (5.12)$$

which is the well-known equation for the thin lens. (See for example Eq. (41-1), p. 685 of [11]. Note the corresponding notations used in [11] and here: $s = -a$, $s' = -\kappa_{22}^{-1}$, $R_1 = -R_1$, and $R_2 = -R_2$.) The condition for a negative κ_{22} under the approximation in (5.11) is

$$a > \frac{R_1 R_2}{(n - 1)(R_1 - R_2)} > 0 . \quad (5.13)$$

(iii) Far Field: If the observation point 3 is in the far zone ($\kappa_{22}c \gg 1$), then DF in (5.6) becomes

$$DF \approx \left\{ \frac{a}{a + \frac{1}{n}b + c} \right\} \left\{ 1 + (n - 1) \frac{ab}{R_1 R_2} \left[\frac{R_2 - R_1}{b} - 1 + \frac{1}{n} \left(1 - \frac{R_1}{a} \right) \right] \right\}^{-1} \quad (5.14)$$

The first factor in () in (5.14) is the divergence factor of a planar dielectric slab ($R_1, R_2 \rightarrow \infty$). Thus, the ratio of the electric field at a far-field point 3 for a spherical shell and that for a dielectric slab is

$$\eta = \frac{|\vec{E}(3) \text{ for spherical shell}|}{|\vec{E}(3) \text{ for a slab of same thickness}|}$$

$$= \left\{ 1 + (n - 1) \frac{ab}{R_1 R_2} \left[\frac{R_2 - R_1}{b} - 1 + \frac{1}{n} \left(1 - \frac{K_1}{a} \right) \right] \right\}^{-1} \quad (5.15)$$

As a numerical example, consider the case in which the inner and outer dielectric surfaces are concave and concentric ($Q_1 = Q_2$) with $(R_1/b) = 2$. We plot η as a function of (a/b) for $n = 0.5$ and $n = 3$ in Figure 25. We note that η can be substantially different from unity. When $a = R_1$, we have $\eta = 1$. Thus, in this interesting special case, the axial far field through a concentric spherical shell and that through a planar slab become the same. Another interesting special case occurs when $DF \rightarrow \infty$. It means that the paraxial rays emerging from the dielectric shell (Figure 23) are parallel to the axis so that they focus at the far-field point at infinity. From (5.14), it is shown that $DF \rightarrow \infty$ if $K_{22} \approx 0$ or

$$\frac{1}{a} = (n - 1) \frac{R_1 - R_2 + b(n - 1)/n}{R_1[R_2 - b(n - 1)/n]} \quad (5.16)$$

Under the thin-lens approximation $b \ll 0$, (5.16) is reduced to the well-known lensmaker's equation (see Eq. (41-2), p. 685 of [11]). In the antenna radome application, (5.16) is useful in the determination of the enhancement of the antenna main beam.

(iv) Multiple Refraction: For a given source point 0 and observation point 3 in Figure 21 or 22, we can trace two types of geometrical optics rays. The first type is the direct ray from 0 to 3 without going through internal reflections in the dielectric shell. Its field solution is given in (5.3) which, of course, is the main contribution. The second type contains rays which bounce one or more times inside the shell before reaching point 3. We now consider the contribution of such multiply refracted rays. For the

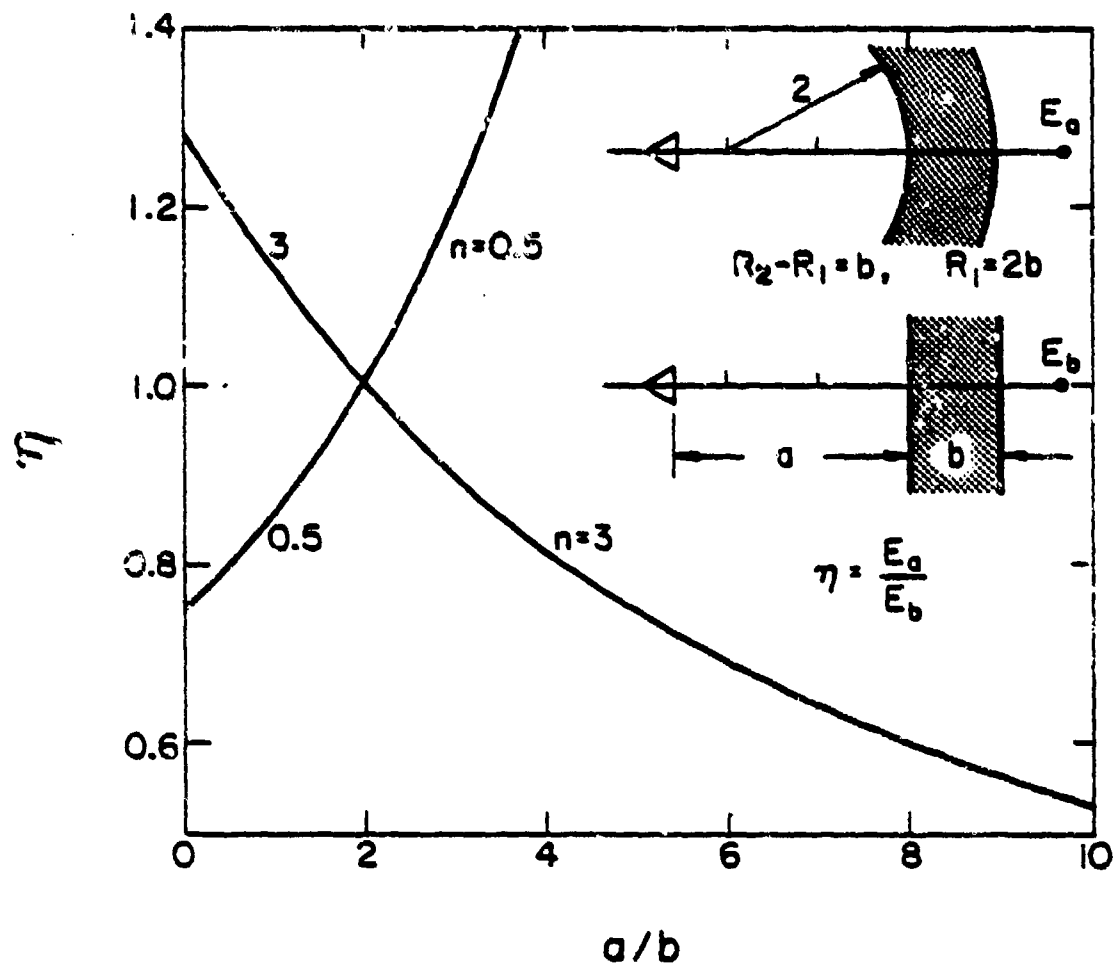


Figure 25. Transmitted field E_a transmitted through a spherical shell normalized by E_b which is that through a dielectric slab.

axial incidence case (Figure 23), let us further specialize the geometry by setting $(R_1, R_2) \rightarrow \infty$. The dielectric shell becomes the slab shown in Figure 26, and the field on the direct ray calculated from (5.3) reads

$$\hat{E}^t(3) = \hat{E}^t(1) e^{-jk_0(nb+nc)} \left[\frac{a}{na + b + nc} \right] T \quad (5.17)$$

where T is the product of the transmission coefficients at points 1 and 2 (Figure 26a)

$$T = T_1 T_2 = \left[\frac{2}{1+n} \right] \left[\frac{2}{1+(1/n)} \right] \quad (5.18)$$

In a similar manner, we can calculate the field on the multiply refracted rays (a twice internally refracted ray is shown in Figure 26b). Superimposing their contributions, we obtain the solution for the field at point 3 including the direct and all multiply refracted rays, namely,

$$[\hat{E}^t(3)]_{\text{all rays}} = \hat{E}^t(1) e^{-jk_0(nb+nc)} \left[\frac{na}{na + b + nc} \right] T \cdot \left\{ 1 + \sum_{p=1}^{\infty} e^{-j2pk_0 nb} \left(\frac{n-1}{n+1} \right)^{2p} \frac{na + b + nc}{na + (2p+1)b + nc} \right\}. \quad (5.19)$$

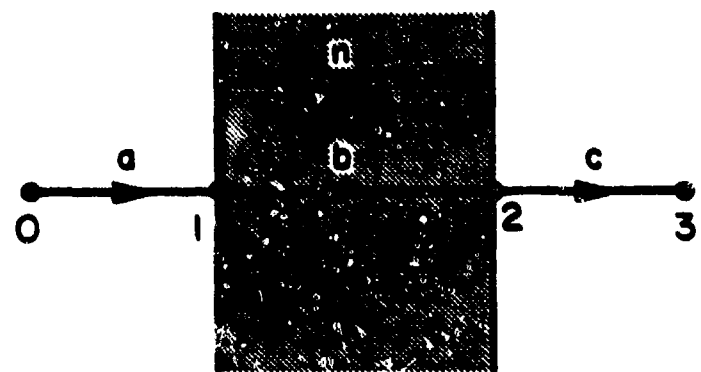
Under the condition

$$(a + c) \rightarrow \infty \text{ (far field), or } b \rightarrow 0 \text{ (thin slab)} \quad (5.20a)$$

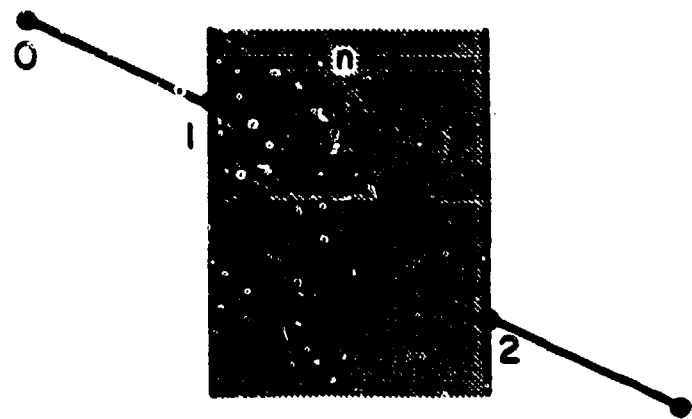
the series in (5.19) can be summed up in a closed form with the result

$$[\hat{E}^t(3)]_{\text{all rays}} = \hat{E}^t(1) e^{-jk_0(nb+nc)} \left[\frac{na}{na + b + nc} \right] T_{\text{slab}} \quad (5.20b)$$

when T_{slab} is recognized as the transmission coefficient of the slab



(a)



(b)

Figure 26. Singly and doubly refracted rays through a dielectric slab.

$$T_{\text{slab}} = \frac{T}{1 - \left[\frac{n-1}{n+1} \right]^2 \exp(-j2k_0 nb)} \quad (5.20a)$$

Comparing (5.20b) with (5.17), we note the effect of the multiply refracted rays is accounted for by replacing T by T_{slab} . When the condition in (5.20a) is not met, we must evaluate (5.19) numerically. Let us define an error term

$$\delta_p = \left\{ \frac{|\vec{E}^t(3)| \text{ including } p \text{ multiply refracted rays}}{|\vec{E}^t(3)| \text{ including all multiply refracted rays}} - 1 \right\} \times 100\% \quad (5.21)$$

In Figure 27, we plot δ_0 (including no multiply refracted rays) and δ_1 (including one multiply refracted ray) vs. u for $b = 0.75 \lambda_0$ and $(a+c)/b = 4$. Several observations are made. (a) For commonly used values of n (between 1 and 3), the error δ_0 is 13% or less except at resonances. A resonance occurs when all multiply refracted rays emerging from the slab are in phase with the primary ray. For the configuration in Figure 26, the resonance condition is

$$(nk_0 b/\pi) = (2nb/\lambda_0) = \text{a positive integer} \quad (5.22)$$

For an obliquely incident ray and/or a curved slab, the condition for resonance is rarely satisfied. Thus, generally speaking, the error for neglecting the multiple refraction is roughly 10%. (b) Errors δ_0 and δ_1 have about the same order of magnitude. Thus, the inclusion of the first-order multiply refracted ray does not in general improve the accuracy of the solution.

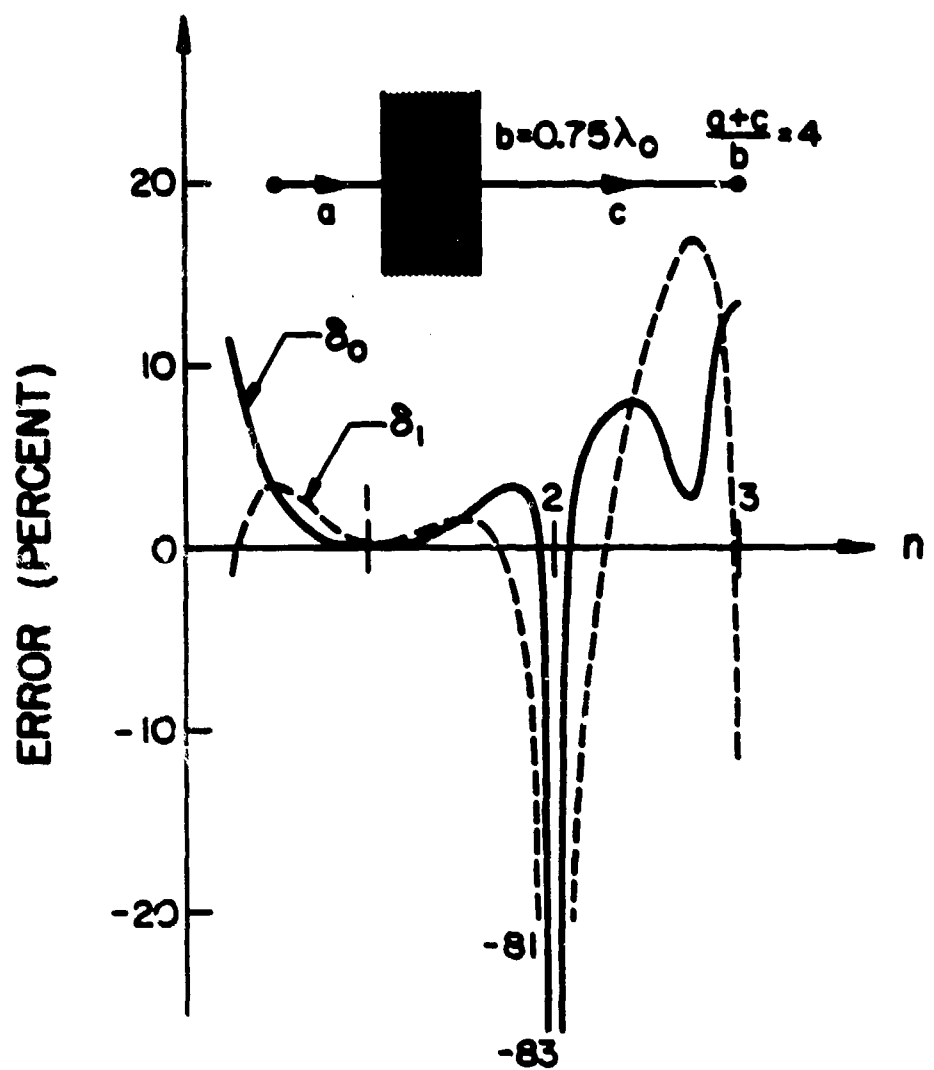


Figure 27. Error introduced by neglecting all or all except one multiply refracted ray in a dielectric slab.

E. Numerical Results

(a) Radome. Consider a dielectric spherical radome with an inner radius $20 \lambda_0$, a uniform thickness $0.5 \lambda_0$ and $n = \sqrt{5}$, as shown in Figure 28. The y-polarized source is located at points 1, 3, or 4, and its radiation field in the E-plane is given by

$$\hat{E}^i(r, \theta, \phi = \pi/2) = \frac{e^{-jk_0 r}}{r} [\hat{y} \cos(1.5 \theta)] . \quad (5.23)$$

The transmitted field is calculated from (5.3). For an observation point in the E-plane and in the far-field zone ($x = 0$ plane and $c \rightarrow \infty$ in Figure 21), we may rewrite (5.3) as

$$\hat{E}^t(r) = \frac{e^{-jk_0 r}}{r} [\hat{y} p^t(\theta)] , \quad r \rightarrow \infty \quad (5.24)$$

where r is the distance from point 0 to point 3 (Figure 21). We plot $p^t(\theta)$ as a function of θ in Figure 28. Generally speaking, the radome modifies the radiation field gently, as expected.

(b) Lens I (Double Concave). Unlike the above radome, a dielectric lens may modify the incident field drastically. Let us consider Lens I, drawn approximately to scale in Figure 29. The source is $2 \lambda_0$ away from the lens, and is y-polarized. Let us concentrate on the field in the H-plane ($x-z$ plane). In Figure 29, we launch 4 rays 2° apart. The outside ray (at $\theta = 6^\circ$) suffers total reflection at the second face of the lens, and is not transmitted into the free space region (we ignore multiple refractions). We assume the incident field from the source is confined to a cone (a beam). In the $x-z$ plane, it is given by

$$\hat{E}^i(x, 0, z) = \frac{e^{-jk_0 r}}{r} \begin{cases} \hat{y} 1 & , \text{ if } \theta < \theta^i \\ 0 & , \text{ if } \theta > \theta^i \end{cases} . \quad (5.25)$$

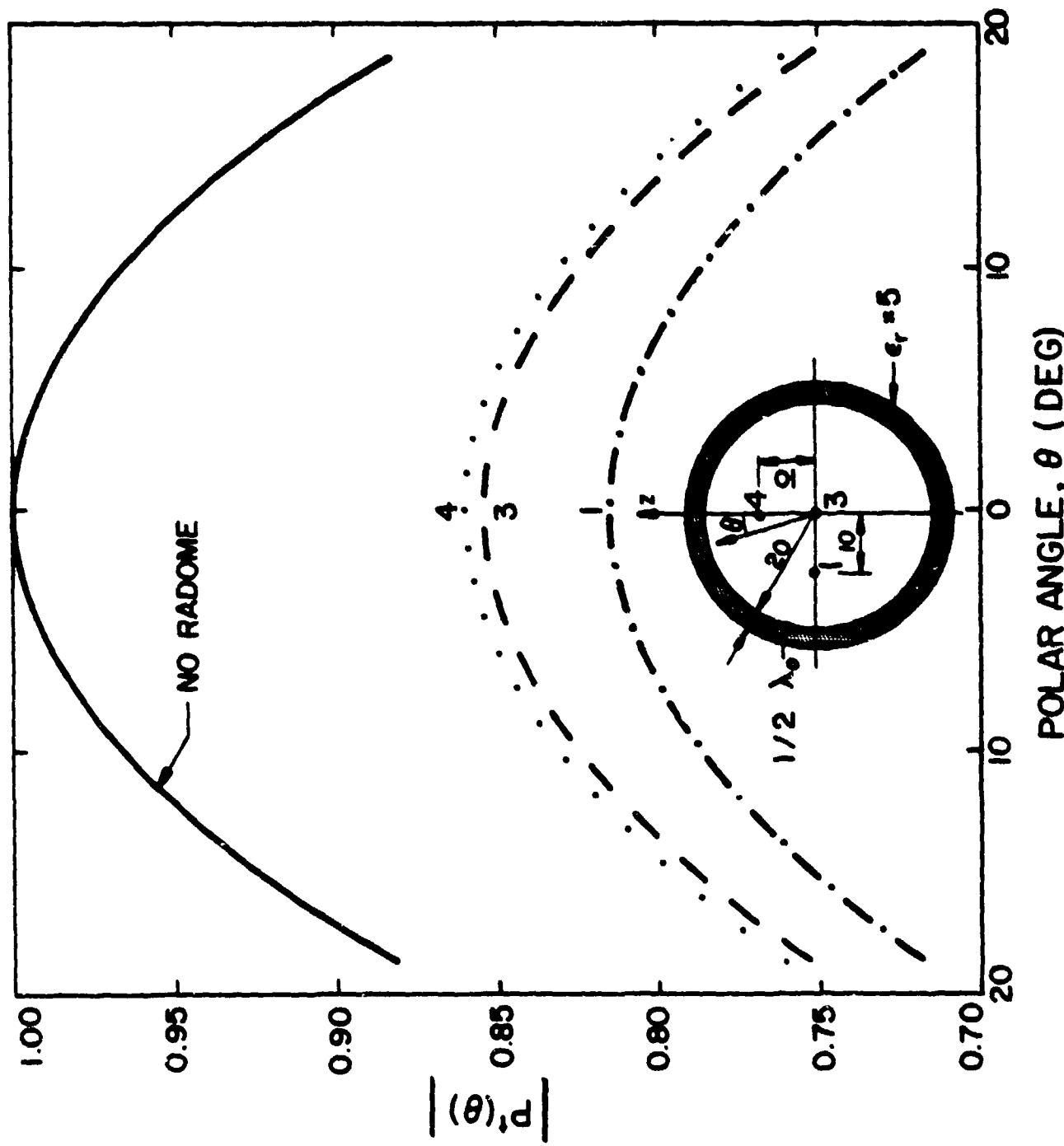


Figure 28. E-plane radiation pattern through a spherical radome.

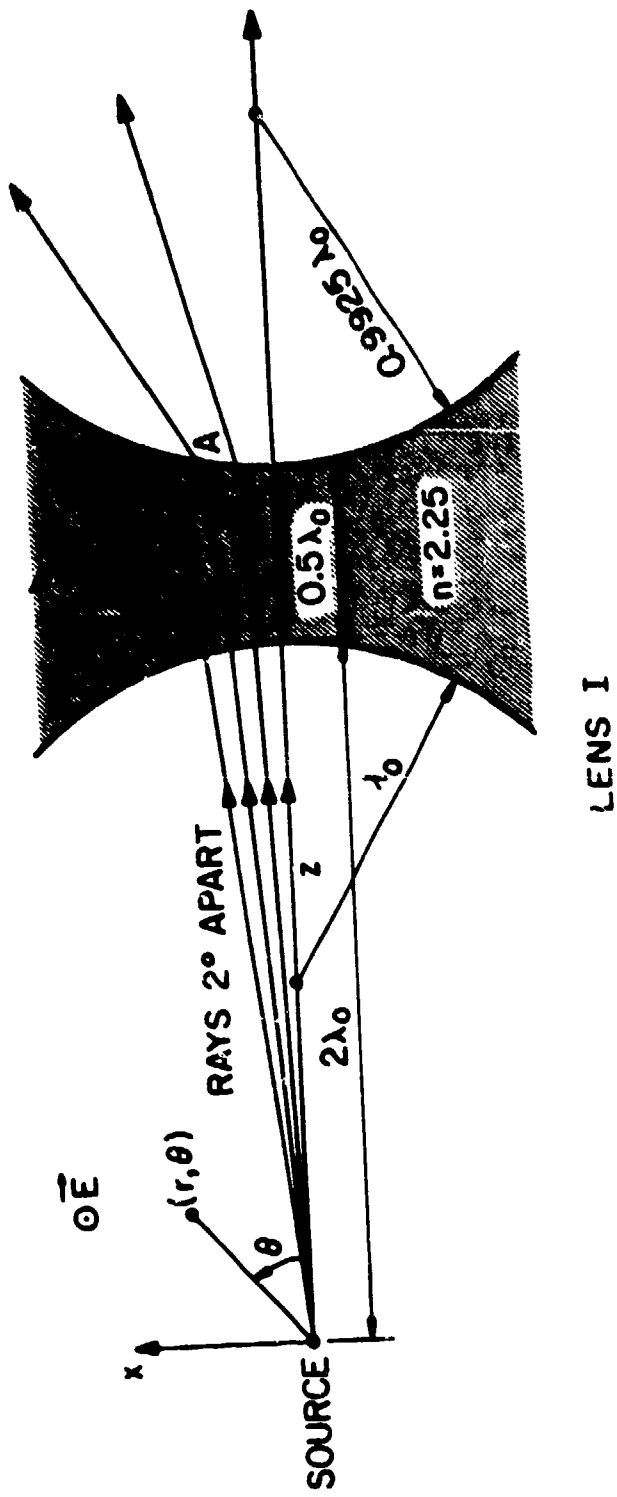


Figure 29. Double-concave spherical dielectric lens: geometry and ray picture.
Crosses indicate foci.

In the present case (Lens I), we choose $\theta^i = 5.5^\circ$. After transmission through the lens, the rays become more divergent, and they are spread over an angular region of about $\theta < 53.5^\circ$, which is considerably wider than the incident angular spread ($\theta < 5.5^\circ$). At an observation point $(r, \theta, \phi = 0)$, we express the transmitted field as

$$\hat{E}^t(r, \theta, 0) = \frac{-jk_0 r}{r} [y Q^t(r, \theta)] . \quad (5.26)$$

In the absence of the lens, $Q^t = 1$ for $\theta < \theta^i$ and $Q^t = 0$ for $\theta > \theta^i$. With the lens present, we plot $Q^t(r, \theta)$ as a function of θ for $r = 2 \times 10^3 \lambda_0$ in Figure 30. Note that the transmitted field is much weaker (12% or less) than the incident field because of the wider spread of the transmitted rays. For the present case, $Q^t(r, \theta)$ is only very weakly dependent on r , as long as $r > 100 \lambda_0$. Thus, the transmitted field \hat{E}^t in (5.26) in the far zone is approximately a spherical wave with an angular pattern Q^t . Every transmitted ray has two foci. Their distances behind the second face Σ_2 of the lens are $(\kappa_{21})^{-1}$ and $(\kappa_{22})^{-1}$, which may be calculated from (5.7). In particular, $(\kappa_{21})^{-1}$ is for the normal section of the wavefront in the plane of incidence (x - z plane), whereas $(\kappa_{22})^{-1}$ is for that in the perpendicular plane (defined by the y -axis and the ray direction). For the third ray (incident $\theta = 4^\circ$) in Figure 29, we calculate from (5.7) that

$$(\kappa_{21})^{-1} \approx +0.21 \lambda_0 , \quad (\kappa_{22})^{-1} \approx +0.375 \lambda_0 . \quad (5.27)$$

We mark the position of the focus corresponding to κ_{21} by a cross in Figure 29. The distance between A and the cross is $(\kappa_{21})^{-1}$. The trace of the two sets of foci is shown in Figure 31. They are curves on the two caustic surfaces of the transmitted wavefront (intersection of caustic surfaces and the x - z plane).

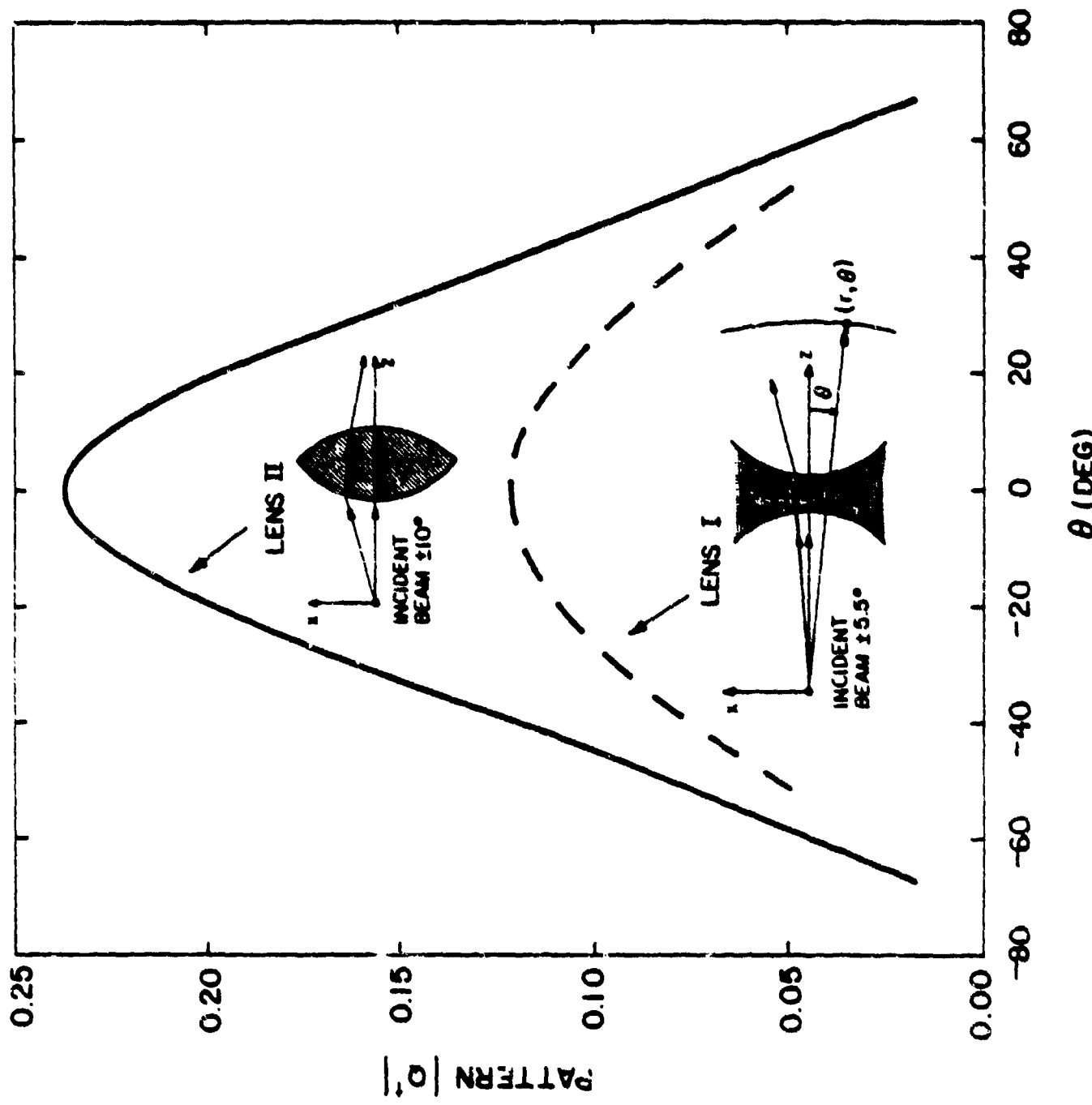


Figure 30. H-plane far field pattern through lens I and lens II.

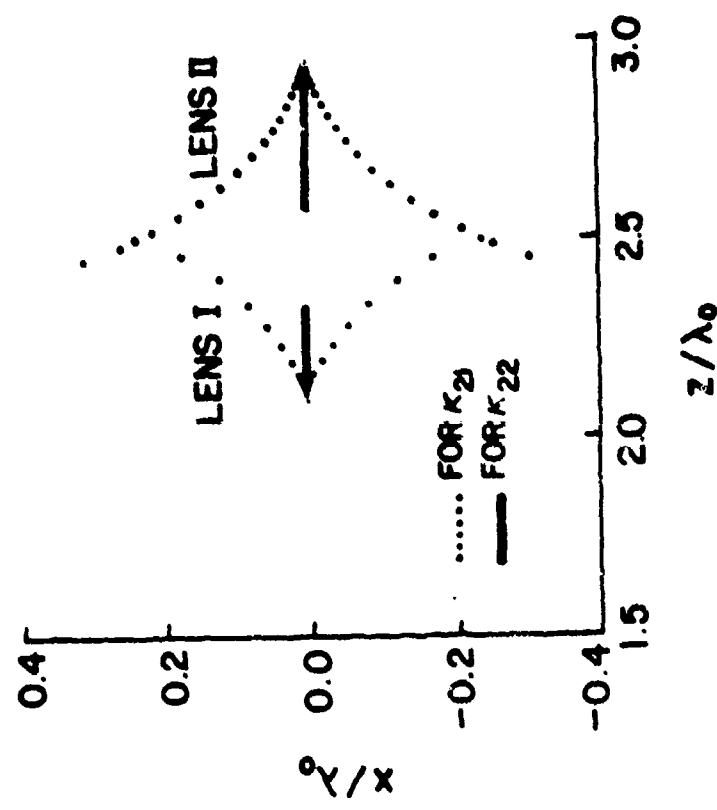


Figure 31. Trace of foci of the traced rays which lie in x-z plane for lenses I and II.
 (For better presentation, the scale along the x-axis is expanded.)

(c) Lens II (Double convex). The geometry of Lens II and its ray picture are shown in Figure 32. The incident field is given in (5.25) with $\theta^i = 10^\circ$. The transmitted field in the H-plane is expressed in (5.26), where $Q^t(r, \theta)$ is again very weakly dependent on r in the far zone and is plotted in Figure 30. We note that the incident 10° -beam is now spread into a 67° -beam after transmission through Lens II. The peak value of the transmitted field is about 24% of the incident field at the same far-field location. The caustic curves are shown in Figure 31.

(d) Lens III (Convexo-Concave). The geometry of Lens III is shown in Figure 33. The radii (R_1, R_2) of the lens and the source distance satisfy the lensmaker's equation in (5.16), so that the transmitted rays near the axial direction are almost parallel and focus at a point at infinity in the axial direction. The incident field is given in (5.25) with $\theta^i = 12^\circ$. The H-plane transmitted field E^t is expressed in (5.26), where $Q^t(r, \theta)$ varies drastically from the near field zone up to $r \sim 100 \lambda_0$ as seen from Figure 34. Beyond $r \sim 100 \lambda_0$, the beam becomes narrower, and the peak becomes higher with the increase of r . It is well-known that the exact value of the beam's peak (on a caustic surface) cannot be predicted by the present geometrical optics theory. It can be calculated from, for e.g., the Huygens-Green formula described in p. 107 of [15]. The caustic curves are shown in Figure 35.

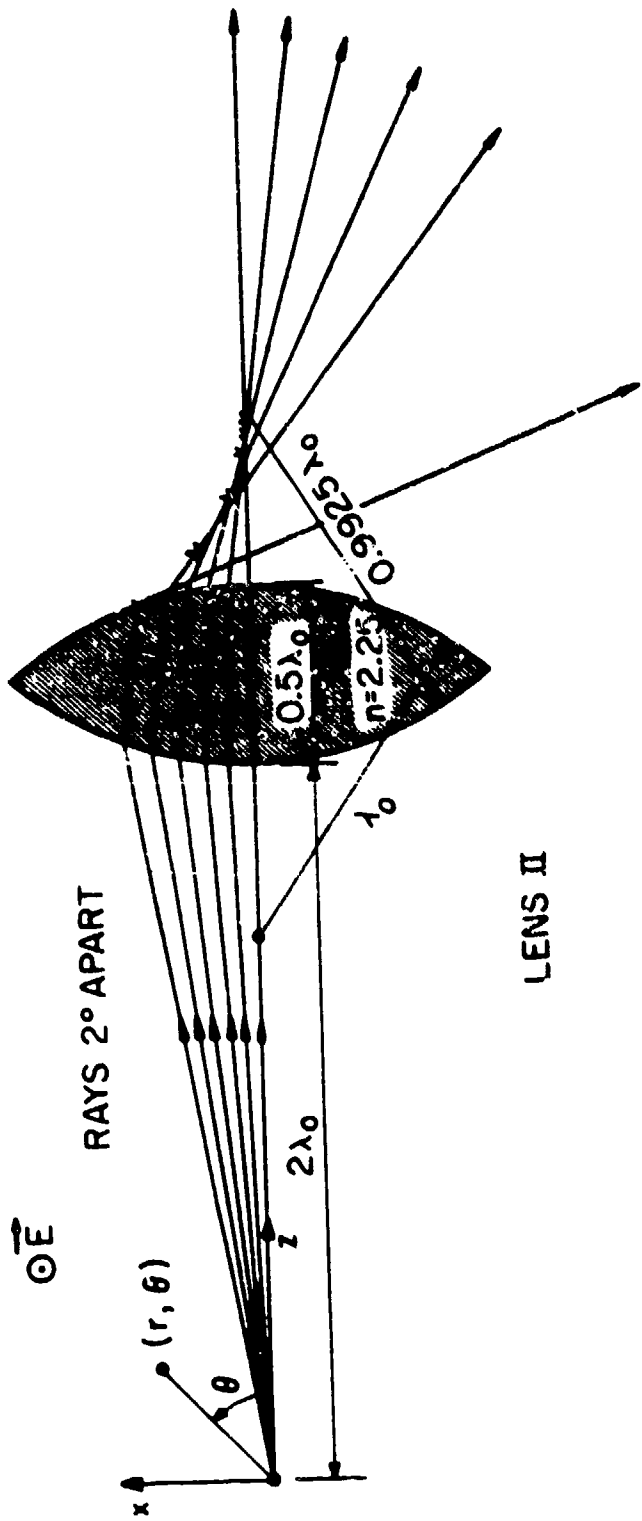


Figure 32. Double-convex spherical dielectric lens: geometry and ray picture. Crosses indicate foci.

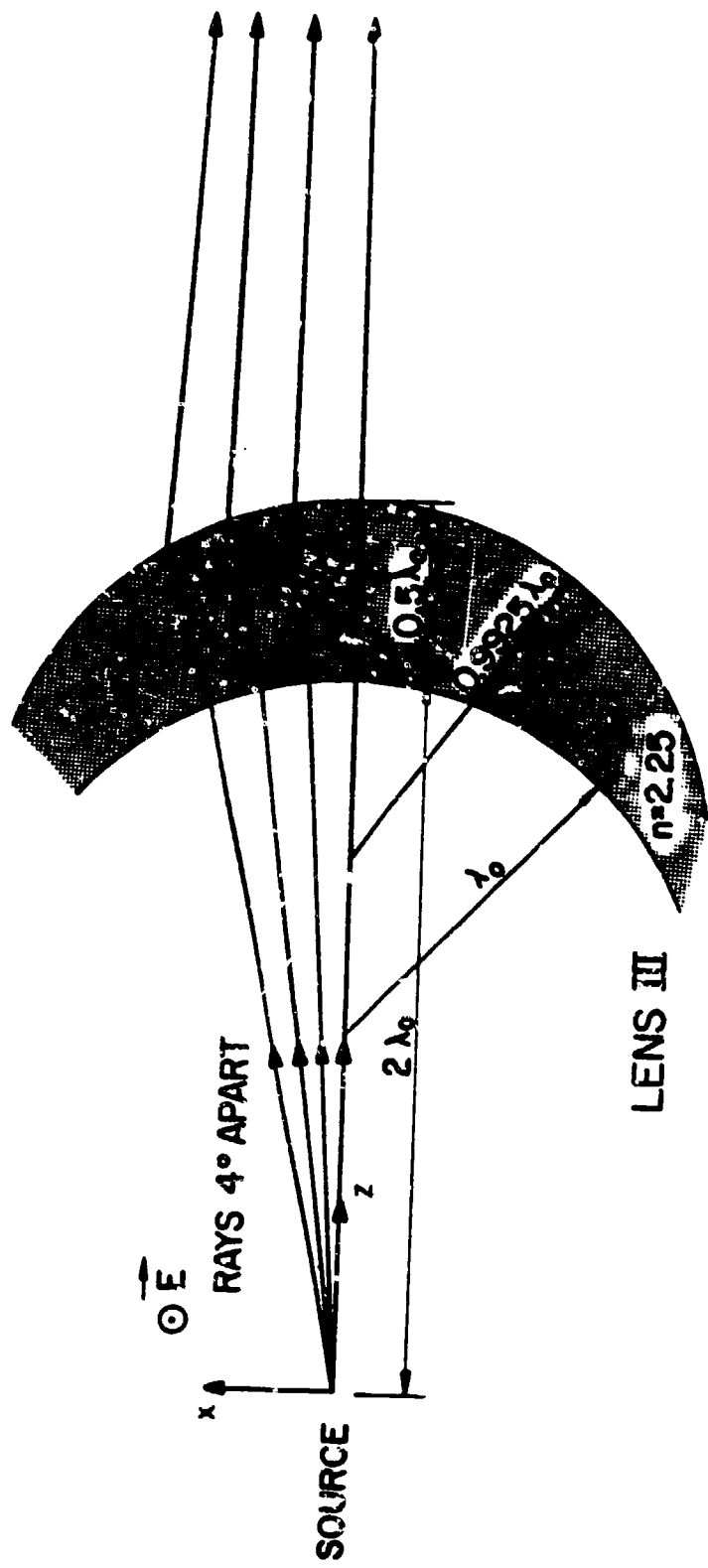


Figure 33. Convexo-concave spherical dielectric lens: geometry and ray picture.

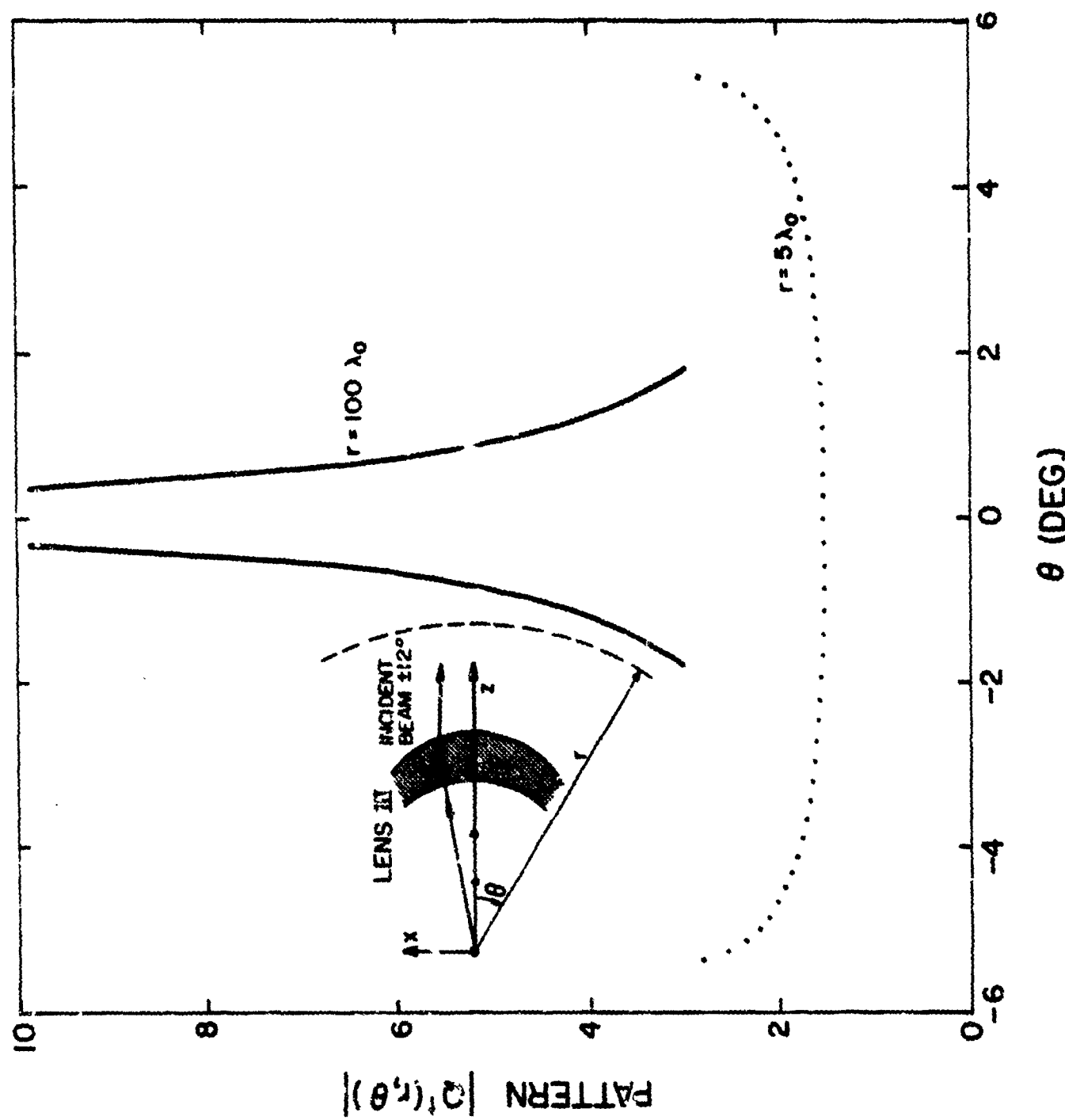


Figure 24. H- μ plane far field pattern through lens III.

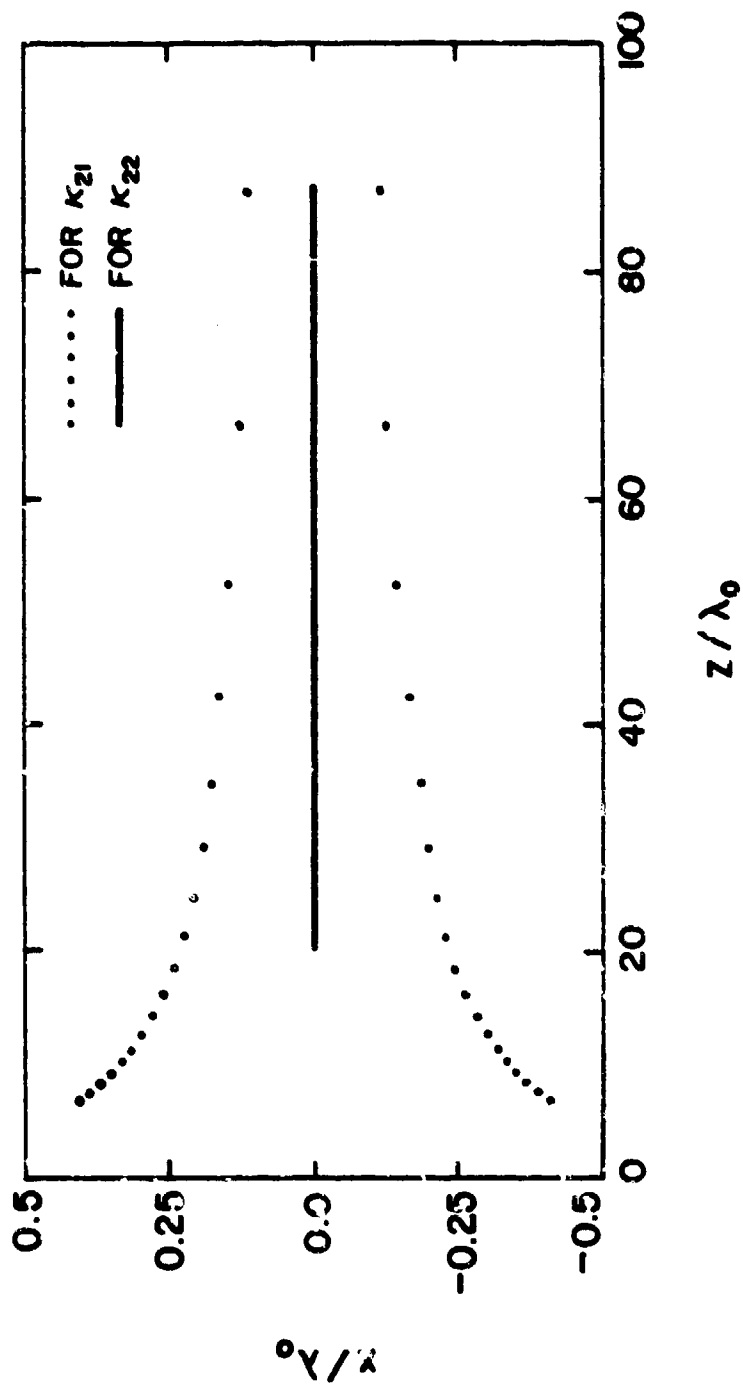


Figure 35. Trace of foci of the transmitted rays which lie in the x - z plane, for lens III.

F. Conclusions

For a given incident field in (5.1), a geometrical optics solution of the transmitted field through a spherical dielectric shell (Figure 22) is given in (5.3) through (5.7). The present solution is an approximated one. We summarize its validity and limitations below

- (i) Because ray techniques are being employed for the analysis presented herein, the radii of curvature should be large in terms of the incident wavelength in order for the results to be valid. As in all ray-optical solutions, our solution fails when the observation point is near the caustic surfaces of the transmitted wavefront.
- (ii) The solution given in (5.3) and (5.7) is valid only for spherical shells, and when four points (0,1,2,3,) in Figure 22 are coplanar. These two limitations can be relaxed. In fact, an explicit GO solution, (which is very similar to the present one,) for an arbitrarily curved shell, and arbitrary source and observation points is given in [5].
- (iii) Our solution includes only the contribution from the first-order refracted ray (a direct ray from the source to the observation point without internal refractions inside the dielectric shell). It has been estimated that, except at "resonances" which rarely occur for curved shells, the error of neglecting higher-order refracted rays is roughly 10% for $n = \sqrt{\epsilon_r}$ in the range 1 to 3. It should be pointed out that the higher-order refracted rays can be calculated in exactly the same manner as the first-order refracted

ray by using the formulas derived in this work and in [5].

It is only a matter of bookkeeping and computer time in doing the numerical calculations.

- (iv) For transmission through a curved dielectric shell, the major field contribution, of course, comes from the refracted rays which are studied in this paper. However other diffraction processes exist which may not be conveniently fitted into ray descriptions, and their contribution may be significant under certain conditions. An example is the modal fields guided by the curved dielectric shell. Efforts to understand its behavior in canonical problems have been initiated [16].

VI. ARRAY COVERED BY RADOME

In this chapter, we study the radiation pattern of a linear array of eleven point sources enclosed in a radome. The array elements are arranged symmetrically along the x-axis with a half-wavelength spacing as shown in Figure 36. The element pattern is assumed to be of the form

$$\hat{E}^i = \frac{e^{-jk_0 r}}{r} [\sin \phi \hat{\theta} + \cos \phi \hat{\phi}] \cos \theta . \quad (6.1)$$

To calculate the array pattern, rays are traced from each source through the radome as discussed in Chapter I. When the ray tracing is done, there are two options available in calculating the far field: (a) we can calculate the transmitted field \hat{E}_3^t over a planar surface Σ_3 just outside the radome and then integrate this field to get the far-field pattern; (b) we can push the surface Σ_3 to infinity and calculate \hat{E}_3^t on this surface directly, thus avoiding the integration step--this is known as the direct ray method. Though, in general, both methods do give identical results, the second method becomes less accurate if the far-field point happens to be in the vicinity of the caustic surfaces of the transmitted wavefront. However, one does not usually confront such a situation in practice. The details of the calculations using these two methods may be found in [5].

Once the far-field pattern of each source is obtained, the sum pattern is obtained by adding the patterns of the individual elements. A progressive phase shift is introduced among the elements to enable beam scanning. In the results to follow, we present the H-plane (x-z plane) sum patterns. Thus, restricting ourselves to this plane, the incident field in (6.1) reduces to

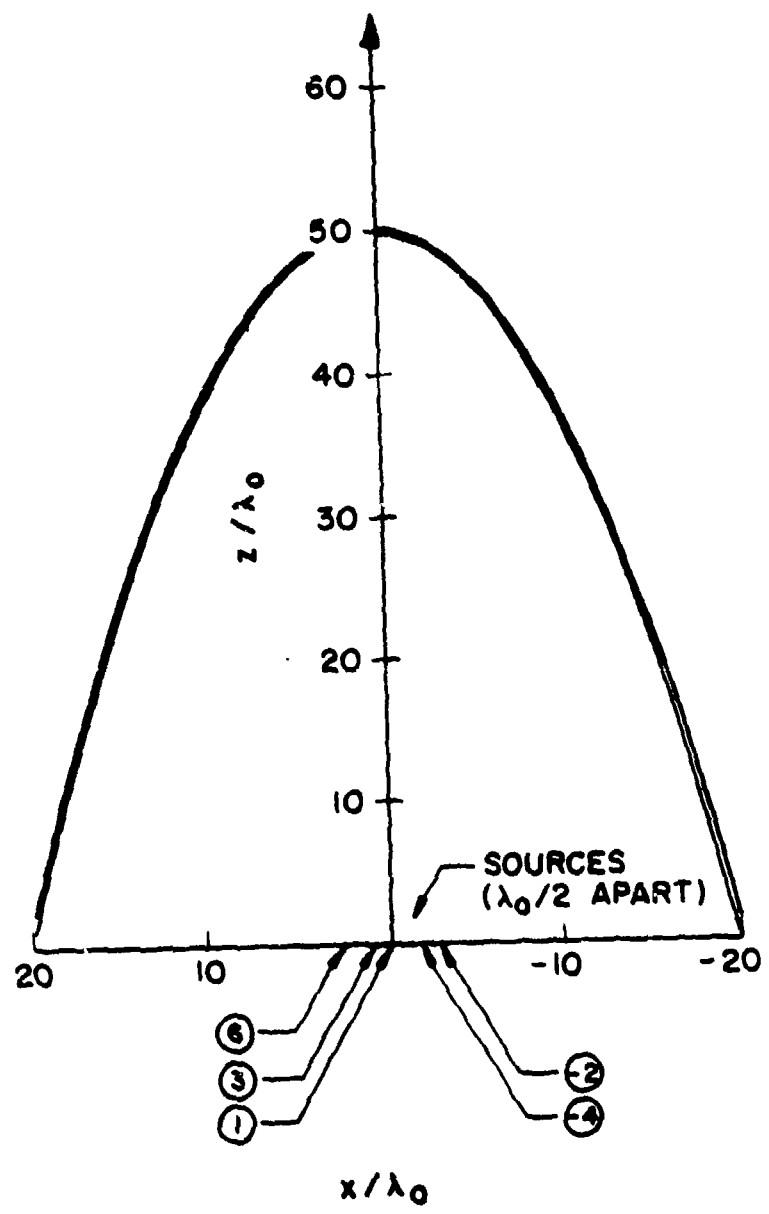


Figure 36. Paraboloidal radome A generated by Eqs. (6.4) and (6.5).

$$\hat{E}^t = \frac{y e^{-jk_0 r}}{r} \cos \theta \quad . \quad (6.2)$$

The total transmitted field, summed over all the sources, may then be represented by

$$E_{\text{sum}}^{(t)} = \frac{e^{-jk_0 r}}{r} \sum_{n=4}^{+6} |E_{(t)}^t|_n e^{j\phi_n^{(t)}(\theta)} e^{j(n-1)(kds \sin \theta + \alpha)} \quad (6.3)$$

where $|E_{(t)}^t|_n$ represents the magnitude and $\phi_n^{(t)}(\theta)$, the phase, of the transmitted field due to the n^{th} source, d in the element spacing, and α is the inter-element phase shift.

Array patterns were calculated for four types of radomes as specified in Table I. Two of the radomes were paraboloids and two were tangent ogives.

(a) Radome A: This is a paraboloidal radome of relative dielectric constant 2.5. The inner and outer surfaces of this radome were generated by

$$z/\lambda_0 = 50 - (x^2 + y^2)/(8\lambda_0^2) \quad (6.4)$$

and

$$z/\lambda_0 = 50.25 - (x^2 + y^2)/(8.16\lambda_0^2) \quad , \quad (6.5)$$

respectively. The geometry of this radome, along with the eleven element array, are shown in Figure 36. The H-plane element patterns through the radome are shown in Figure 37. The H-plane sum patterns are shown in Figures 38-42 for different scan angles (the scan angles indicated in the figures are the values for the beam without the radome, measured from the z-axis).

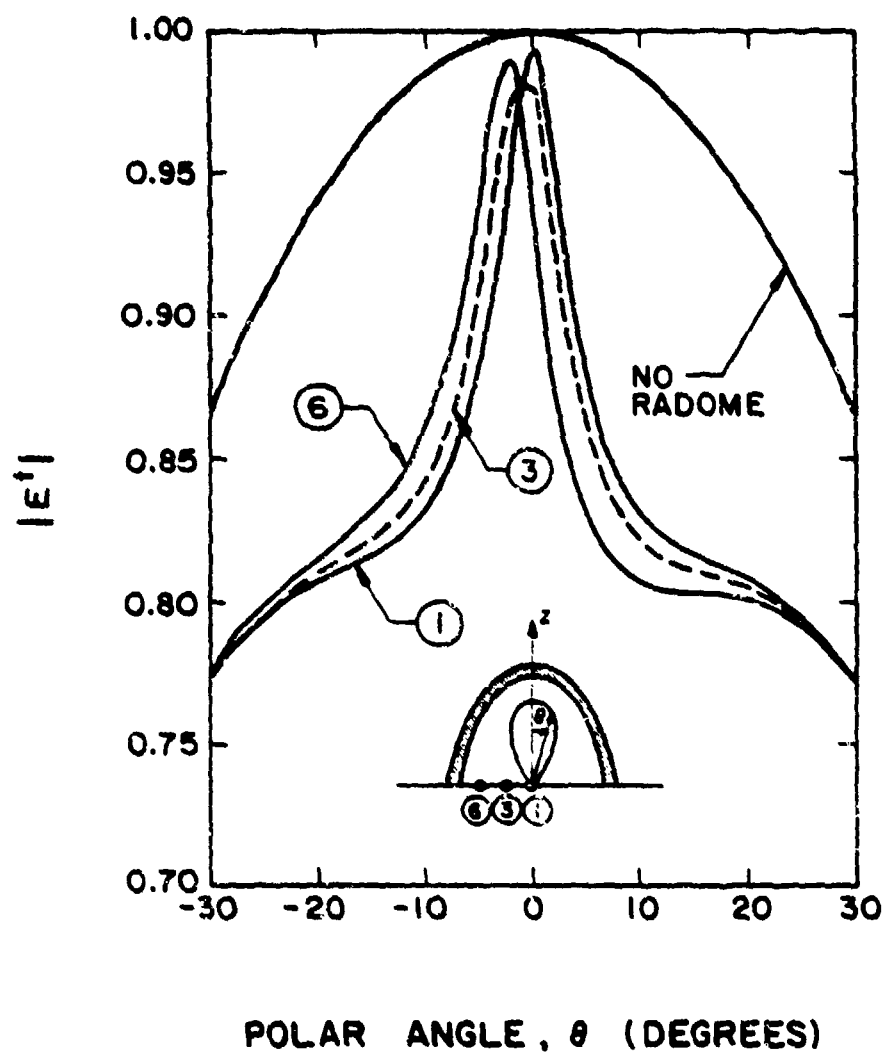


Figure 37. H-plane element patterns through radome A for sources ①, ③ and ⑥.

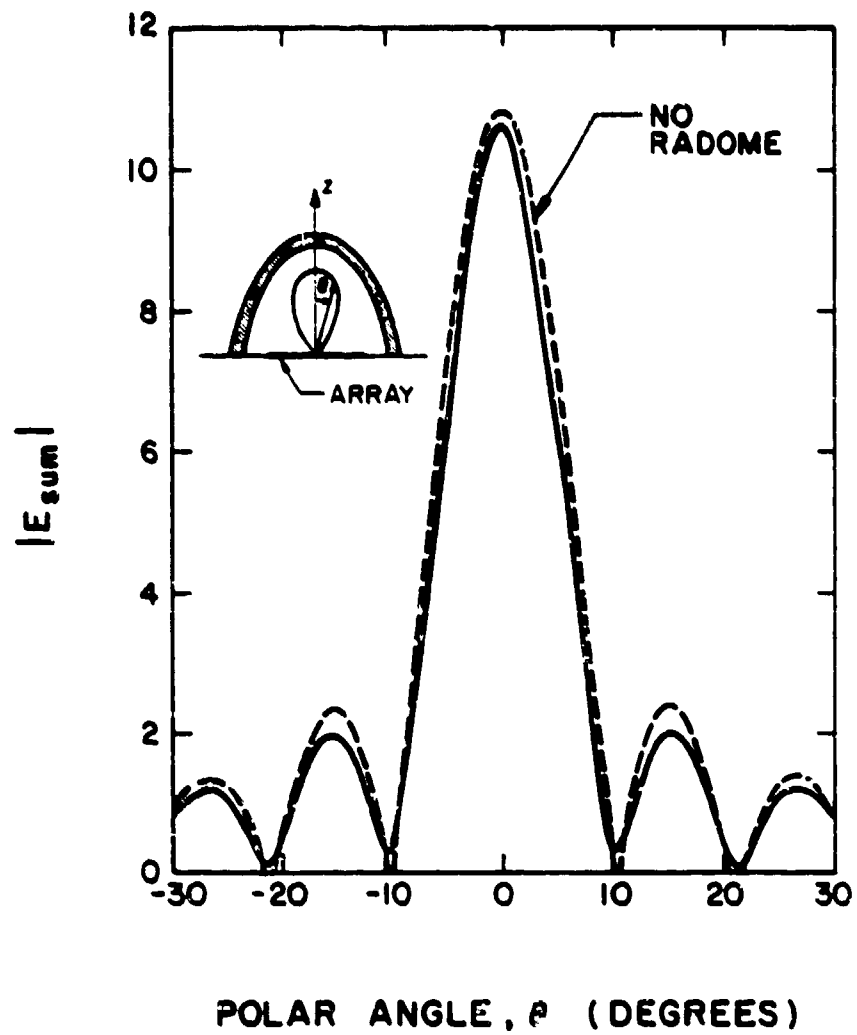


Figure 38. H-plane sum pattern through radome A beam at 0° .

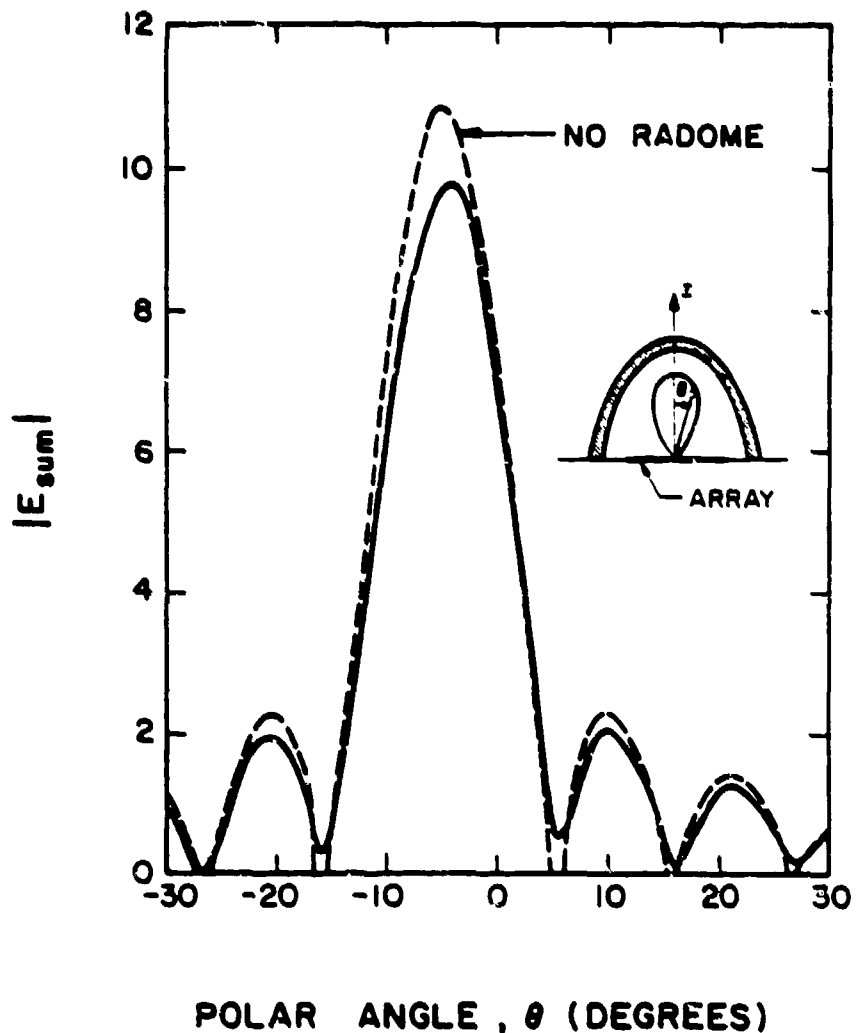


Figure 39. Same as Figure 38, except for scan angle = -4.95° .

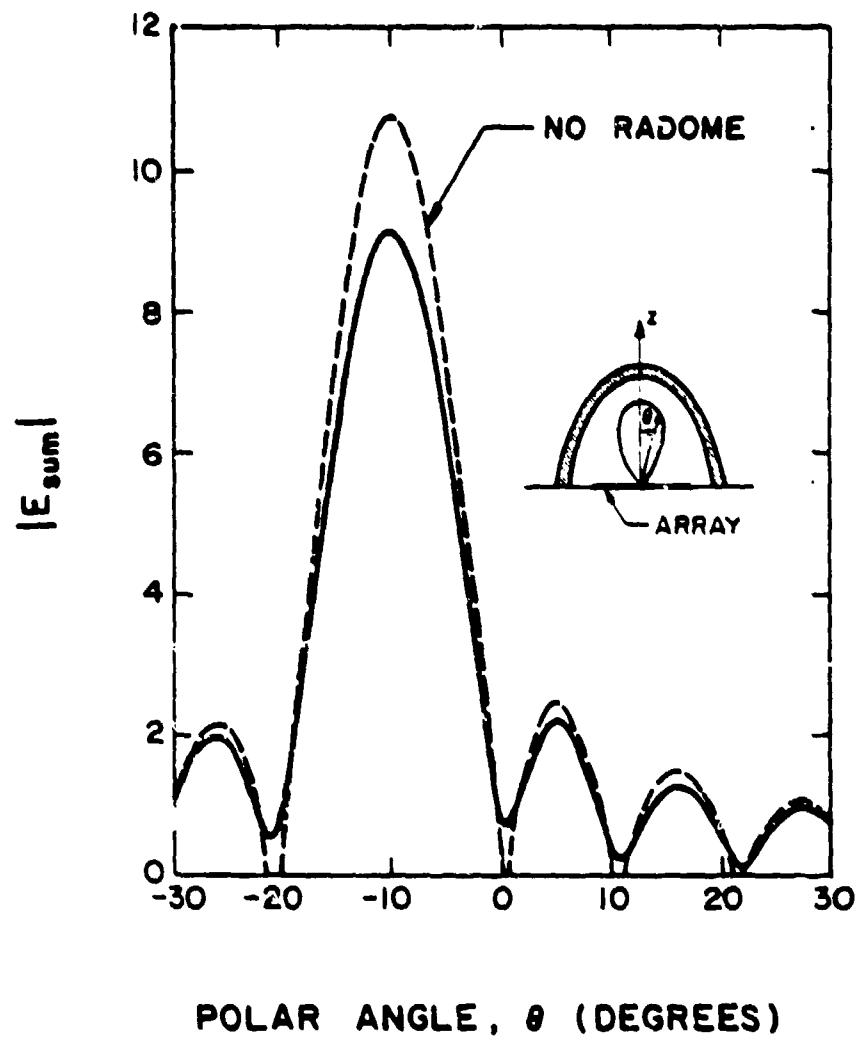
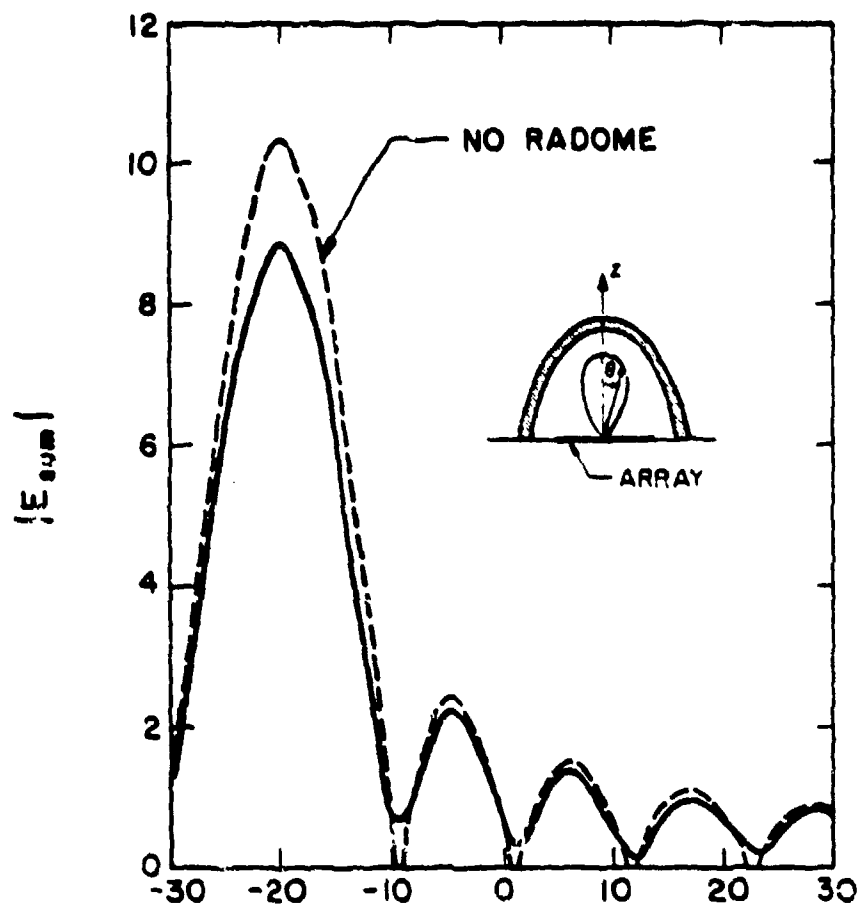


Figure 40. Same as Figure 38, except for scan angle = -9.89° .



POLAR ANGLE, θ (DEGREES)

Figure 41. Same as Figure 38, except for scan angle = -19.77° .

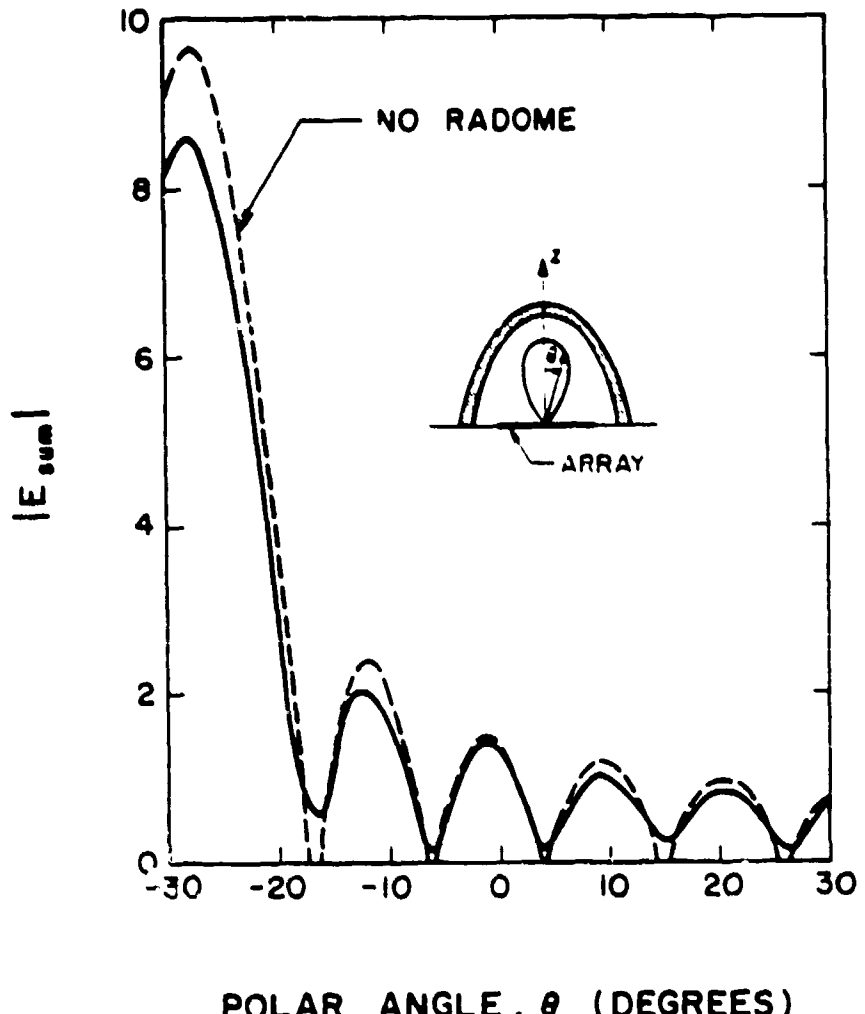


Figure 42. Same as Figure 38, except for scan angle = -27.64° .

TABLE I

RADOME	SHAPE	ϵ_r	LENGTH (External)	DIAMETER (External)	WALL THICKNESS
A	Paraboloid	2.5	50.25 λ_0^*	40.50 λ_0	$\lambda_0/4$
B			50.50 λ_0	40 λ_0	$\lambda_0/2.0$
C	Tangent Ogive	5.7	14.6 λ_0	6.7 λ_0	0.233 λ_0
D		9.3	14.9 λ_0	6.82 λ_0	0.176 λ_0

*Free-space wavelength

Figure 43 shows the radome boresight error for this radome. The boresight error is the difference between the beam maximum with and without the radome [(beam maximum with radome) - (beam maximum without radome)].

It may also be observed from Figures 38-42 that, as the scan angle increases, the gain decreases because of the decrease in the effective aperture with increasing scan angle. Figure 44 shows this gain variation. Observe that in the presence of the radome the maximum field strength drops much faster. Also, around the tip region where the curvature is the highest, the maximum field strength decreases faster, and then levels off at higher scan angles.

(b) Radome B: This is also a paraboloidal radome of $\epsilon_r = 2.5$, but the outer surface in this radome was configured so as to make the curvature in the tip region very close to the critical curvature (see Figure 30, [5]), thus resulting in a greater focussing action in the z-direction. The inner surface was obtained from (6.4) and the outer surface was obtained from

$$z/\lambda_0 = 50.50 - (x^2 + y^2)/(7.925\lambda_0^2) . \quad (6.6)$$

The geometry of the radome is shown in Figure 45. Observe that the thickness is maximum along the z-axis and reduces gradually to zero thickness at the base.

The H-plane sum patterns are shown in Figures 46-49, and the boresight error curve is presented in Figure 50. The focussing action of this radome may be clearly observed in Figure 46 - the axial field strength is 1.4 times as large as that without the radome.

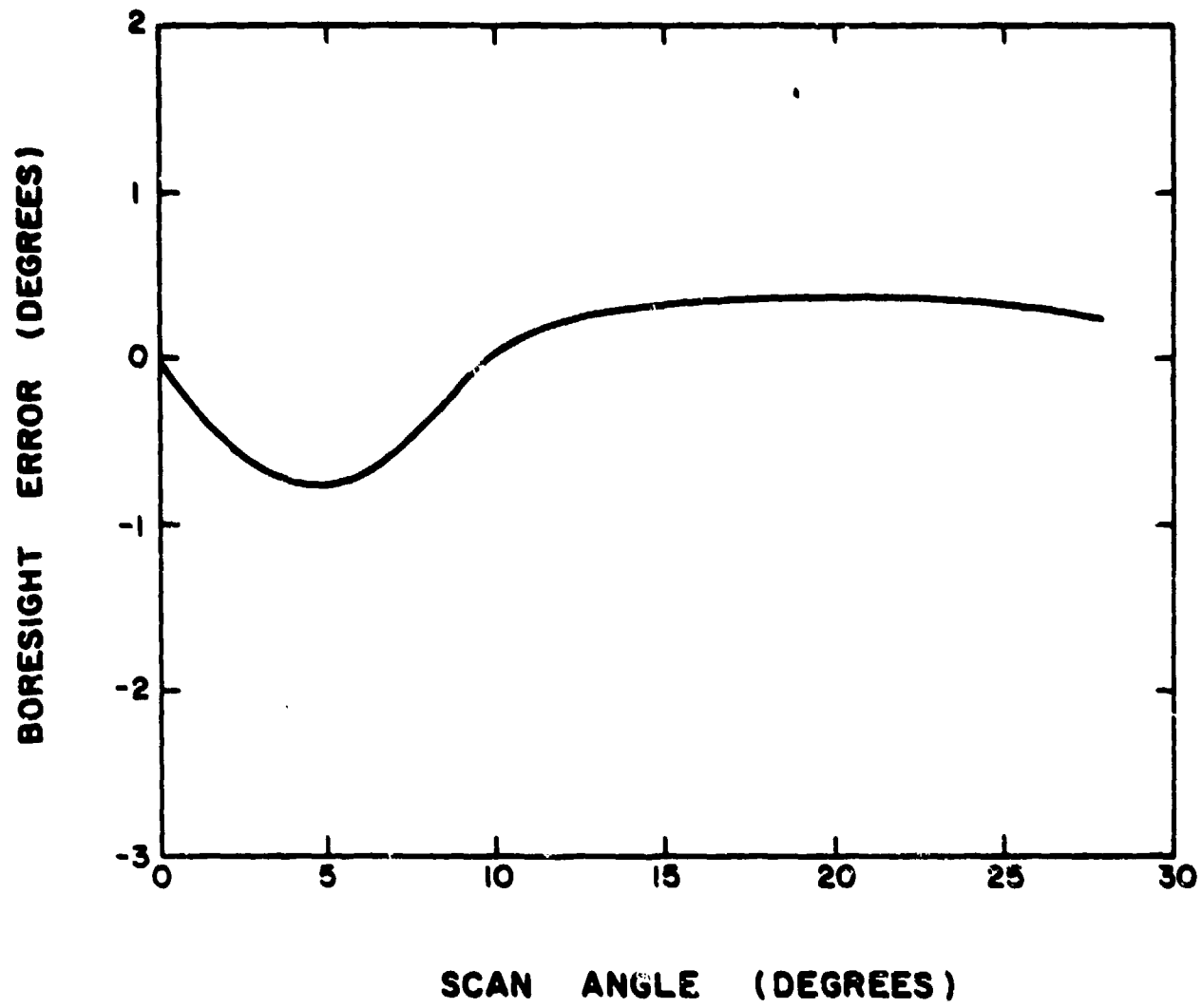


Figure 43. Boresight error for radome A.

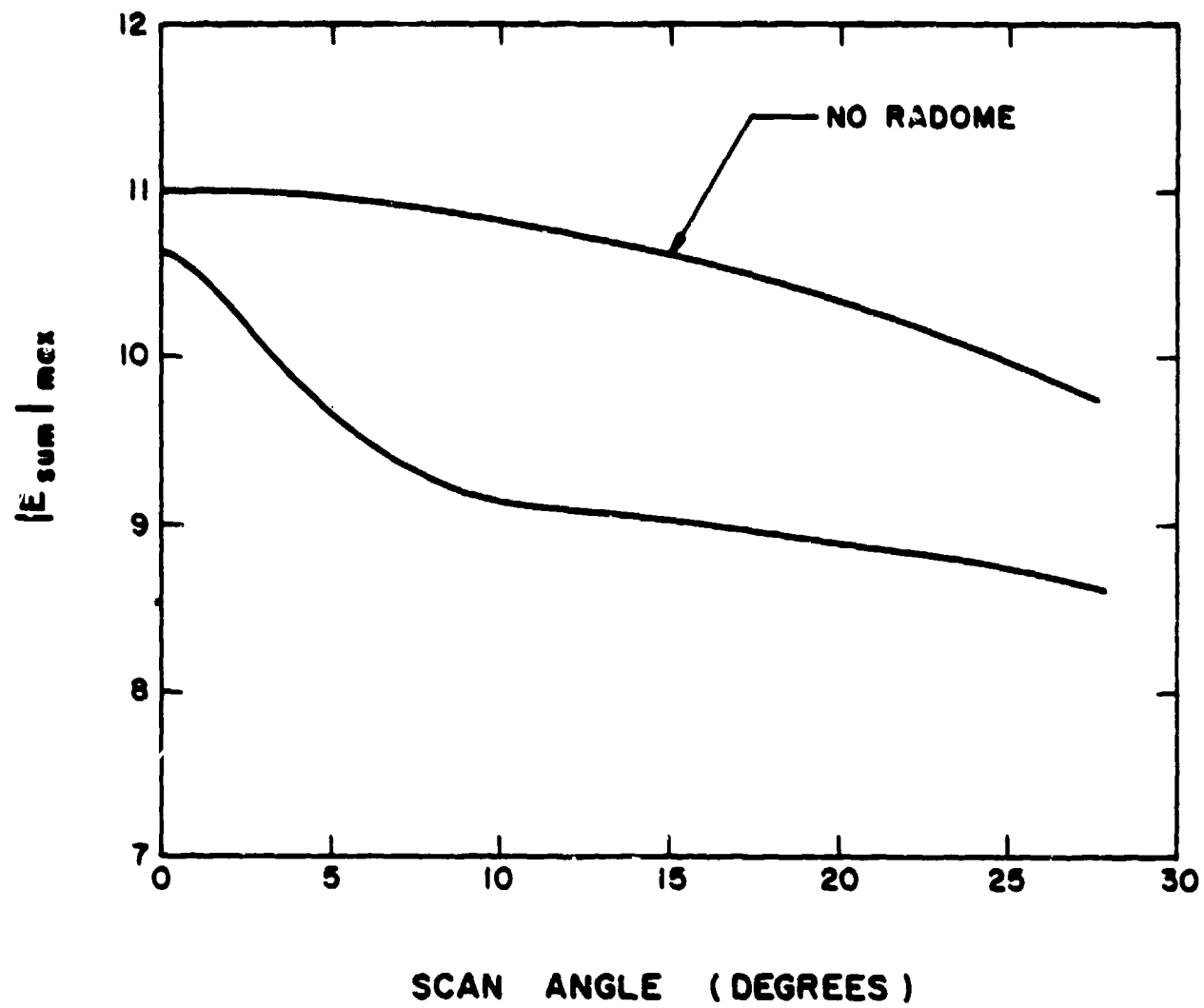


Figure 44. Variation of maximum field strength with scan angle for radome A.

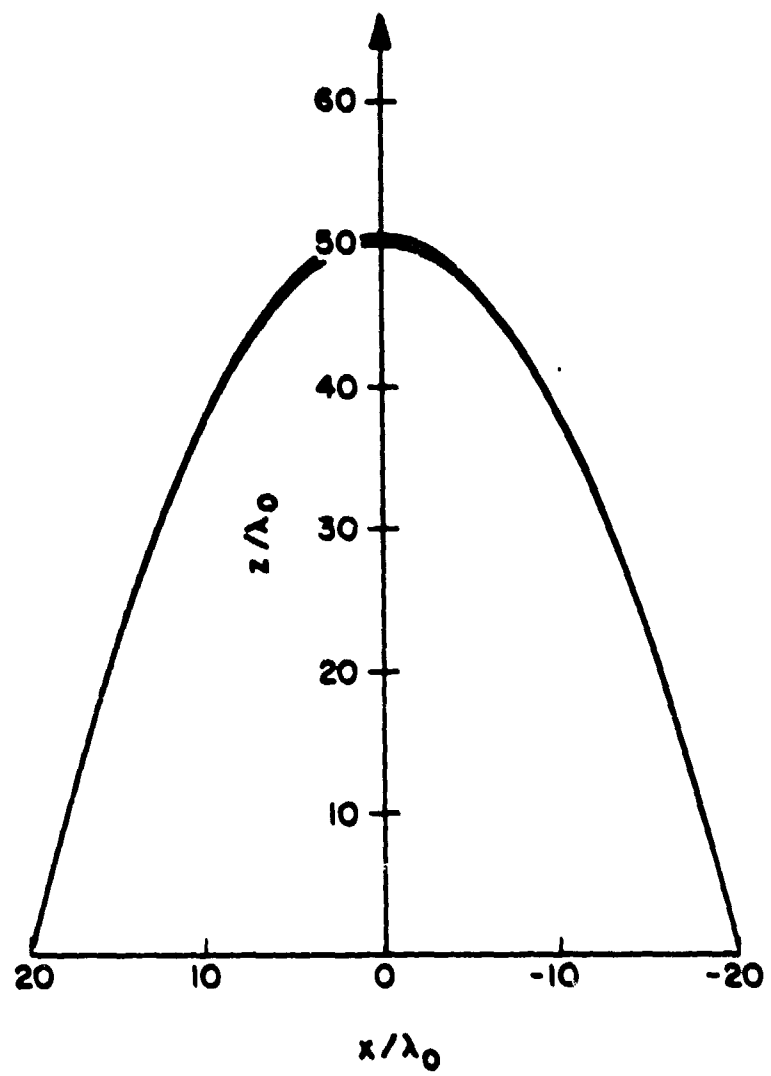


Figure 45. Geometry of radome B.

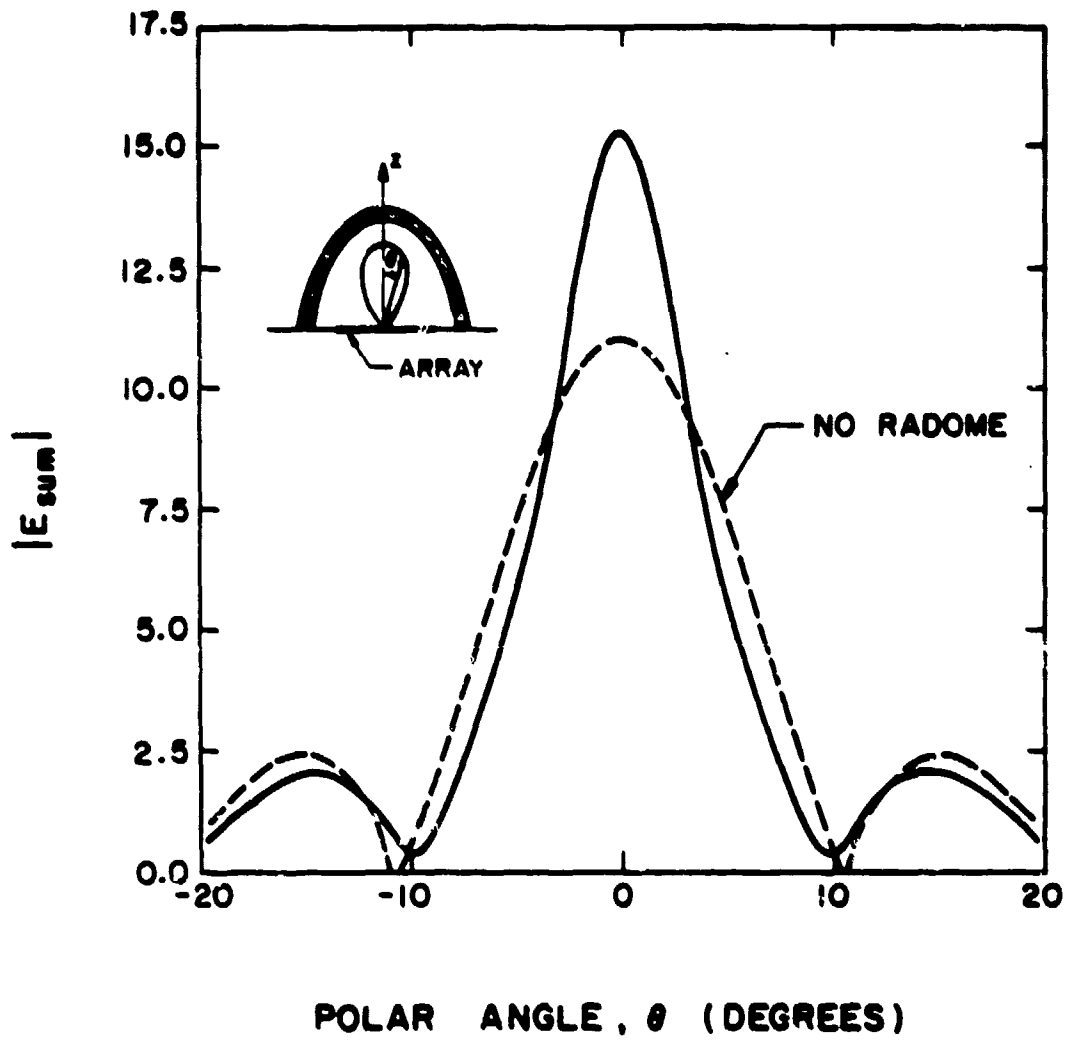
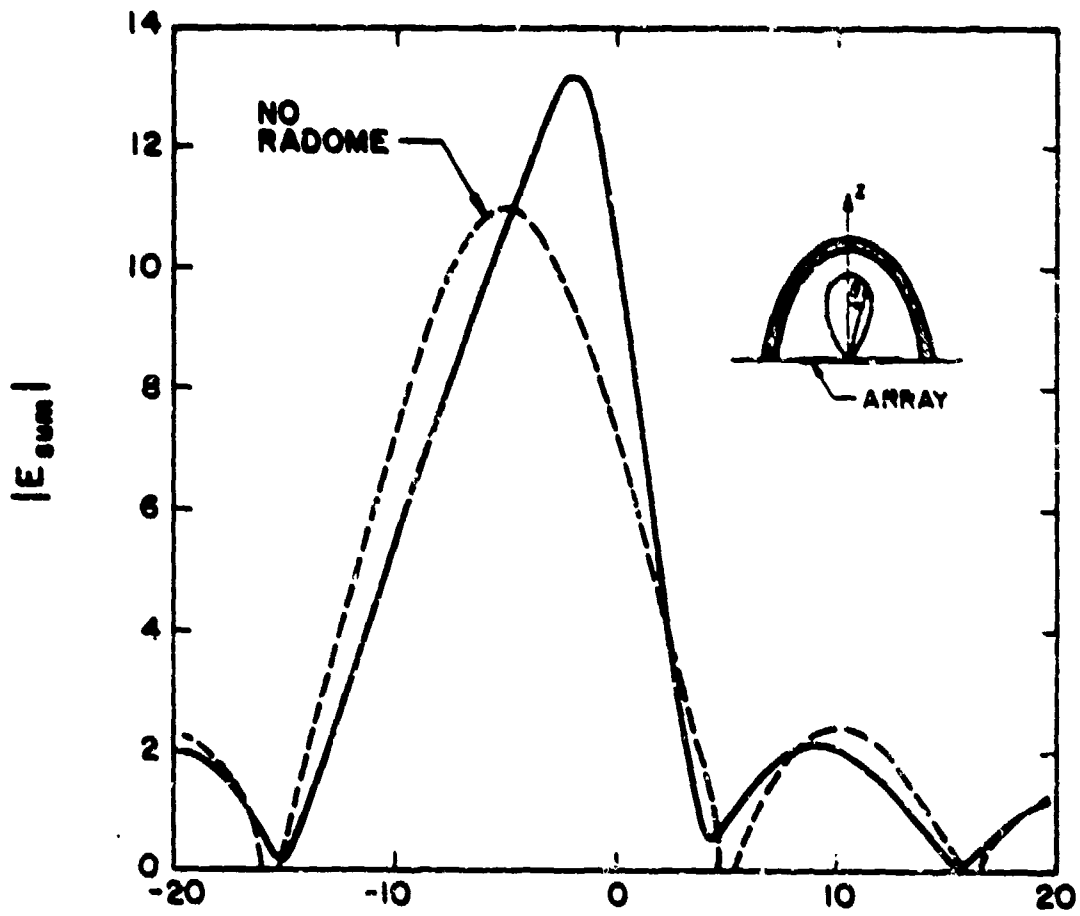


Figure 46. H-plane sum pattern through radome B. Beam at 0° .



POLAR ANGLE, θ (DEGREES)

Figure 47. Same as Figure 46, except for scan angle = -4.95° .

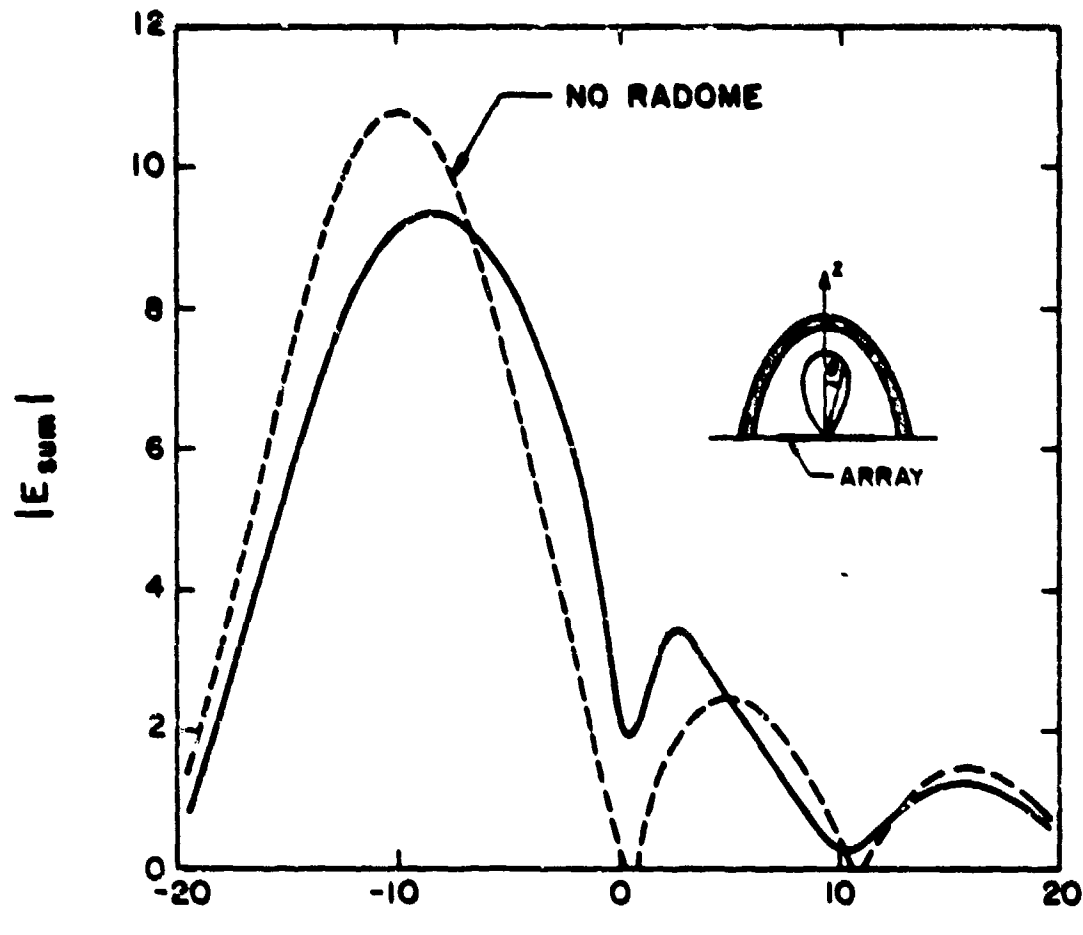


Figure 48. Same as Figure 46, except for scan angle = -9.89° .

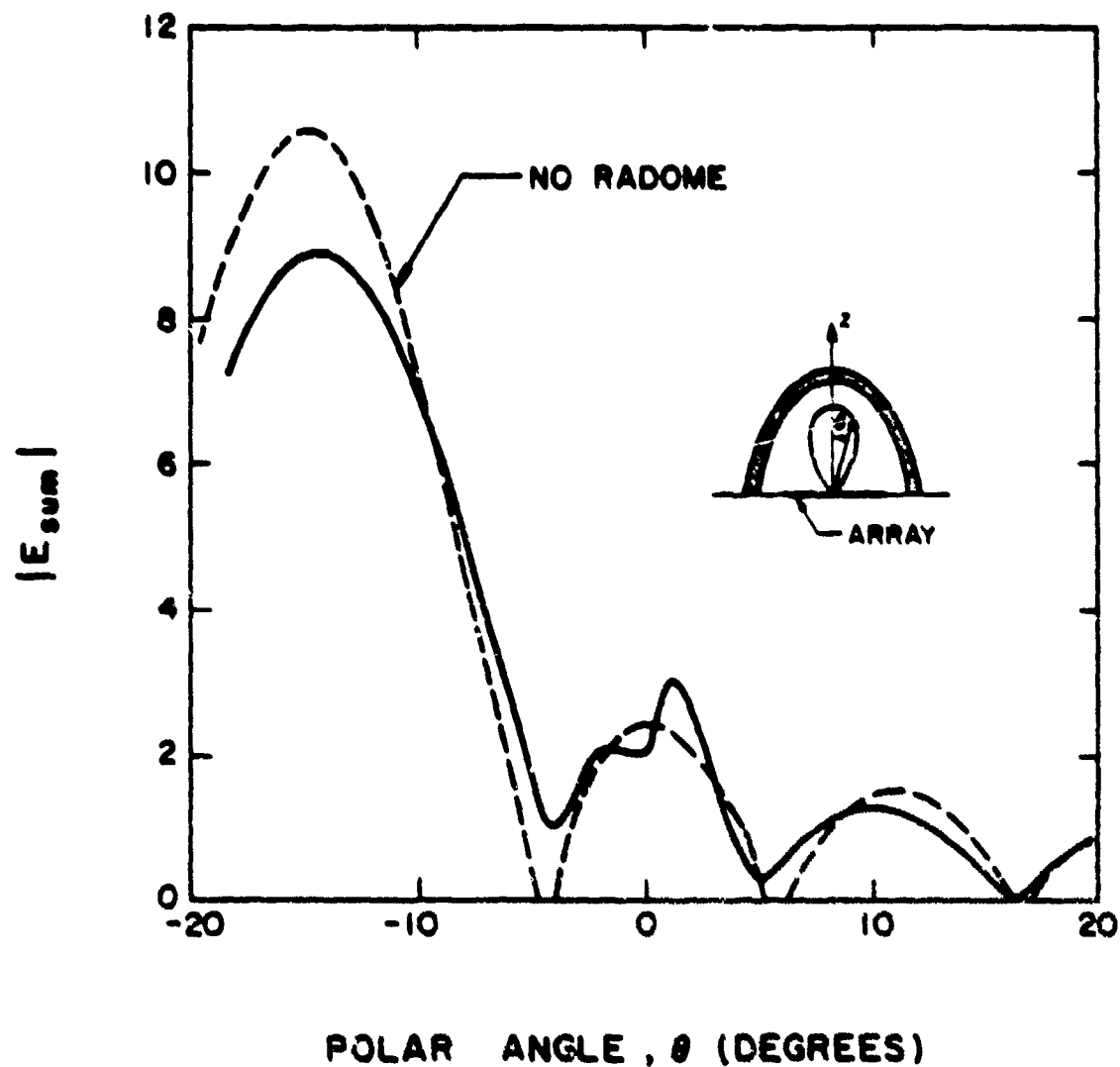


Figure 49. Same as Figure 46, except for scan angle = -14.83° .

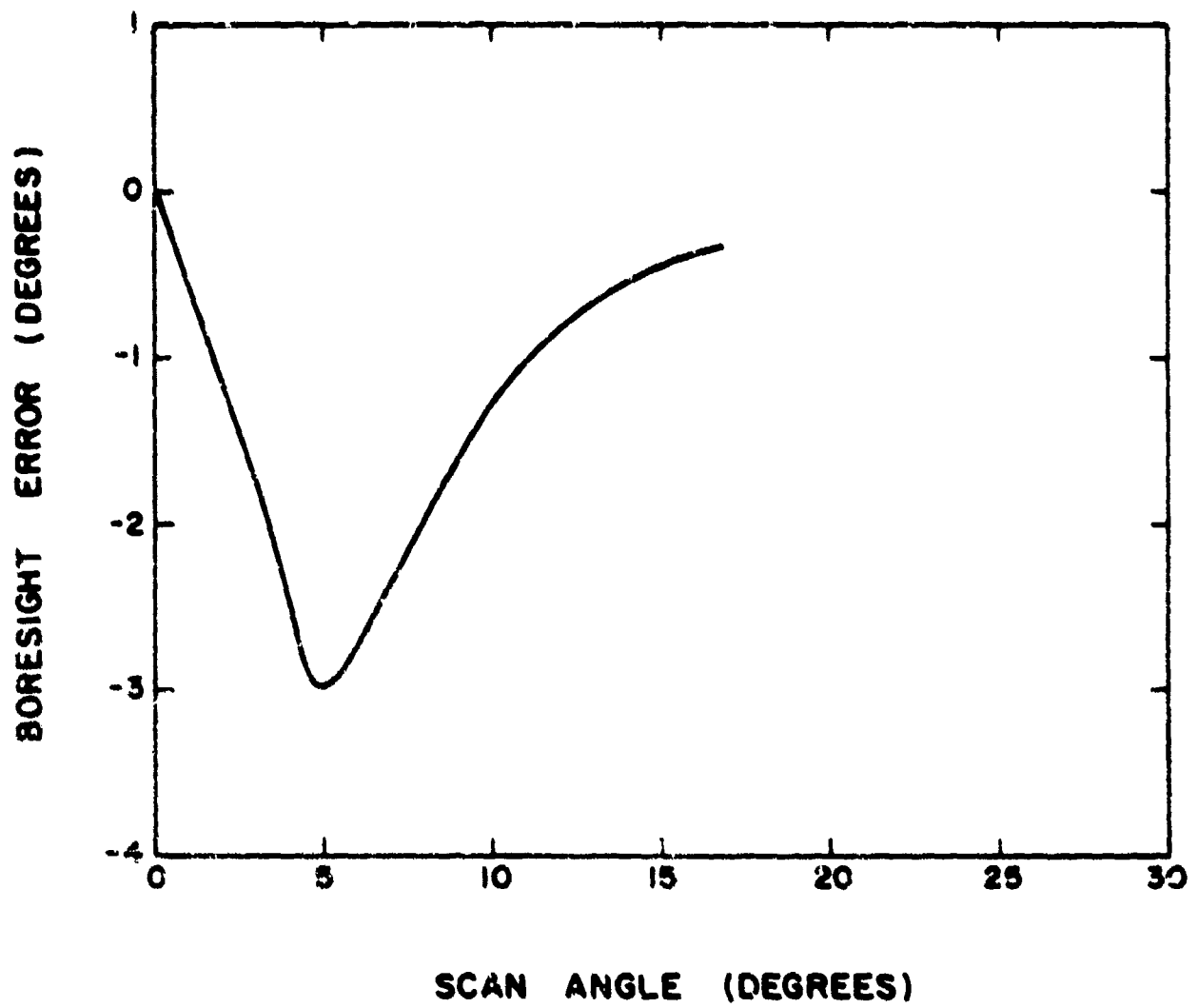


Figure 50. Boresight error for radome B.

(c) Radomes C and D: These are tangent ogive radomes used in missiles. The geometrical configuration is given in Figure 51. Radome C has $c_T = 5.7$ and radome D $c_T = 9.3$. It may be observed from Figure 51 that the radome has a discontinuity in the z-direction. In practice, this discontinuous tip region is replaced by a smooth curved surface. However, in our calculations, this modification was not introduced. The field along the z-axis was calculated by interpolation.

The H-plane sum patterns for radome C are presented in Figures 52-57, and the corresponding boresight error curve is shown in Figure 53. The patterns for radome D are in Figures 59-64. The boresight error curve is shown in Figure 65. It may be observed from these figures that the patterns for small scan angles are not generally good. Also, the boresight error at small scan angles is quite high. This behavior is not usually observed in practical radomes for two reasons:

(i) In practice, the antenna is usually a reflector antenna or a planar array of considerably large number of elements, whereas in our model, we have only eleven point sources $\lambda_0/2$ apart.

If one includes a sufficient number of point sources so as to faithfully represent a given practical antenna, there will be considerable changes in the sum patterns and the boresight error curves.

(ii) The second reason has something to do with the tip region.

Figure 66 shows a tangent ogive and a paraboloidal radome of the same size. It may be observed that the tip region in the tangent ogive is very steep whereas in the paraboloid the surface changes more smoothly.

In general, the patterns improve at larger scan angles, as does the boresight error.

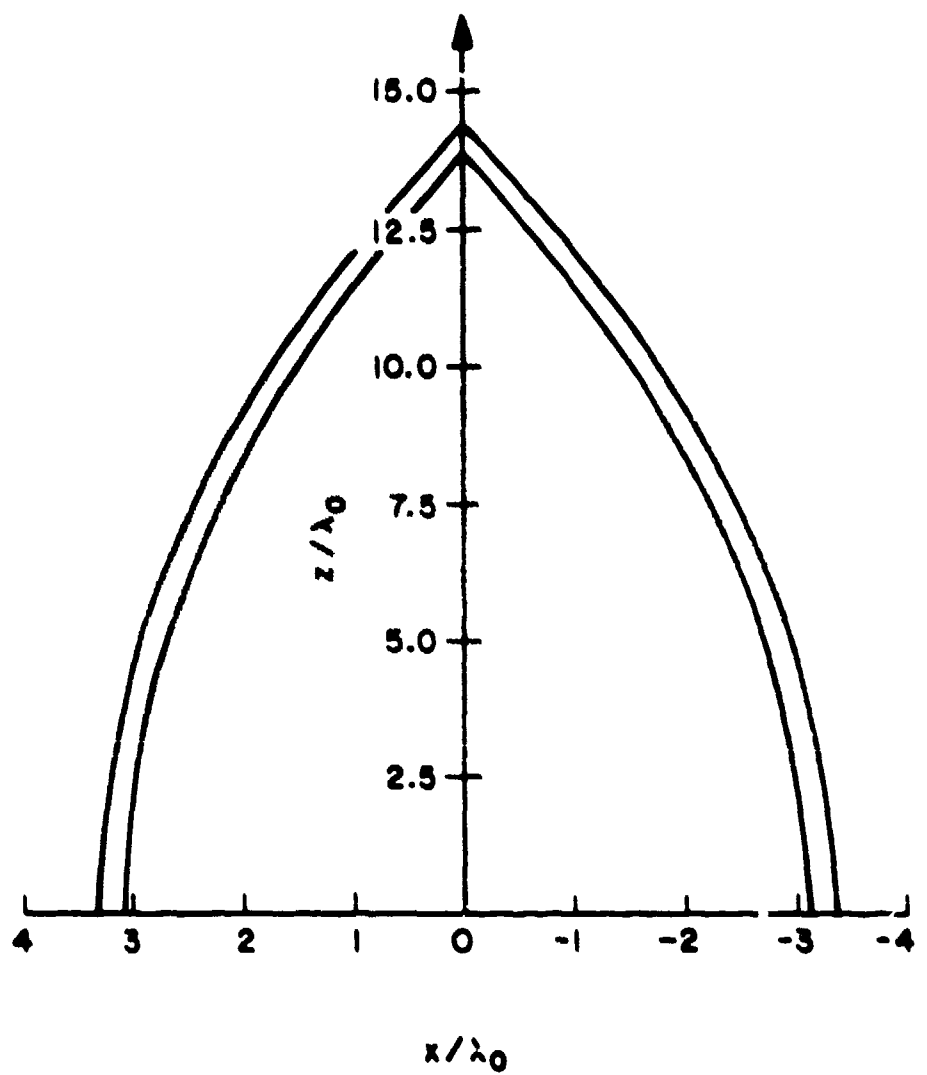


Figure 51. Geometry of radomes C and D.

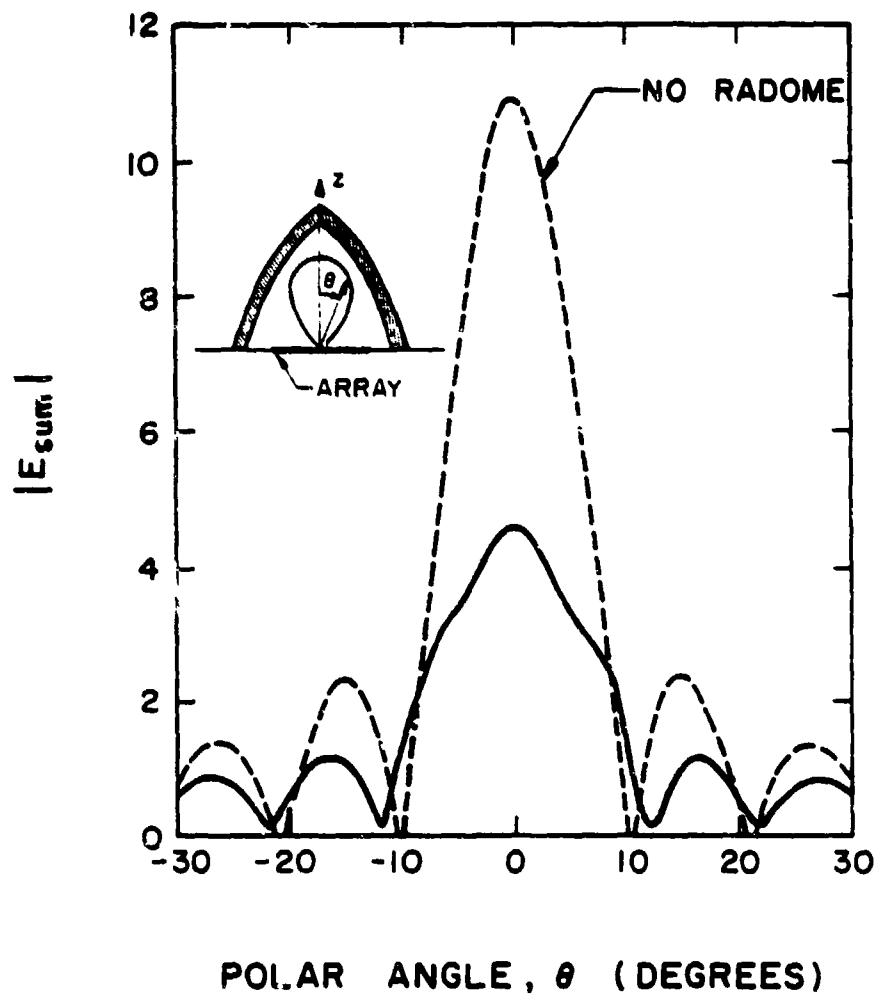


Figure 52. H-plane pattern through radome C. Beam at 0° .

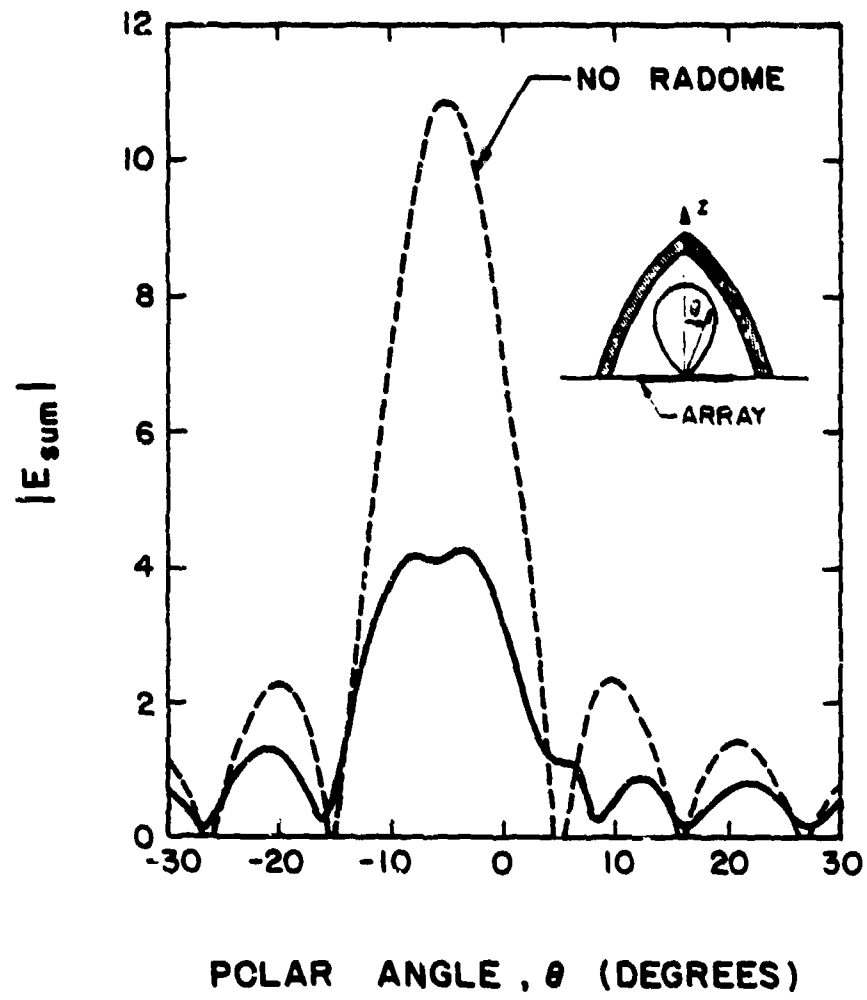


Figure 53. Same as Figure 52, except for scan angle = -4.95° .

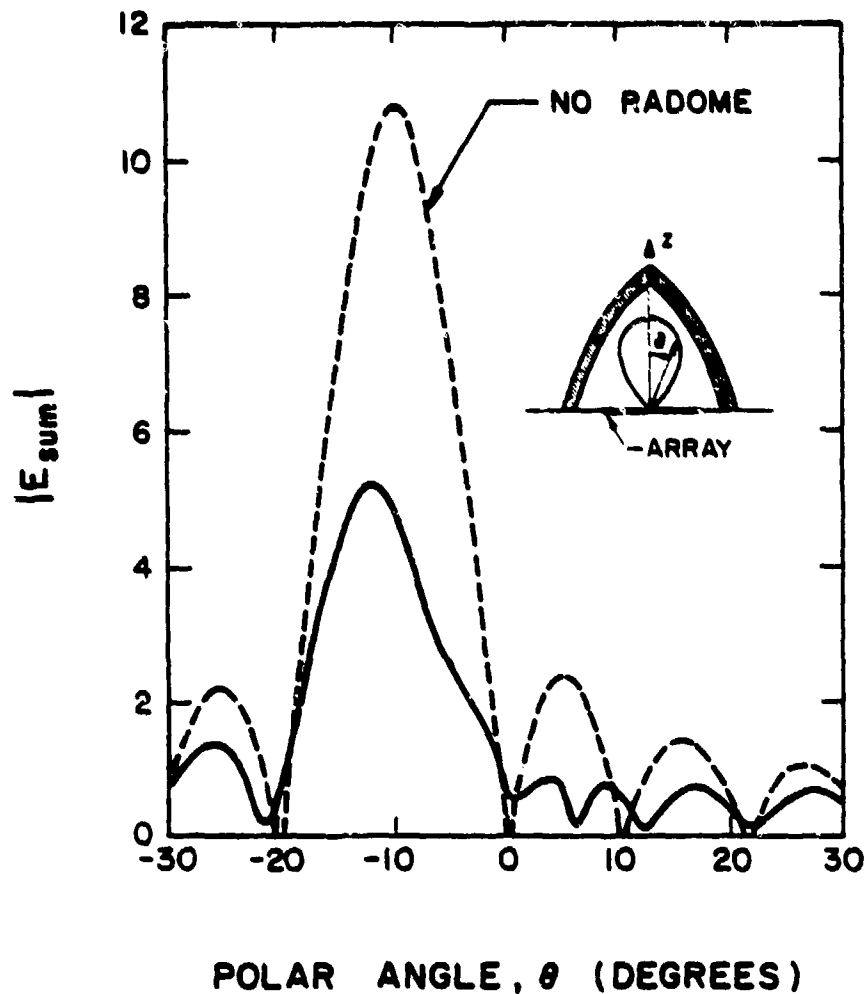


Figure 54. Same as Figure 52, except for scan angle = -9.89° .

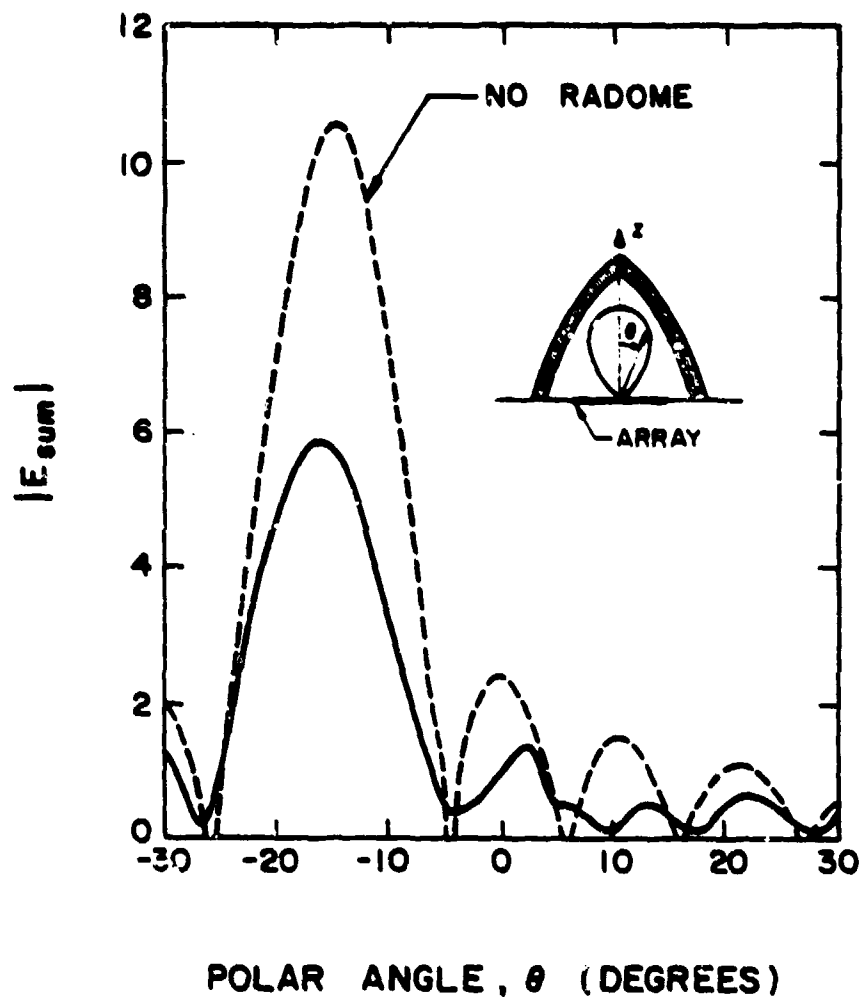


Figure 55. Same as Figure 52, except for scan angle = -14.83° .

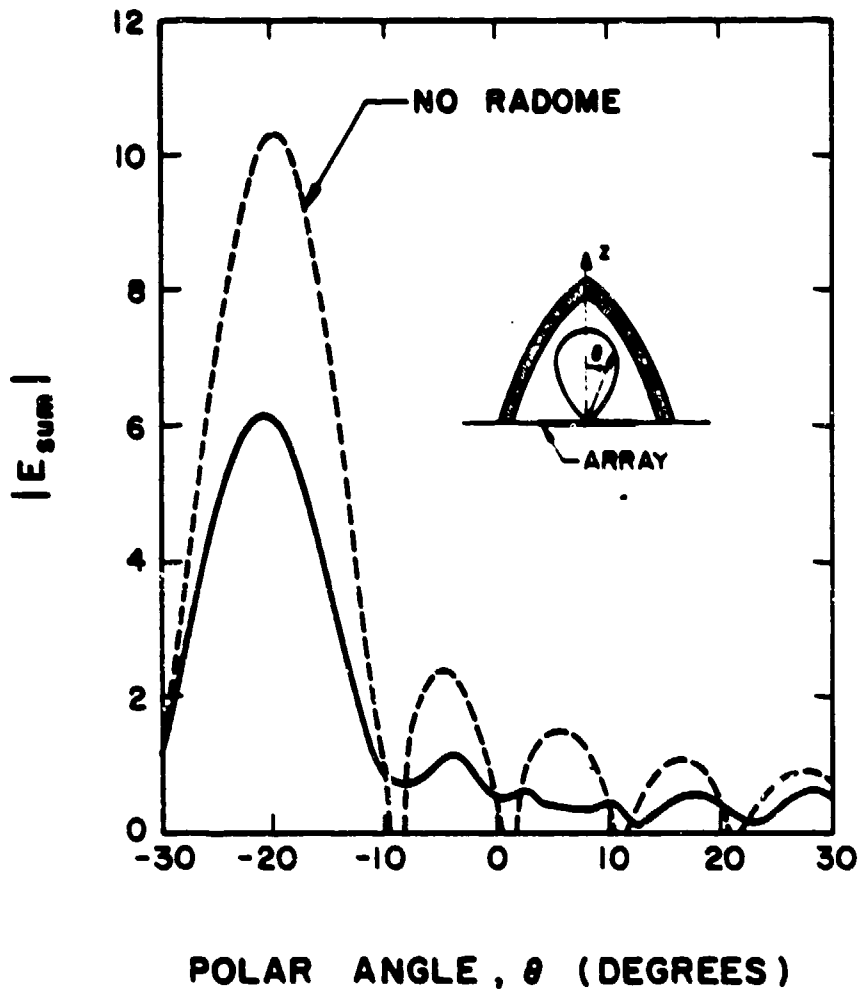


Figure 56. Same as Figure 52, except for scan angle = -19.77° .

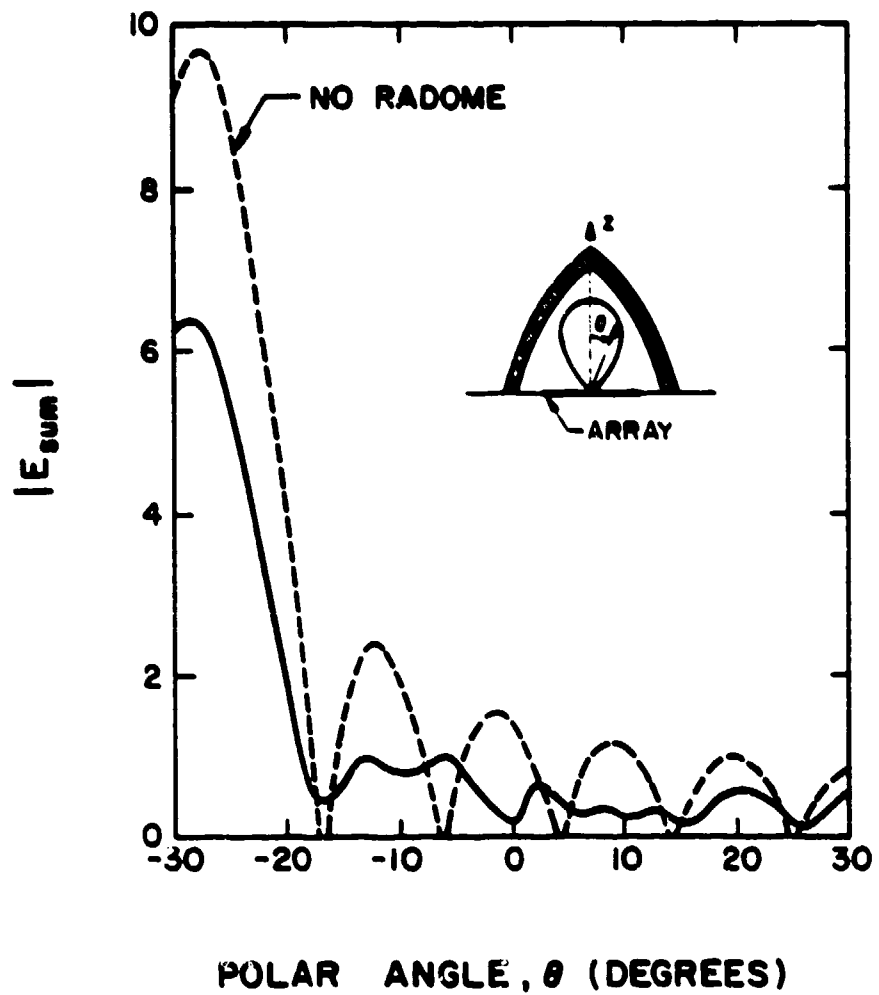


Figure 57. Same as Figure 52, except for scan angle = -27.64° .

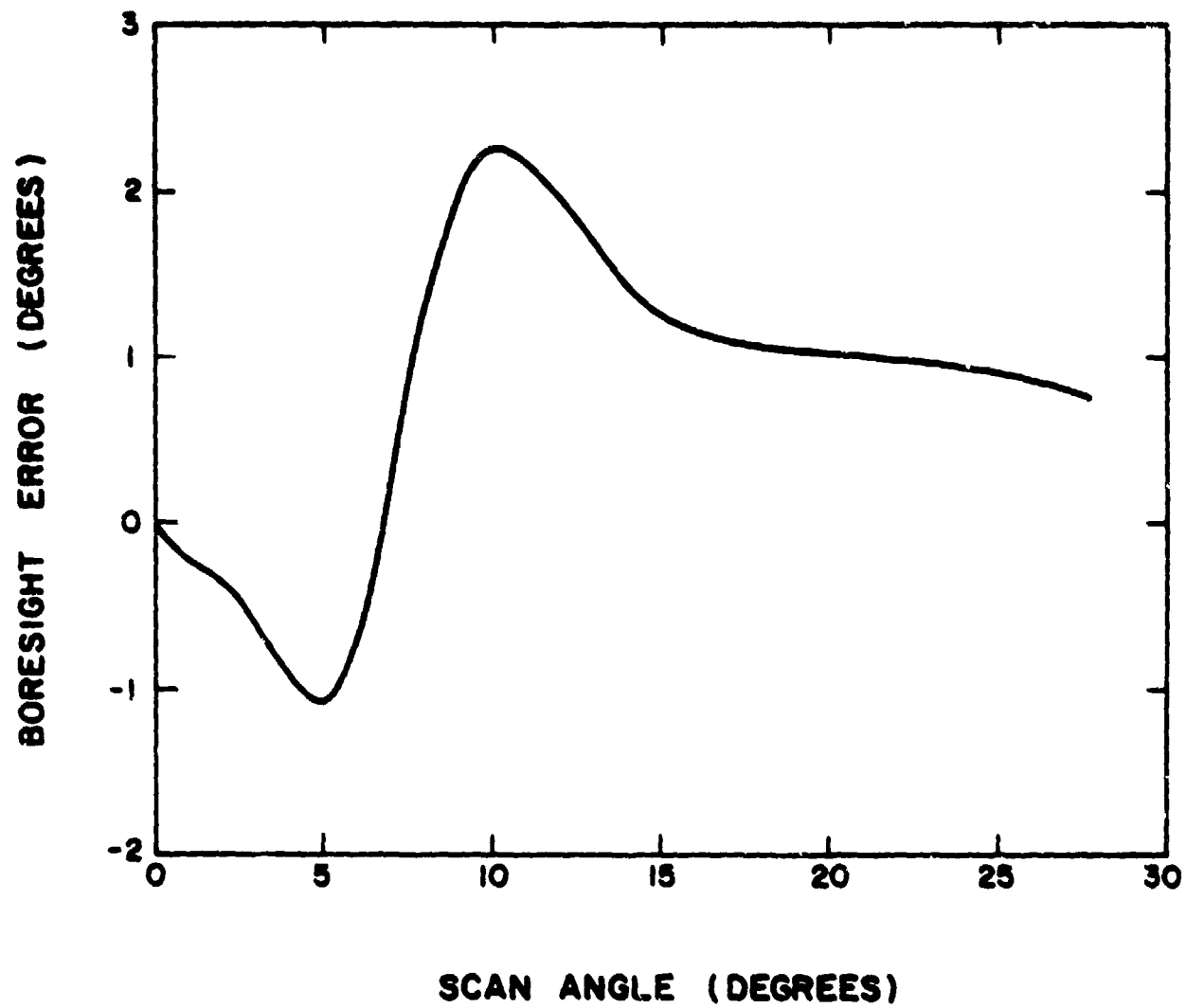


Figure 58. Boresight error for radome C.

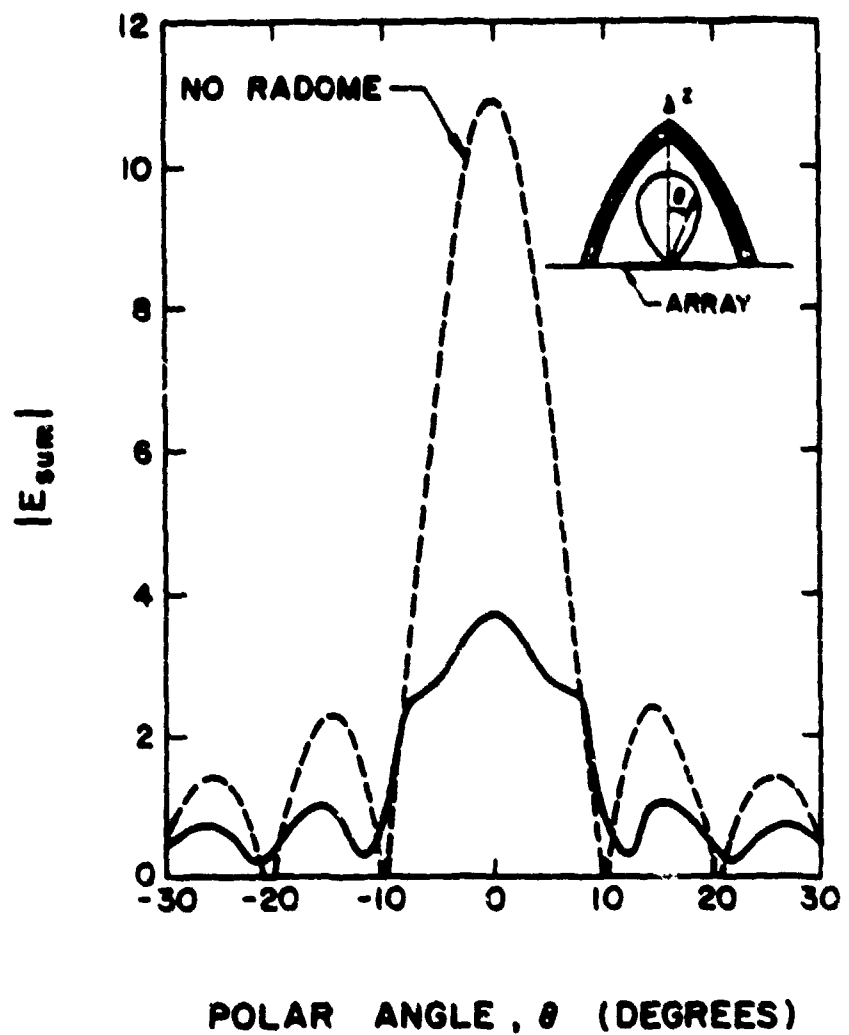


Figure 59. H-plane pattern through radome D. Beam at 0°.

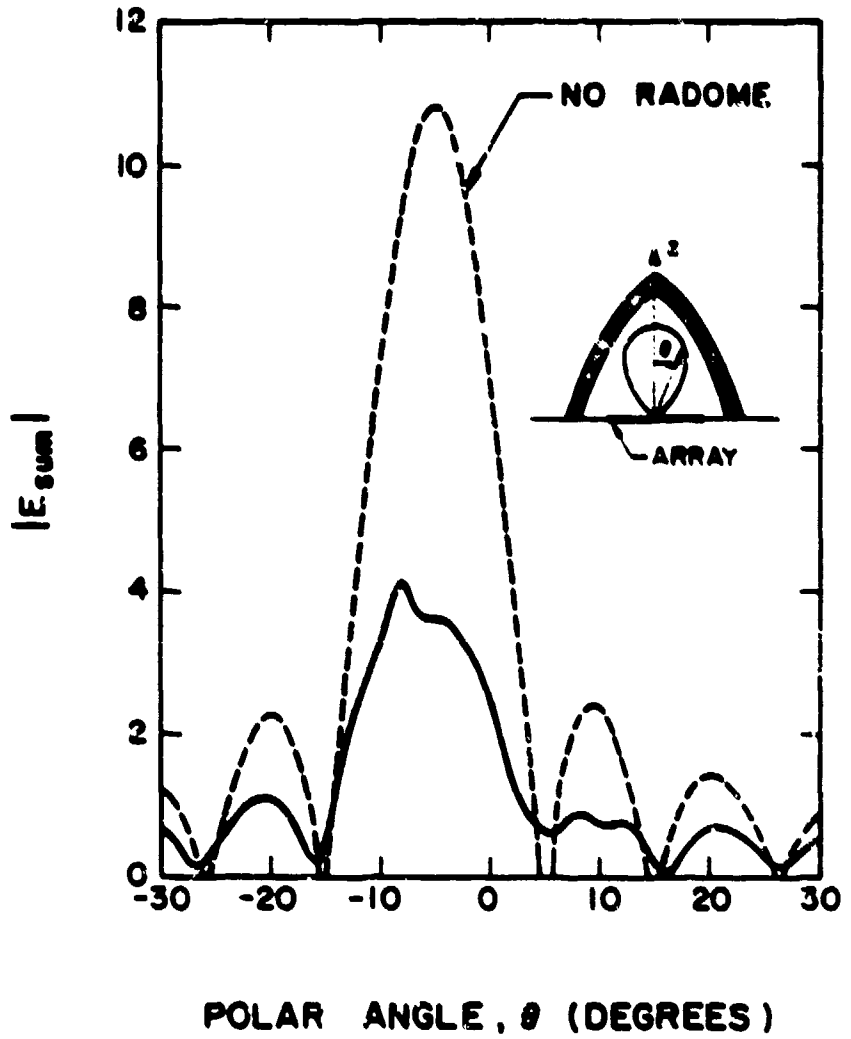


Figure 60. Same as Figure 59, except for scan angle = -4.95° .

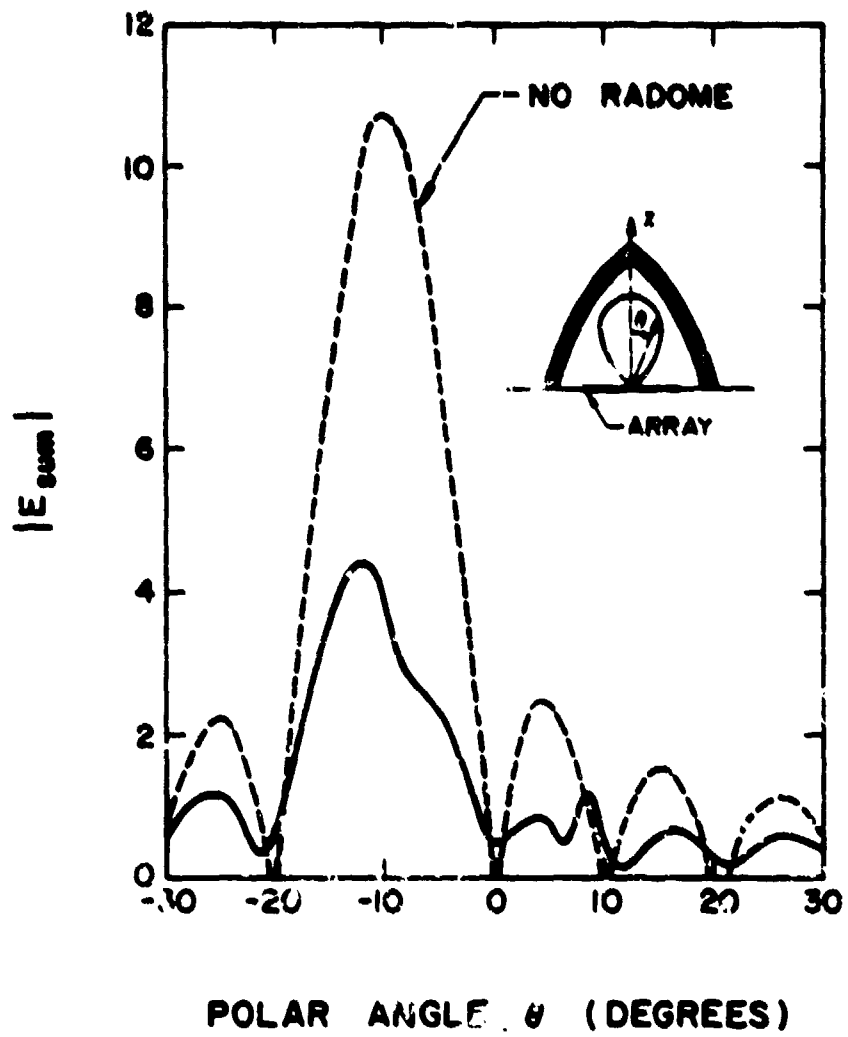
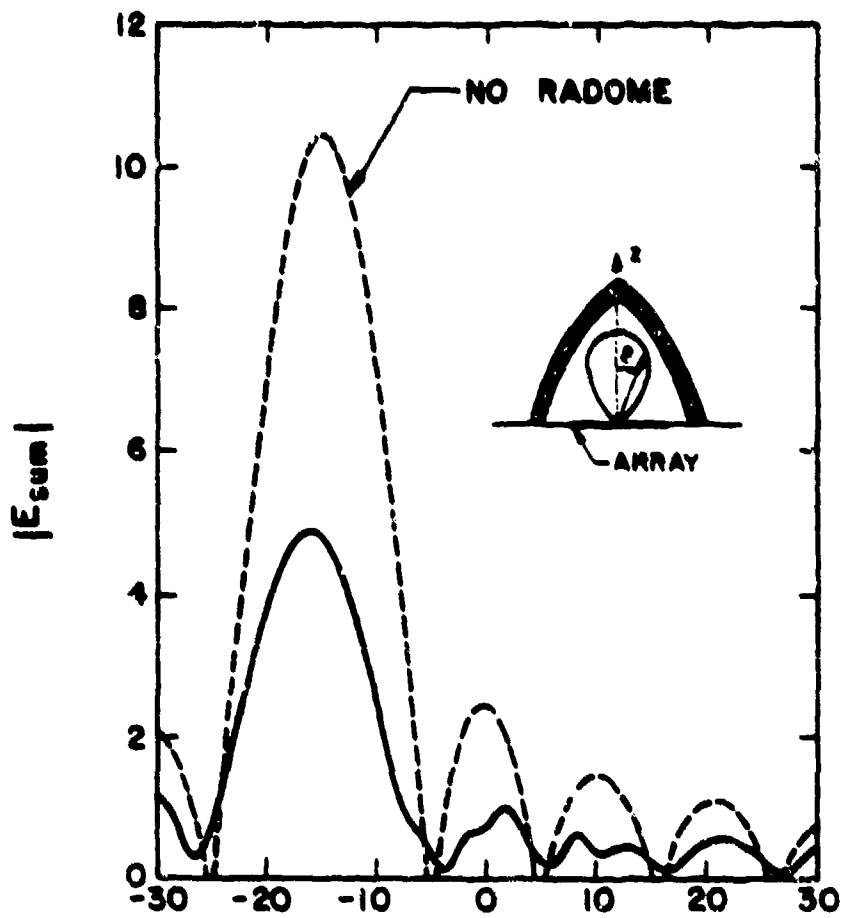


Figure 61. Same as Figure 59, except for scan angle = -9.89° .



POLAR ANGLE, θ (DEGREES)

Figure 62. Same as Figure 39, except for scan angle = -14.83° .

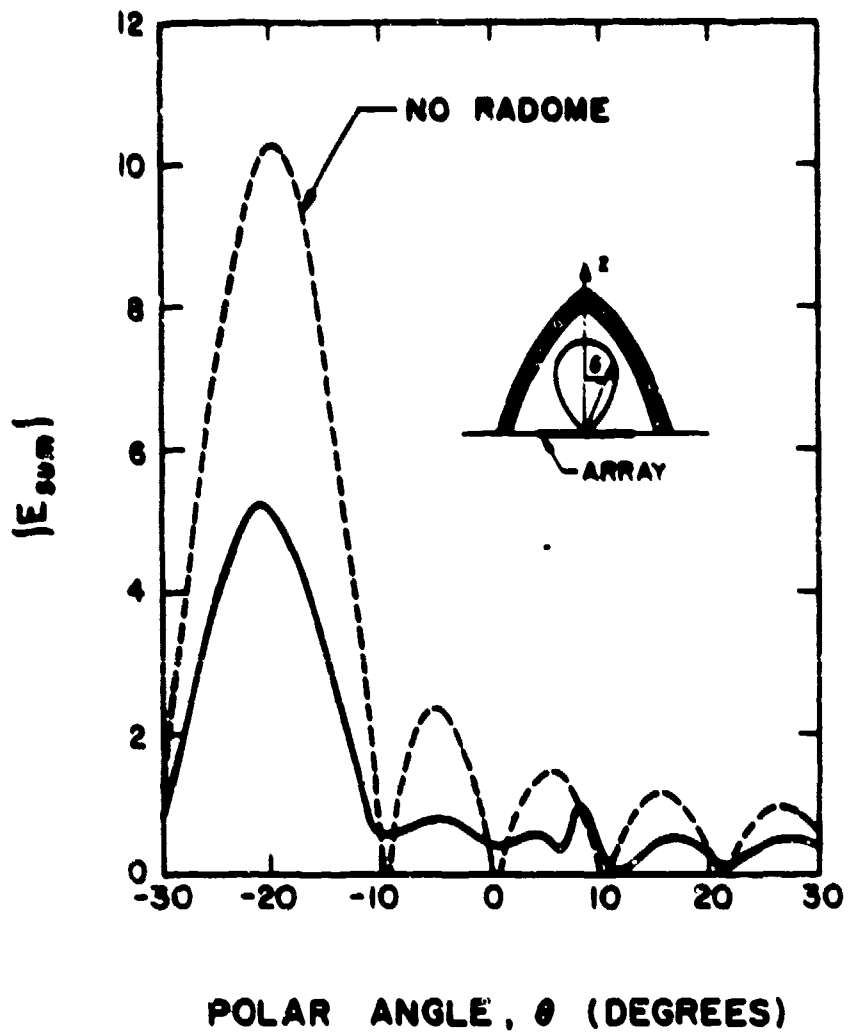


Figure 63. Same as Figure 59, except for scan angle = -19.77° .

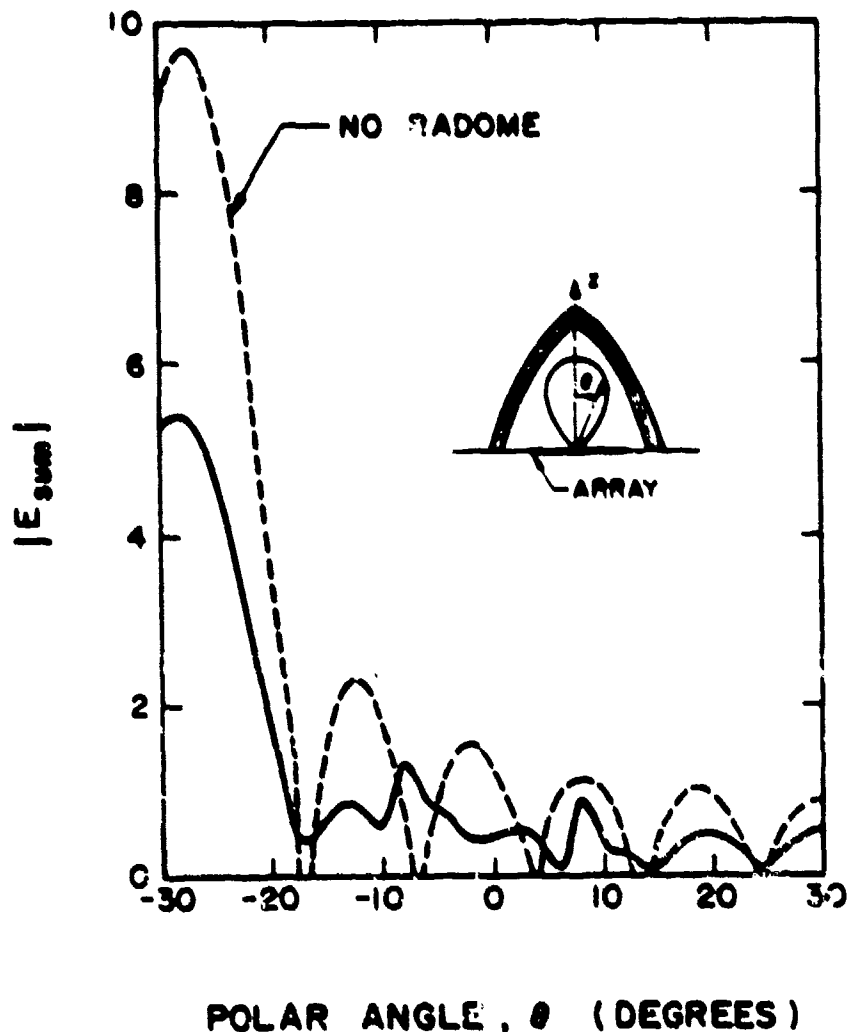


Figure 64. Same as Figure 59, except for scan angle = -27.65° .

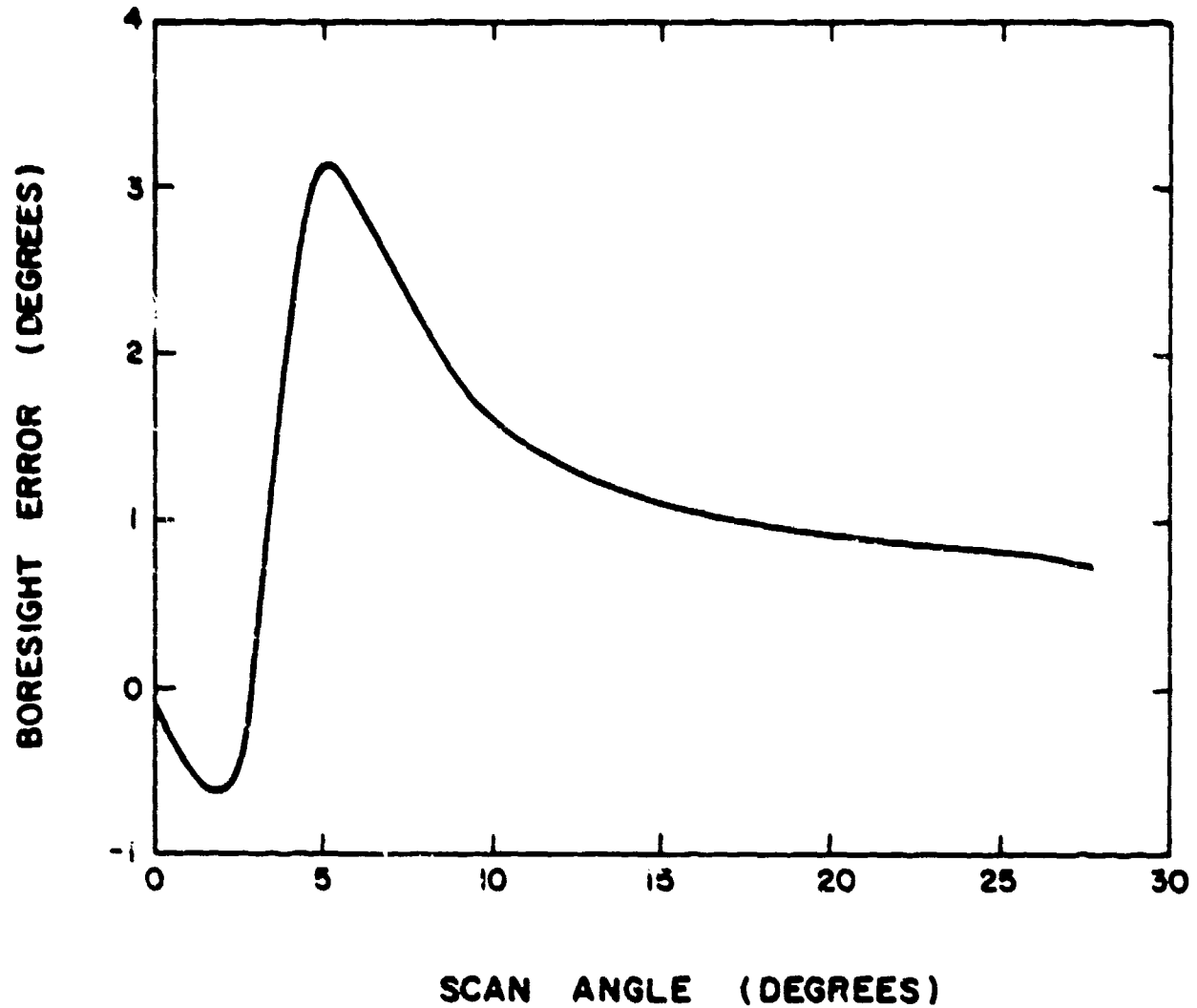


Figure 65. Bore sight error for radome D.

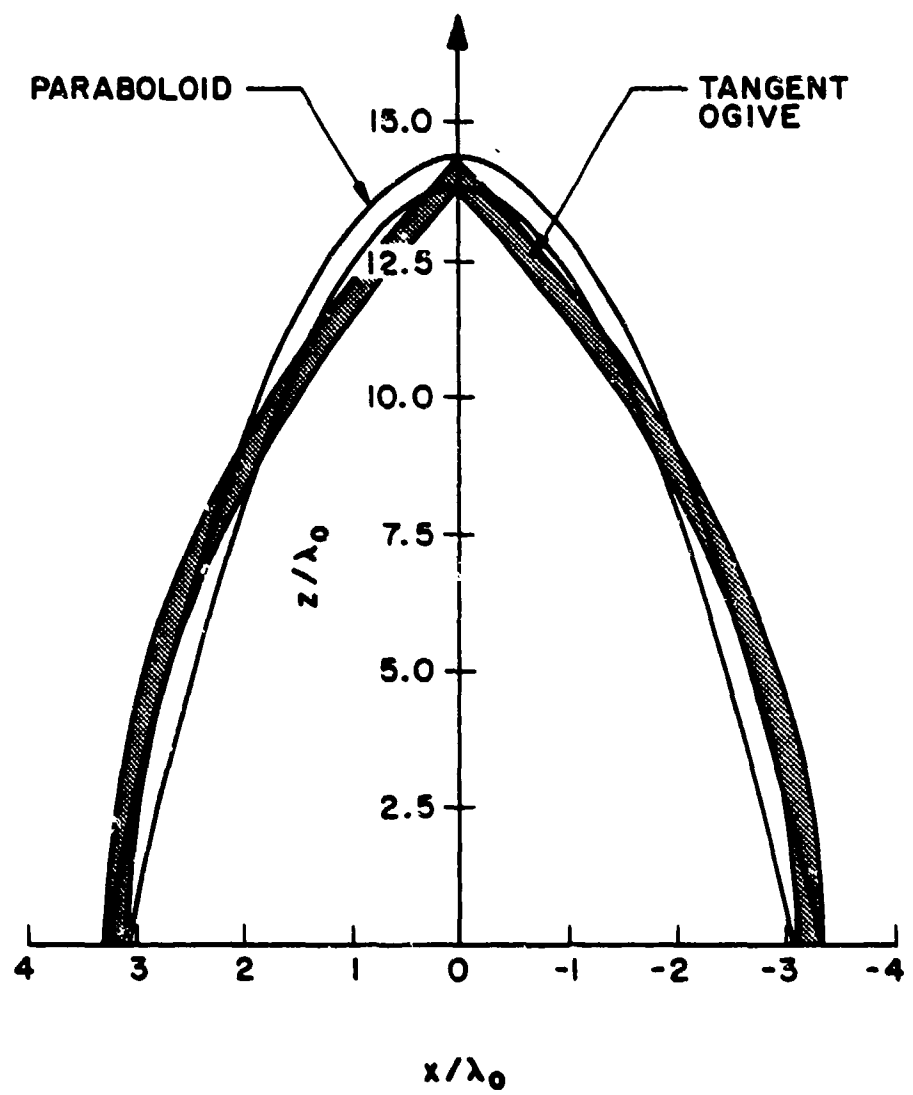


Figure 66. Comparison of tangent ogive and an equivalent paraboloid.

APPENDIX A

DERIVATION OF EQUATION (5.6)

Referring to Figure 21, the curvature matrix [4], [10] of the incident spherical wave may be expressed as

$$Q_1^i = \begin{bmatrix} a^{-1} & 0 \\ 0 & a^{-1} \end{bmatrix} . \quad (A.1)$$

The curvature matrix of the inner surface of the radome (Σ_1) is

$$Q^{\Sigma_1} = \begin{bmatrix} R_1^{-1} & 0 \\ 0 & R_1^{-1} \end{bmatrix} . \quad (A.2)$$

From the knowledge of these two curvature matrices, the curvature matrix of the refracted ray 1-2 may be expressed as [4]

$$Q_1^t = (\theta_1^t)^{-1} [\theta_1^i Q_1^i \theta_1^i / n + (\cos \alpha_1^t - \cos \alpha_1^i / n) Q^{\Sigma_1} (\theta_1^t)^{-1}] \quad (A.3)$$

where θ_1^i and θ_1^t are coordinate transformation matrices given by

$$\theta_1^i = \begin{bmatrix} \cos \alpha_1^i & 0 \\ 0 & 1 \end{bmatrix} \quad (A.4)$$

$$\theta_1^t = \begin{bmatrix} \cos \alpha_1^t & 0 \\ 0 & 1 \end{bmatrix} . \quad (A.5)$$

Simplifying (A.3), we obtain

$$Q_1^t = \begin{bmatrix} \kappa_{11} & 0 \\ 0 & \kappa_{12} \end{bmatrix} \quad (A.6)$$

where κ_{11} and κ_{12} are defined in (5.7).

The curvature matrix of the wavefront incident at point 2 is given by

$$Q_2^i = [(Q_1^t)^{-1} + b \bar{I}]^{-1} \quad (A.7)$$

where \bar{I} is the identity matrix. The curvature matrix of the transmitted wavefront at 2 can be calculated similarly to that at 1. The final result is

$$Q_2^t = \begin{bmatrix} \kappa_{21} & 0 \\ 0 & \kappa_{22} \end{bmatrix} \quad (A.8)$$

where κ_{21} and κ_{22} are defined in (5.7).

REFERENCES

- [1] D. T. Paris, "Computer aided radome analysis," IEEE Trans. Antennas Propagat., vol. AP-18, pp. 7-15, 1970.
- [2] D. C. F. Wu and R. C. Rudduck, "Plane wave spectrum - surface integration technique for radome analysis," IEEE Trans. Antennas Propagat., vol. AP-22, pp. 497-500, 1974.
- [3] S. W. Lee, "Geometrical theory of diffraction in electromagnetics, Vol. 1: Geometrical optics," Tech. Rept. 78-2, Electromagnetics Lab., Univ. of Ill., Urbana, IL, 1978.
- [4] G. A. Deschamps, "Ray techniques in electromagnetics," Proc. IEEE, Vol. 60, pp. 1022-1035, 1972.
- [5] S. W. Lee, V. Jamnejad, M. S. Sheshadri, and R. Mittra, "Analysis of antenna radomes by ray techniques," Tech. Rept., Electromagnetics Laboratory, Univ. of Ill., Urbana, IL, May 1980.
- [6] A. Gullstrand, "Das allgemeine optische Abbildungs system Svenska Vetensk," Fandl., vol. 55, pp. 1-139, 1915.
- [7] A. W. Snyder and J. D. Love, "Reflection at curved dielectric interface - electromagnetic tunneling," IEEE Trans. Microwave Theory Tech., vol. MTT-23, pp. 134-141, 1975.
- [8] J. D. Love and A. W. Snyder, "Generalized Fresnel laws for a curved absorbing interface," J. Opt. Soc. Amer., vol. 65, no. 9, pp. 1072-1074, September 1975.
- [9] J. D. Love and A. W. Snyder, "Fresnel's and Snell's laws for the multimode optical waveguide of circular cross sections," J. Opt. Soc. Amer., vol. 65, no. 11, pp. 1241-1247, November 1975.
- [10] S. W. Lee, "Differential geometry for GTD applications," Electromagnetics Laboratory Report 77-21, University of Illinois, Urbana, IL, 1977.
- [11] F. W. Sears, M. W. Zemansky, and H. D. Young, University Physics, 5th ed. Massachusetts: Addison-Wesley, 1976.
- [12] L. M. Brekhovskikh, Waves in Layered Media. New York: Academic Press Inc., 1960
- [13] J. H. Bruning and Y. T. Lo, "Multiple scattering of EM waves by spheres: Part I - Multipole expansion and ray-optical solutions; Part II - Numerical and experimental results," IEEE Trans. Antennas Propagat., vol. AP-19, no. 3, pp. 378-400, May 1971.

- [14] S. W. Lee, P. Cramer, Jr., K. Woo and Y. Rahmat-Samii, "Diffraction by an arbitrary subreflector: GTD solution," IEEE Trans. Antennas Propagat., vol. AP-27, no. 3, pp. 305-316, May 1979.
- [15] S. Silver, Microwave Antenna Theory and Design. New York: Dover, 1965.
- [16] P. D. Kinsiger, L. B. Felsen, and A. Neissel, "Rigorous asymptotic analysis of transmission through a curved dielectric slab," paper presented in URSI meeting, Los Angeles, June 1981.

DISTRIBUTION LIST

Commander
Naval Air Systems Command
ATTN: AIR-310B (2 copies quarterly, 5 copies final)
AIR-360E (C. A. Thomas)
AIR-950D6 (14 copies final only)
Washington, DC 20361

Commander
Naval Weapons Center
ATTN: Dr. G. H. Winkler, Code 381
China Lake, CA 93555

Commander
Naval Air Development Center
ATTN: Mr. J. Z. Lyons, Code 204
Warminster, PA 18974

Commander
Naval Ocean Systems Center
ATTN: J. Boyne, Code 8211
San Diego, CA 92152

Ohio State University
Electro Science Laboratory
ATTN: Dr. C. H. Walter
1320 Kinnear Road
Columbus, OH 43212

University of Colorado
Department of Electrical Engineering
ATTN: Prof. L. Lewin
Boulder, CO 80302

General Dynamics Corporation
Electronics Division
ATTN: Dr. G. Tricoles
P. O. Box 81127
San Diego, CA 92138

Commander
Air Force Avionics Laboratory/DHM
ATTN: Mr. Harold Weber
Mr. Alan Blume
Wright-Patterson Air Force Base, OH 45433

Office of Naval Research
ATTN: Dr. H. Mullaney/Code 427
800 North Quincy Street
Arlington, VA 22217

R. C. Hansen, Inc.
Box 215
Tarzana, CA 91356

Harry Diamond Laboratories
ATTN: Dr. Howard S. Jones, Jr./AMDDO-RAE
2800 Powder Mill Road
Adelphi, MD 20783

Missile Intelligence Agency
US Army Missile Command
ATTN: Mr. R. Thompson (MSMI/YPE)
Redstone Arsenal, AL 35809

Hughes Aircraft Company
Radar Systems Group
ATTN: Dr. W. H. Kummer/MSR2-A102
P. O. Box 92426
Los Angeles, CA 90009

Mr. Gordon Lovitt
Office of Naval Research Branch Office
536 S. Clark
Chicago, IL 60605

Prof. S. W. Lee
Electromagnetics Laboratory
Department of Electrical Engineering
University of Illinois
1406 W. Green St.
Urbana, Illinois 61801

Prof. R. Mittra
Electromagnetics Laboratory
Department of Electrical Engineering
University of Illinois
1406 W. Green St.
Urbana, Illinois 61801

Mr. H. Lawler
Department of Electrical Engineering
University of Illinois
1406 W. Green St.
Urbana, Illinois 61801